





Universitat Autònoma de Barcelona

**ADVERTIMENT.** L'accés als continguts d'aquesta tesi queda condicionat a l'acceptació de les condicions d'ús establertes per la següent llicència Creative Commons:  [http://cat.creativecommons.org/?page\\_id=184](http://cat.creativecommons.org/?page_id=184)

**ADVERTENCIA.** El acceso a los contenidos de esta tesis queda condicionado a la aceptación de las condiciones de uso establecidas por la siguiente licencia Creative Commons:  <http://es.creativecommons.org/blog/licencias/>

**WARNING.** The access to the contents of this doctoral thesis it is limited to the acceptance of the use conditions set by the following Creative Commons license:  <https://creativecommons.org/licenses/?lang=en>



Universitat Autònoma  
de Barcelona

# **Sustainable Materials by Electrodeposition and Sputter Deposition Methods**

---

Doctoral Thesis presented by Doğa Bilican

Supervised by  
Dr. Jordi Sort Viñas  
Dra. Eva Pellicer Vilà  
Dra. Jordina Fornell Beringues

Materials Science Doctorate Programme  
Department of Physics  
Faculty of Sciences  
June 2018



El Prof. Jordi Sort Viñas, professor d'investigació ICREA del Departament de Física de la Universitat Autònoma de Barcelona,

La Dra. Eva Pellicer Vilà, investigadora Ramón y Cajal del Departament de Física de la Universitat Autònoma de Barcelona,

i la Dra. Jordina Fornell Beringues, investigadora post-doctoral del Departament de Física de la Universitat Autònoma de Barcelona,

Certifiquen:

Que Doğa Bilican ha realitzat sota la seva direcció el treball d'investigació que s'exposa a la memòria titulada "Sustainable Materials by Electrodeposition and Sputter Deposition Methods per optar al grau de **Doctor per la Universitat Autònoma de Barcelona**.

Que el disseny dels experiments, síntesi de mostres, llur caracterització, l'anàlisi dels resultats, la redacció dels articles i d'aquesta memòria són fruit del treball d'investigació realitzat per Doğa Bilican.

I perquè així consti, signen el present certificat,

Prof. Jordi Sort Viñas

Dra. Eva Pellicer Vilà

Dra. Jordina Fornell Beringues



## Acknowledgements

First of all, I would like to thank my supervisors, Prof. Jordi Sort, Dr. Eva Pellicer and Dr. Jordina Fornell for their guidance, patience and support that they showed from the very beginning of my thesis. The time I spent under your supervision taught me a lot about many aspects of science and made me grow as a researcher.

I would like thank Prof. Maria Dolors Baró and Prof. Santiago Suriñach for the kind advices they gave me whenever I needed their help. Also I am grateful to Jordi Malapeira for always being informative and helpful to me in managing administrative issues.

I am thankful to Dr. Pau Solsona for his help in heat treatment processes and Dr. Enric Menéndez for his help in data analysis. Also, it is a pleasure for me to acknowledge the support from the UAB Microscopy Service and the UAB X-ray Diffraction Service.

I would like thank to all the other current and former members of Gnm<sup>3</sup> group: Shauna, Alberto, Isarain, Evangelia, Jin, Irati, Miguel, Junpeng, Yuping and Huiyan. Thank you for giving me a very warm welcome in the beginning and sharing the lab-life with me for the last three years.

I would like to thank Prof. Zoe Barber for her support and kindness during the period that I spent in the Device Materials Group in University of Cambridge. I may certainly not forget to thank Samer Kurdi and Yi Zhu whom I had the chance to collaborate with during my stay there.

Being a part of the SELECTA-ETN (Smart Electrodeposited Alloys for Environmentally Sustainable Applications-European Training Network, no: 642642) during my Ph.D. was a unique and priceless experience that gave me the chance to meet many inspiring scientists and broadened my horizons in research. I would like to mention that it was a pleasure to meet and spend time with all the principal investigators and Ph.D. candidates that took part in this project.

v

My friends in Barcelona; Shauna, Merve and her lovely cat Rıfki, Evrim, Sinem and Timi, thank you for making my time in this city unforgettable.

I would like to especially thank my family and all my friends for showing an infinite sympathy, support and patience to me in every move I make. Thank you for accepting me as who I am and for your endless encouragement and motivational support.

Doğa Bilican



## Resum

Aquesta Tesi engloba la fabricació i caracterització de materials sostenibles com poden ser partícules de bismut (Bi), capes de ferrita de bismut ( $\text{BiFeO}_3$ ) i aliatges de base Cu amb memòria de forma. S'ha emprat l'electrodeposició per obtenir partícules de Bi micromètriques i submicromètriques a partir d'un electròlit aquós així com també per sintetitzar capes de  $\text{BiFeO}_3$  a partir d'un bany de dimetilformamida seguit d'un tractament tèrmic en aire. Els aliatges amb memòria de forma de coure-alumini-níquel (Cu–Al–Ni) s'han fabricat mitjançant polvorització catòdica. Per obtenir les capes primes de Cu–Al–Ni s'han utilitzat dues metodologies diferents: d'una banda, s'han dipositat capes de Cu–Ni i Al alternativament per tal d'obtenir una estructura tipus sandvitx; seguidament les capes s'han tractat tèrmicament i s'han trempat en aigua gelada. D'altra banda, s'han crescut capes de Cu–Al–Ni en substrats de MgO aplicant temperatura. Les capes s'han caracteritzat morfològicament mitjançant microscòpia electrònica de rastreig (SEM). Per a la caracterització estructural s'ha utilitzat difracció de raigs X (XRD) i microscòpia electrònica de transmissió (TEM). Les capes de ferrita de bismut s'han mesurat per magnetometria de mostra vibrant (VSM). Per tal de conèixer les temperatures de transició de fase de les capes de Cu–Al–Ni s'han dut a terme mesures de resistivitat en funció de la temperatura. S'ha estudiat la morfologia de les partícules de bismut en funció de la composició del bany, de l'activitat del substrat i del potencial aplicat. A mesura que s'augmenta el valor absolut del potencial aplicat es va observar un canvi en la morfologia de les partícules (d'hexàgons a dendrites) independentment del substrat utilitzat. Cal remarcar que les partícules de bismut recobreixen el substrat de forma més homogènia (sense aglomeracions) quan s'afegeix gluconat de sodi al bany. La caracterització estructural de les capes de  $\text{BiFeO}_3$  preparades per electrodeposició i posterior tractament tèrmic revelà que l'estructura romboèdrica de  $\text{BiFeO}_3$  (interessant pel seu caràcter multiferroic) es forma al voltant dels 600 °C. El lleuger senyal ferromagnètic observat a la capa tractada tèrmicament a 600 °C s'atribueix principalment al seu caràcter nanoestructurat, la qual cosa afavoreix l'aparició de fenòmens d'inclinació aleatòria dels espins a la superfície (efecte conegut com a *spin canting*) en la fase  $\text{BiFeO}_3$ . En les capes de Cu–Al–Ni preparades per polvorització catòdica i posterior tractament tèrmic, s'observà que un canvi gradual en la seva composició (és a dir, disminució del contingut d'Al i un augment del contingut de Ni) comporta un canvi en la fase formada a temperatura ambient (de martensita a austenita). Les capes obtingudes presenten una estructura policristal·lina orientada aleatòriament. D'altra banda, en les capes de Cu–Al–Ni fabricades a alta temperatura en substrats de MgO, es va detectar un creixement texturat en (200) a causa de la relació epitaxial entre la capa i el substrat. Les mesures de resistivitat versus temperatura van posar de manifest l'existència de transformació martensítica en la capa austenítica texturada mentre que no es va observar transformació en la capa austenítica orientada aleatòriament. Finalment, s'ha fet una contextualització general del potencial que presenten els materials desenvolupats en aquesta Tesi com a candidats sostenibles en sistemes micro i nano.





## **Abstract**

This thesis dissertation includes the synthesis and characterization of sustainable materials including bismuth (Bi), bismuth ferrite ( $\text{BiFeO}_3$ ) and copper-based shape memory alloys. Electrodeposition and sputter deposition were employed as the synthesis techniques. Electrodeposition was used in order to obtain micron and submicron sized Bi particles from an aqueous electrolyte and  $\text{BiFeO}_3$  films when electrodeposition from dimethylformamide bath was followed by heat treatment of the resulting coatings in open air. Sputter deposition was applied to produce copper-aluminium-nickel (Cu–Al–Ni) shape memory alloys. Two approaches were followed to obtain the Cu–Al–Ni thin films. In one of the methods applied, multilayers of Cu-Ni and Al were first sputtered, followed by heat treatment and quenching in iced water while, in the other method, epitaxial growth of austenitic Cu–Al–Ni on MgO substrate was obtained by sputter deposition along with in-situ heat treatment. Morphological characterization of the samples was carried out by scanning electron microscopy (SEM). X-ray diffraction (XRD) and transmission electron microscopy (TEM) were used for structural characterization. For the investigation of magnetic properties of the bismuth ferrite films, vibrating sample magnetometry (VSM) was implemented. In order to observe the martensitic transformation behaviour in the sputter deposited Cu–Al–Ni films, electrical resistivity measurements with respect to temperature were carried out. The morphology of the Bi particles was investigated as a function of the bath composition, substrate activity and the applied potential. In all cases, it was seen that as the absolute value of the applied potential increased, an evolution in the particle morphology from hexagons to dendrites was observed. Moreover, Bi particles were more uniformly distributed over the substrate when sodium gluconate was added to the electrolyte. The characterization studies for the  $\text{BiFeO}_3$  films prepared by electrodeposition and subsequent heat treatment revealed that rhombohedral  $\text{BiFeO}_3$  (interesting for its multiferroic character) formed around 600 °C. At lower and higher temperatures, secondary binary and ternary oxide phases were encountered. The observed weak ferromagnetic-like behaviour in the film annealed at 600 °C is mainly ascribed to nanostructuring which, in turn, favours the occurrence of spin canting in the  $\text{BiFeO}_3$  phase. In the free-standing Cu–Al–Ni films prepared by sputter deposition and subsequent heat treatment, it was observed that a gradual change in the film composition (i.e. decrease in the Al content and an increase in the Ni content) resulted in a shift in the room temperature phase formation from martensite to austenite. The obtained films exhibited a randomly oriented polycrystalline structure. On the other hand, for the austenitic Cu–Al–Ni film grown at high temperature on MgO substrates, a (200) textured growth of the film was observed due to the epitaxial relationship between the film and the substrate. The electrical resistance change vs. temperature measurements revealed that martensitic transformation was observed in the textured austenite film whereas it was not observed in the randomly oriented austenite film. The potential of the materials investigated throughout this Thesis as sustainable candidates in micro- and nanosystems is outlined.



# Contents

<b>Objectives.....</b>	<b>1</b>
<b>1.Introduction.....</b>	<b>3</b>
<b>1.1 Sustainability for Novel Technologies .....</b>	<b>3</b>
1.1.1 Concept of Sustainability .....	3
1.1.2 Sustainability for Microelectromechanical Systems (MEMS).....	4
1.1.3 Fabrication of MEMS/NEMS .....	5
1.1.4 Sustainable Material Selection for Coating Technologies .....	7
<b>1.2 Electrodeposition as a Fabrication Technique .....</b>	<b>9</b>
1.2.1 Theoretical Concepts in Electrodeposition .....	9
1.2.2 Electrodeposition Methods.....	11
1.2.3 Codeposition of Two Species.....	12
1.2.4 Parameters of Electrodeposition.....	13
<b>1.3 Sputter Deposition as a Fabrication Technique .....</b>	<b>16</b>
1.3.1 Theoretical Concepts of Sputtering.....	16
1.3.2 Sputtering Configurations .....	20
1.3.3 The Effects of the Energy of the Depositing Species on Deposit Properties .....	22
1.3.4 Sputter Deposition Targets.....	23
1.3.5 Process Control in Sputter Deposition .....	24
<b>1.4 Electrodeposition of Bismuth and Bismuth Based Compounds .....</b>	<b>25</b>
1.4.1 Electrodeposition of Bismuth.....	25
1.4.2 Electrodeposition of Bismuth (III) Oxide .....	27
1.4.3 Electrodeposition of Bismuth Vanadate.....	28
1.4.4 Electrodeposition of Bismuth Ferrite .....	29
<b>1.5 Sputter Deposited Shape Memory Alloys .....</b>	<b>30</b>
1.5.1 Shape Memory Alloys.....	30
1.5.2 Sputtered Shape Memory Thin Films .....	34
1.5.2.1 Ni–Ti and Ni–Ti–X (with X=Cu, Pd, Hf) Thin Films .....	34
1.5.2.2 Cu–Al–Ni Thin Films.....	35
1.5.2.3 Magnetic Shape Memory alloys: Fe-Pd and Ni-Mn-Ga.....	36
<b>1.6 Size Effects of Shape Memory Alloys .....</b>	<b>37</b>
<b>References.....</b>	<b>39</b>

<b>2. Experimental Methods.....</b>	<b>47</b>
<b>2.1 Film Synthesis.....</b>	<b>47</b>
2.1.1 Electrodeposited Films.....	47
2.1.1.1 Deposition Conditions.....	48
2.1.1.2 Cyclic Voltammetry Studies.....	50
<b>2.2 Sputter Deposited Films .....</b>	<b>50</b>
2.2.1 Room Temperature Sputter Deposition.....	50
2.2.2 High Temperature Sputter Deposition .....	51
<b>2.3 Heat treatment.....</b>	<b>52</b>
2.3.1 Equilibrium Heat Treatment.....	53
2.3.2 Post-quenching.....	55
<b>2.4 Thickness Measurement .....</b>	<b>53</b>
<b>2.5 Scanning Electron Microscopy (SEM) .....</b>	<b>54</b>
<b>2.6 X-ray Diffraction (XRD) Method .....</b>	<b>56</b>
<b>2.7 Transmission Electron Microscopy (TEM) .....</b>	<b>60</b>
<b>2.8 Vibrating Sample Magnetometry (VSM).....</b>	<b>62</b>
<b>2.9 Electrical resistance (ER) –Temperature (T) Measurements .....</b>	<b>64</b>
<b>References.....</b>	<b>65</b>
<b>3. Results and Discussion.....</b>	<b>66</b>
<b>3.1 Electrodeposition of Bismuth .....</b>	<b>66</b>
3.1.1 Cyclic Voltammetry (CV) Studies.....	66
3.1.2 Potentiostatic Deposition and Morphological Characterization of Deposits .....	68
3.1.3 X-ray Diffraction Analysis.....	72
<b>3.2 Electrodeposition of Bismuth Ferrite followed by Heat Treatment .....</b>	<b>75</b>
3.2.1 Electrochemical Deposition .....	75
3.2.2 Structural and Morphological Characterisation .....	77
3.2.3 Magnetic Characterisation.....	80
<b>3.3 Sputter Deposited Cu–Al–Ni Shape Memory Thin Films .....</b>	<b>82</b>
3.3.1 X-ray Diffraction Analysis.....	82
3.3.2 Transmission Electron Microscopy Studies.....	84
3.3.3 Resistance vs Temperature Measurements .....	85
<b>References.....</b>	<b>87</b>
<b>4. General Conclusions .....</b>	<b>89</b>
<b>5. Future Perspectives .....</b>	<b>91</b>
<b>Scientific CV .....</b>	<b>93</b>

## Objectives

Within the scope of this Thesis, fabrication of sustainable materials with the potential to act as substitutes for conventionally preferred materials to be used in micro/nanosystems was targeted. Sustainable materials comprising bismuth, bismuth ferrite and shape memory copper-aluminium-nickel alloy systems were studied. Electrodeposition was used in the synthesis of bismuth (Bi) and bismuth ferrite ( $\text{BiFeO}_3$ ) while sputter deposition was used in the synthesis of copper-aluminium-nickel (Cu–Al–Ni) shape memory system. Morphological, structural and magnetic properties of the synthesized materials were investigated. The main objectives of the Thesis can be outlined as follows:

- To examine the electrochemical behaviour of bismuth (Bi), which is an eco-friendly non-toxic semi-metal, by manipulating electrodeposition parameters such as bath composition, applied potential and substrate activity. The main purpose is being capable of tuning the deposited particle morphology in materials with large surface-to-volume ratio. Morphological and structural characterization was utilized in order to show how the morphological evolution of Bi particles could be kept under control within a narrow potential window.
- To synthesize bismuth ferrite ( $\text{BiFeO}_3$ ) films by electrodeposition and subsequent heat treatment as a bismuth based multiferroic compound and a sustainable substitute candidate for lead-zirconate-titanate (PZT). The dependence of the phase composition to applied heat treatment temperature was investigated. The origin of the weak ferromagnetic-like behaviour in the obtained films depending on the nanoscale structure and the phase composition was analysed.
- To synthesize Cu–Al–Ni shape memory alloys with 4-7 wt% nickel as a more sustainable candidate for the widely used Ni–Ti with 55 wt% nickel, which is a highly allergenic metal. With the purpose of making a comparison between compositional and structural properties and martensitic transformation behaviour, polycrystalline and epitaxial Cu–Al–Ni films were prepared by sputter deposition



# 1. Introduction

## 1.1 Sustainability for Novel Technologies

### 1.1.1 Concept of Sustainability

Sustainability is the socio-ecological process of pursuing a common ideal to support the endurance of biological systems. It has three key pillars: environmental protection, social responsibility and economic practice (Figure 1.1) [1,2].

Green initiatives entailing material selection and process design are an important aspect of environmental domain of sustainability. Sustainability must be considered starting from materials selection and process design to product finishing in all industrial processes. Recycling and reclamation efforts must be performed accordingly.

Providing essential training programs constitute an important social aspect of sustainability. It is also quite important for industrial and academic organizations to pay attention to compliance with regulations issued by foundations devoted to environmental issues.

Capital improvements and new market development on green materials is an essential part of the economic pillar of sustainability. Setting forth and remaining in compliance with principles of sustainability in product design and manufacturing is an indispensable part of process implementations.

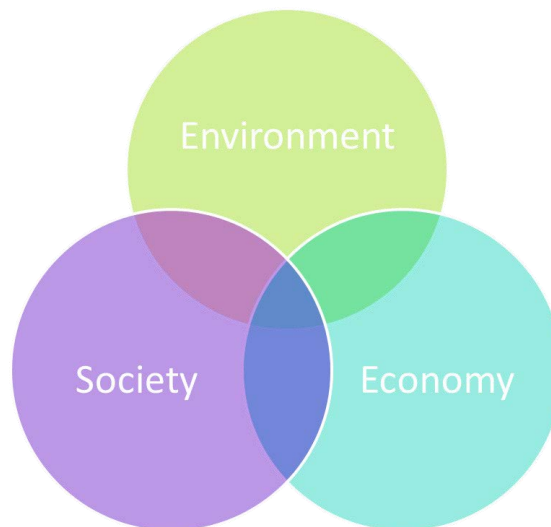


**Figure 1.1 Environment, economy and society should act together for sustainable development**

Making sustainability a part of the global system is a challenge that encompasses law, urban planning, transport, social and individual lifestyles and ethical consumerism. Reorganizing living conditions by creating sustainable cities, reappraising economic sectors like construction and agriculture and using science to develop green technologies and renewable energy are essential for moving toward sustainability.



### 1.1.2 Sustainability for Microelectromechanical Systems (MEMS)

In now-a-days' rapid-growing world, downsizing is seen in all conventional technologies and micro/nanoplatforms have come into focus of many new market developments. For instance, the commercial FeNi, permalloy, notable for its high magnetic permeability, acts as a magnetic core in electric and electronic equipment. The fact that it has almost zero magnetostriction along with high magnetic permeability makes FeNi thin films a favourable choice for MEMS industry as large variations in magnetic properties due to variation in stresses would not be tolerated in industrial processes. Even though FeNi a suitable choice to utilize in industrial applications, it consists of approximately 80 (wt%) Ni which is classified as a highly allergenic metal regarding the regulations issued by European Commission (see section 1.1.4). While miniaturizing, it is also crucial to take sustainability principles into consideration. While the fabrication methods (see section 1.1.3) for MEMS bring long-term profits as they enable development of systems with reduced volume and energy consumption, designing sustainable products by making substitutions in material precursors is a serious concern as well (see 1.1.4).

The definition of MEMS can be made as the entirety of the process technologies utilized to form integrated miniaturized devices or systems that combine mechanical and electrical components. In nanoelectromechanical systems (NEMS) their size decreases down to few nanometers. The significance of MEMS is that the effect that they generate is on the macroscale while they are capable of sensing, controlling and actuating on the microscale.

MEMS can be divided into four sub-groups such as microstructures, microsensors, microelectronics and microactuators each of which require individual synthesis approach at micro/nanoscales (Figure 1.2) [3].

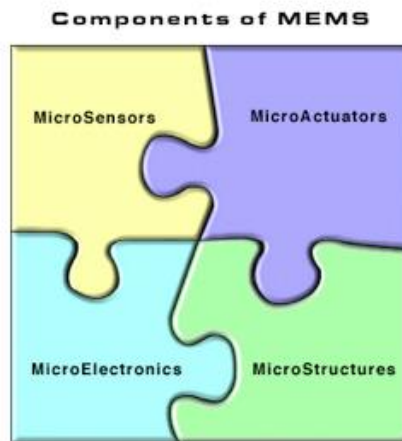


Figure 1.2 Components of MEMS [4]

### **1.1.3 Fabrication of MEMS/NEMS**

#### **Film Deposition**

Deposition technology can be regarded as the major method to fabricate materials for micro/nanodevices and it can be categorized into chemical and physical deposition techniques.

##### ➤ **Chemical Deposition**

In this group of deposition techniques, a fluid precursor goes through a chemical change at a solid surface and leaves a solid layer on the surface. Some of the chemical deposition methods are briefly summarized below:

- **Sol–Gel Method**

It is the process of the settling of (nm sized) particles from a colloidal suspension onto a substrate, forming ceramic materials as a result. The desired solid particles are suspended in a liquid, forming the 'sol', which is deposited on a substrate by spinning, dipping or coating, or transferred to a mould. The particles in the sol become polymerised by partial evaporation of the solvent, or addition of an initiator, forming the 'gel', which is then heated up to form the final product [5].

- **Spin Coating**

In this technique, a liquid precursor is coated onto a flat substrate that is rotated at a high velocity to centrifugally spread the solution over the substrate. The spinning speed and the viscosity of the precursor determine the thickness of the film. A final heat treatment brings the final product [6].

- **Dip Coating**

Dip coating is applied by having a substrate submerged in a liquid precursor. The substrate is withdrawn from the solution under controlled conditions by varying parameters such as speed of the withdrawal, evaporation conditions, and solvent viscosity. The homogeneity, thickness and morphology of the film can be varied by manipulating these parameters [7].

- **Chemical Vapour Deposition (CVD)**

Chemical vapour deposition (CVD) is described as the deposition of a solid on a heated surface from a chemical reaction in the vapour phase. It belongs to the class of vapour transfer processes. The main product is deposited onto the substrate whereas the by-products get pumped out. The process parameters are the reaction rate, gas transport and diffusion [8].

- **Atomic Layer Deposition (ALD)**

ALD is a self-limited film growth method that is characterized by alternating exposure of the growing film to chemical precursors, resulting in the sequential deposition of (sub)monolayers [9].

- **Electrodeposition**

Electrodeposition is a surface treatment technique in which an external electric current is used to induce the reduction of dissolved metal cations in a liquid electrolyte in a way that they form a coating on an electrode acting as a substrate (see chapter 1.2).

- **Physical Deposition**

In general terms, in physical deposition, mechanical, electromechanical or thermodynamic means are induced to synthesize a thin solid film. Some of the commonly used physical deposition methods are succinctly mentioned below:

- **Electron Beam Evaporation**

This is a form of vapor deposition in which a target anode is bombarded with an electron beam given off by a charged tungsten filament under high vacuum. The electron beam causes atoms from the target to transform into the gaseous phase. These atoms then precipitate into solid form, coating everything in the vacuum chamber (within line of sight) with a thin layer of the anode material [10].

- **Molecular Beam Epitaxy**

Molecular beam epitaxy (MBE) is a finely controlled method for growing single-crystal epitaxial films in a high vacuum ( $10^{-11}$  Torr). The films are formed on single-crystal substrates by slowly evaporating the elemental or molecular constituents of the film from separate Knudsen effusion source cells (deep crucibles in furnaces with cooled shrouds) onto substrates held at a temperature appropriate for chemical reaction, epitaxy, and re-evaporation of excess reactants [11].

- **Sputter Deposition**

Sputter deposition is based on the principle of having a material ejected from a target source to a substrate (see chapter 1.3).

- **Pulsed Laser Deposition (PLD)**

It is a process that works by ablation process. A target material surface is vaporized by pulses of focused laser light. The vapor is converted to plasma and this plasma reverts to a gas before it coats the substrate [12].

- **Thermal Spraying**

Thermal spraying can be applied either in atmospheric conditions or in a vacuum chamber at low pressure. In this method, the coating material in powdered form is applied to the surface using a carrier gas in plasma flame with a certain amount of mechanical force [13].

Aside from the deposition techniques, applying patterning is effective in increasing the alternatives for MEMS. It is often desirable to pattern a film into distinct features or to form openings in the material. These features are on the micrometer or nanometer scales. The patterning technique typically uses a 'mask' to define portions of the film which will be removed. In the process, the pattern of the mask is transferred to the material to be fabricated [14]. Patterned surfaces allow fabrication of 3D systems such as nanowires and nanopillars.

#### **1.1.4 Sustainable Material Selection for Coating Technologies**

The future constraints on energy use will apply more pressure to use materials in the most cost-effective way possible. As raw materials become scarcer, it is necessary to use them as efficiently as possible. Additionally, implementing all required surface technology operations in an ecologically and environmentally responsible manner is becoming a more important issue every day. This pushes researchers to design materials by avoiding use of toxic and scarce precursors. For electrodeposition, minimization of raw materials, energy use and disposal of waste products are key points emphasized in currently applied rules and regulations. Physical deposition methods emerge as environmentally friendly methods which produces less waste as dry coating methods [15]. Designing materials without or with minimum amounts of scarce and toxic elements with certain compositional restrictions should be taken into account. Some important points that must be raised for material selection for coating technology products are outlined below:

##### **Minimization of Critical Raw Materials**

Use of noble metals and rare earth metals is highly restricted because they are highly costly and hard to access [16].

For example, Sm–Co-based and Nd–Fe–B based alloys are the most widely used products for hard-magnetic applications. The necessity of using rare earth metals in order to obtain the required hard magnetic properties have led new alternative alloy systems with more appropriate prices and higher accessibility to be searched. For this reason, Mn-based alloys such as MnBi, MnGa, MnAl [17] are arising as promising candidates to replace the dominant products of the market.

Regarding magnetostrictive alloys, Fe–Pd, which is Fe–rich with around 70 at%, is a suitable candidate to replace the  $Tb_xDy_{1-x}Fe_2$ , Terfenol, which is a very widely used magnetostrictive material [18].

### **Minimization of Nickel and Cobalt**

Nickel and cobalt use is quite widespread in the MEMS market. However, nickel and cobalt are highly allergenic metals [19]. Directive EN 1811 issued by European Commission must be taken into consideration for technological devices that might be in contact with human skin [20]. Besides, cobalt salts are among high concern substances [21] and cobalt price sharply increased in the recent years [22]. Some examples for alternative material selections that can be employed for widely used MEMS products are given below:

NiTi is the mostly commonly used shape memory system. It is used in many fields ranging from biomedicine to thermal and electrical actuation. However, among the copper based shape memory alloys, Cu–Al–Ni stands out due to having a quite large superelastic recovery. Moreover, Cu–Al–Ni shape memory alloys have approximately 5 (wt%) of nickel compared to Ni–Ti system shape memory alloys which have around 50 (wt%) of Ni. Also, Cu–Al–Ni is a more cost-effective choice compared to Ni–Ti as titanium is a highly costly metal [23].

Also, alloys such as Ni–Co and Fe–Co are utilized due to their high magnetostrictive properties. Increasing the iron based alternatives is crucial to create more sustainable materials for magnetostrictive alloys.

### **Bismuth for Lead Replacement**

Lead is a metal which possesses a number of attributions such as high density, low melting point, ductility, inertness to oxidation, relative abundance in earth's crust and low-cost. The qualities made it a highly preferred metal for a wide range of applications from solders to radiation shielding until its toxic impacts started to come into focus of researchers. The fact that elevated concentrations of lead persist in soil and accumulates over time in soil and water caused long-term hazards for the environment and living organisms. For this reason, tendencies towards creating alternatives for lead use initiated. As a consequence of this, due to its similar physical and chemical properties to lead, bismuth emerged as an option.

In spite of its location among highly toxic metals such as lead, arsenic and antimony, bismuth earned the status of 'green element' due its non-toxic nature [24]. This is most probably due to the relatively low solubility of bismuth salts in living organisms [25]. For medical applications, bismuth is selected due to being non-toxic. For instance, bismuth is used in bismuth-impregnated latex shields to shield from X-ray in medical examinations [26]. Pure bismuth is also an alternative to mercury electrodes to be used in stripping voltammetry of trace metals owing to its high reproducibility [27].

The fact that bismuth expands over solidification makes it a convenient candidate to be used in typesetting alloys to fill printing moulds. It has become a replacement for the toxic heavy metal lead for soldering alloys with low melting points [28, 29]. Bismuth based solders also find uses in food processing equipment, copper water pipes and automobile industry [30]. It has also replaced lead in free machining brasses for plumbing

applications [31]. Owing its ferroelectricity BiFeO<sub>3</sub> is a good candidate to replace lead-zirconium-titanate (PZT) [28]. Also, bismuth has been used as a substitution for lead as lead shot for hunting birds is now prohibited [24].

## **1.2 Electrodeposition as a Fabrication Technique**

Electrodeposition is a surface treatment method that has various advantages. It works at ambient pressure with a simple set-up. It is a cost-effective method that enables the growth of films of several micrometres in thickness. Traditionally used for improving decorative or corrosion resistance properties of materials, recently electrodeposition attracts attention with its potential for the synthesis of components for micro/nanosystems. Also, electrodeposited alloys are used in a wide range of fields. Some examples are given below [32]:

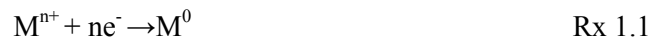
- ✓ Protective-decorative: Ni–Zn, Ni–Au, Ni–Cd, Ni–Sn, Au–Cu, Au–Ag, Cu–Sn
- ✓ Corrosion resistance: Zn–Cd, Zn–Sn, Cd–Sn, Cr–Ni, Cr–Re, Cu–Ni
- ✓ Soldered coatings: Sn–Pb, Sn–Bi, Sn–Sb, Sn–Ni, In– and Bi–based alloys
- ✓ Heat-resistance alloys: Ni–Co, Ni–Fe, Ni–Fe–Co, Co–W, Co–Pt, Fe–Pt, Cr–Mn, Cr–W, Cr–Mo
- ✓ Magnetic alloys: Ni–Co, Ni–Fe, Ni–Fe–Co, Co–W, Co–Pt, Fe–Pt
- ✓ Coatings replacing individual noble metals in electronics and jewellery: Pd–Ni, Au–Ni, Au–Co
- ✓ Antifriction alloys: Pb–Ag, In–Pb, Pb–Cu, Ag–Sn
- ✓ Adhesion coatings: Cu–Zn
- ✓ Electric contact coatings: Ag–Sb, Ag–Pd, Au–Pd, Pd–Ni, Au–Ni, Au–Sb, Pd–In

### **1.2.1 Theoretical Concepts in Electrodeposition**

Electrodeposition is a surface treatment method based on the principle of coating a working electrode with another material which is present in the ionized state in an electrolyte. Mobilizing the charges in an electrolyte cannot be achieved only with the presence of a single electrode/electrolyte interface. A potential difference must be formed in the bath which would determine the thermodynamic conditions for the process. Therefore, electrical energy is involved for the process for the potential difference to form. For electrodeposition experiments to take place, electrochemical cells are required. The working principle of an electrochemical cell can be explained as generating electrical energy from chemical reactions or inserting electrical energy in order to facilitate chemical reactions. Electrochemical cells are divided into two groups, namely galvanic (voltaic) cells in which reactions take place spontaneously and electrolytic cells in which non-spontaneous reactions take place. Electrodeposition takes place in electrolytic cells. Regardless of the cell type, the reactions in electrochemical cells are driven by oxidation/reduction mechanism. Oxidation reactions occur at the anode whereas the reduction reactions take place at the cathode. The potential is the representative of the energy available to drive charges between the electrodes and its magnitude manipulates the direction and the rate at which the charges are transferred between two interfaces. In an electrolytic cell, a direct current (DC) source

(power supply), mostly a rectifier or motor generator, provides a current flowing in one direction through the external portion of the circuit when a potential difference is imposed across the system. The current flow of electrons goes on in the externally connected wires (external circuit). The electrical transfer in solution is through electrically charged species named as ions. Positive ions (cations) move towards negative electrode (cathode) and negative ions (anions) travel toward the positive electrode (anode) when the potential is applied to have the electrical circuit completed. Anodic or cathodic electrodeposition can take place depending on whether the materials form by oxidation or reduction mechanism [32].

In cathodic electrodeposition metal ions are reduced on conductive substrates that function as the working electrode. The overall reduction can be summed up as:



Reduction of  $H_{(aq)}^{+}$  ions to  $H_{2(g)}$  can also accompany the metal reduction and fuse into the deposit which might cause deterioration in the mechanical properties of the coating.



### **Faraday's Laws**

Faraday's laws for electrolysis state the principles for electrodeposition. They are related to current density, time and equivalent weight of the metal with the weight of the reduced material. They can be summarized as follows [32]:

- i. The deposited substance through electrolysis is proportional to the quantity of electricity passing through the electrode.
- ii. The amount of electricity required to produce 1 mole of a substance is a simple entire number multiple of a constant  $F = 96485 \text{ C/mol}$ .

The Faraday's law of electrolysis is mathematically expressed as:

$$W = \frac{Q \cdot A}{n \cdot F} \quad \text{Equation 1.1}$$

$W$ : the deposited mass weight (g)

$Q$ : total charge (C),  $Q = I \cdot t$ ,  $I$ : current (A),  $t$ : time (s)

$A$ : Molecular weight (g/mol)

$n$ : the valence number of the ion

$F$ : 96485 C/mol

Occurrence of 100% efficiency is assumed in Faraday's law. Secondary reactions such as H<sub>2</sub> evolution or chemical reactions occurring that might decrease the efficiency are not taken into account. Nevertheless, it is helpful in estimating the upper weight limit of the reduced mass approximately.

## Electrode Cell

There are two types of cell configurations [32]:

In a two-electrode cell, there is a conductive substrate that works as the working electrode (WE) and, depending on the requirement of the application, an inert metal or a sacrificial anode is used as the counter electrode (CE) (Figure 1.3 left).

In a three electrode cell, in addition to the presence of WE and CE, there is a reference electrode (RE) which has a known and fixed potential (Figure 1.3 right).

In a two electrode-cell, just the current flowing between the two electrodes can be observed, while in a three-electrode cell we can in addition monitor precisely the potential at the WE.

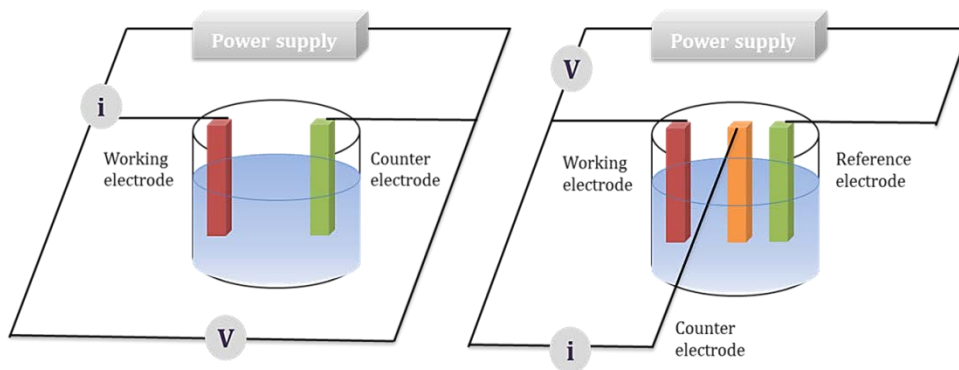


Figure 1.3 Scheme of two electrode cell (left) and three electrode cell (right)

### 1.2.2 Electrodeposition Methods

Direct and pulsed methods are the two main electrodeposition approaches one can follow [32]:

#### Direct Deposition

Potentiostatic deposition: A potential difference is applied externally between the WE and RE and it is held constant while the current passing through the WE is measured as a function of time.

Galvanostatic deposition: A constant current is applied between the WE and CE and the potential is measured between the WE and RE over time.



## **Pulsed Deposition**

Here the applied potential or current is periodically pulsed.

Pulsed deposition: The potential or current is alternated between two different values. As a result of this, a series of pulses of equal amplitude, duration and polarity, separated by zero current is obtained. It is the method of choice for the growth of multi-layered metallic nanowires in porous anodic alumina or polycarbonate templates.

Reversed pulsed deposition: The deposition current is periodically interrupted and a dissolution time is introduced into the deposition cycle. Reverse pulsed deposition shows the same effect in replenishing the diffusion layer as pulsed deposition and selectively dissolves the protrusions of the metal surface to ensure good uniformity in the deposit.

### **1.2.3 Codeposition of Two Species**

For the successful codeposition of two species, X and Y, X being the nobler one, to take place, certain points should be taken into consideration [32]:

- 1) Deposition of X at the limiting diffusion current.

Reduction of component Y requires a potential which is reached by depleting the cathodic solution layer of ions of component X such as generating a concentration polarization and at the same time an increase in the charge transfer overpotential for X.

Dendritic deposits and powdery formation is usually encountered at the limiting current. Additionally, the fraction of X species incorporated in the material is limited by the concentration of X. Under these circumstances, involvement of surface-active substances (SASs) in electrolytes can prevent dendritic growth (Figure 1.4).

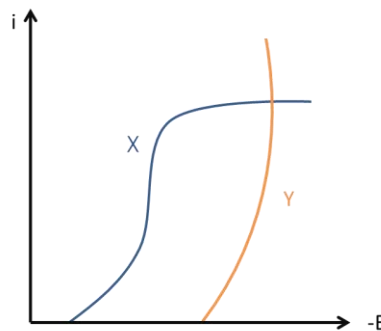


**Figure 1.4 Electrodeposition of component X at the limiting diffusion current: the two curves represent the partial currents for components X and Y**

- 2) The simple addition of SASs may be sufficient to make alloy formation possible (Figure 1.5).

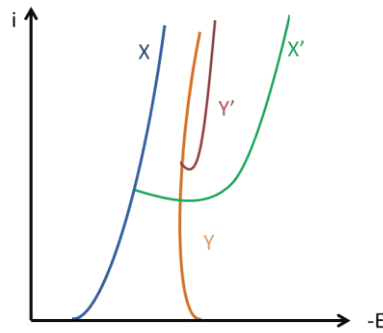


**Figure 1.5** Change in partial current curves for components X and Y after the introduction of SASs: X and Y designates them in the absence of SASs; X' and Y' are the curves in the presence of SASs

- 3) Complex formation between X or X and Y with ligands introduced into the solution.

Widely used ligands such as cyanides, ammoniates, pyrophosphate, tripolyphosphates, aminoacetic and other organic acids like trilon B, gluconates, citrates form complex compounds with several metal ions in the bath. Complexes of electropositive species generally have high stability constants and feature higher polarizability and consequently, they have the tendency to bring the deposition potentials close to each other (Figure 1.6).

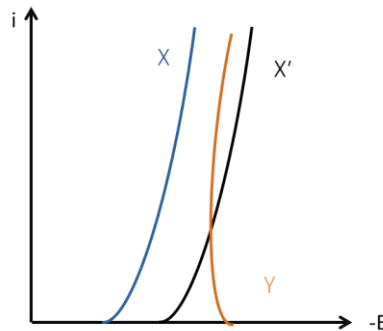


**Figure 1.6** Variation of the partial current curve of component X upon complex formation

- 4) Use of solutions concentrated in Y but diluted in X. It requires dilution by approximately two orders of magnitude or more.

### 1.2.4 Parameters of Electrodeposition

Electrolytic bath composition is one of the key parameters in any electrodeposition process. The remaining variables of the process are quite dependent on the flexibility of the bath. However, there are some rational approaches that allow their effect on deposit qualities such as morphology, structure, composition and its properties [32].

**Current density:** Near the electrode surface, a concentration gradient in the electrolyte forms where ions become reduced. The concentration change takes place at the diffusion layer at the electrode/electrolyte

interface. The ion charges to be reduced accumulate and become reduced at this interface as a consequence of applied potential (Figure 1.7, region I) however, the continuity of the reduction process is also dependent on the mobility of these ions. As the diffusion layer thickens as a result of the charge accumulation at the interface, no change in the current density starts to be observed despite the increase in applied potential (Figure 1.7, Region II). The value where the current density reaches a plateau is called the limiting current density. The limiting current density value of this plateau is dependent on the equilibrium potential of the metal cations to be reduced and the hydrogen overpotential of the electrode surface. As the cathode potential keeps on increasing an instant increase in the current density takes place which is due to co-reduction of more electronegative ions such as  $H^+$  along with the metal cations (Figure 1.7, Region III).

In two component systems, applying high current densities, results in an increase in the overpotential and hence in an increase of the less noble metal component in the deposit.

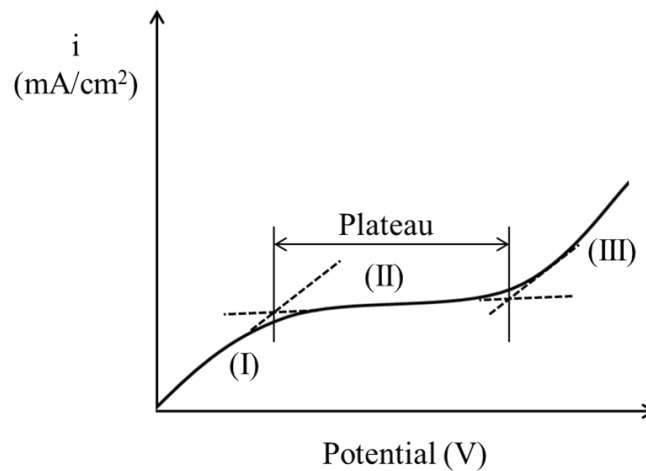


**Figure 1.7 Typical current potential curve and transition between regions I and II to determine the limiting current density**

**Temperature:** Temperature increase causes a decrease in the cathode polarization. Activation polarization decreases with increasing temperature due to the fact that exchange current density rises rapidly with temperature. Concentration polarization drops as a result of the increase of material concentration in the diffusion layer at cathode surface.

**pH:** It is the activity of the solvated hydrogen ion related to the hydrogen ion concentration in the electrolyte. During electrolysis, hydrogen evolution occurs with other reduction reactions, which is a fact that decreases the deposit quality. The inconstancies in pH value remarkably affect the cathodic current efficiency of the process. Working at higher pH values and having wetting agents in the bath is helpful at decreasing hydrogen evolution.

**Air agitation (O<sub>2</sub>, N<sub>2</sub>, Ar):** Air agitation by low pressure blowers is useful at removing hydrogen bubbles formed at the cathode. Also, N<sub>2</sub> or Ar bubbling before electrodeposition helps remove dissolved O<sub>2</sub> in the solution, which might be needed when fully metallic materials prone to oxidation are targeted (e.g. Fe).

**Additives:** To have deposits formed with high quality and well defined properties, selection of appropriate SASs (or simply additives) is very significant. Additives are quite functional in regulating various issues related to electrodeposition, from preventing non-adherence to formation of films with undesired properties such as presence of dendritic morphology. Metal ions show variation in their susceptibility to the effects of additives. The main effects of additives are often regulated by changing the polarization characteristics of the cathode. It is assumed that they operate by adsorption on the substrate or by forming a complex with the metal.

Additives can be classified as follows [32]:

**Complexing agents:** In a bath consisting of the salts of different metals, the preferential deposition of the more noble material is to be more dominant in the deposit as the components have different reduction potentials. In order to increase the incorporation of the less noble material, complexing agents are helpful at bringing the reduction potentials of the two species together.

**Grain refiners:** The grain dislocations and the number of the nuclei formed determine the dimensions of the grains. Addition of organic additives such as saccharin, coumarin or thiourea induce disorder during the deposition of the ad-atoms into the lattice of the growing deposit or inhibit surface diffusion of ad-atoms towards growing centres. Also, applying pulsed deposition or use of high current densities or overpotentials leads to a high degree of supersaturation of the surface ad-atoms and helps in obtaining a decrease in the crystal size of the grain formed.

**Dendrite and roughness inhibitors:** These additives function by adsorbing onto the surface and covering it with a thin layer which acts as an inhibitor for the growth of the dendrites. These additives can be organic or inorganic substances.

**Levelling agents:** Typically, in electrodeposition, due to formation of more deposit in the peaks of the cathode compared to the valleys, the resulting coating exhibits rough surfaces. The current density is higher at the peaks due to the electric field strength in the region. In order to obtain smooth and shiny surfaces, more material must be deposited at the valleys. In order to provide this, levelling agents are used. They are absorbed preferentially on the peaks of the substrate to prevent the deposit growth at these spots.

**Brightening agents:** Mechanical finishing is of importance in the as-deposited products both for decorative and functional purposes. Typically, fine grained deposits have highly reflective surfaces. Brightening agents are effective in providing high reflectivity along with grain refinement.

**Wetting agents or surfactants:** They prevent pit and pore formation in the deposit because they promote H<sub>2</sub> bubbles to be removed from the cathode.

### 1.3 Sputter Deposition as a Fabrication Technique

Sputtering is an advantageous surface treatment method which allows the deposition of any element, alloy or compound. A range of geometries can be coated by sputtering. The configurations and targets can easily be scaled regarding the needs of the processes. The conditions of sputtering are easily reproducible from run to run. It has faster deposition rates compared to vacuum evaporation also allowing for close source-substrate spacing. It is also a clean method with no production of considerable wastes [33,34].

Examples for the materials that can be prepared by sputtering can be mentioned as follows [33]:

- ✓ Single and multilayer metal conductor films for microelectronics and semiconductor devices, e.g. Al, Mo, Mo/Au, Ta, Ta/Au, Ti, Ti/Au, Ti/Pd/Au, Ti/Pd/Cu/Au, Cr, Cr/Au, Cr/Pd/Au, Ni–Cr, W, W–Ti/Au, W/Au.
- ✓ Compound conductor films for semiconductor electrodes, e.g. WSi<sub>2</sub>, TaSi<sub>2</sub>, MoSi<sub>2</sub>, PtSi.
- ✓ Barrier layers for semiconductor metallization, e.g. TiN, WTi (70 at%W–30 at%Ti) or (90wt%W – 10wt%Ti).
- ✓ Magnetic films for recording, e.g. Fe–Al–Si, Co–Nb–Zr, Co–Cr, Fe–Ni–Mo, Fe–Si, Co–Ni–Cr, Co–Ni–Si.
- ✓ Optical coatings – metallic (reflective, partially reflective), e.g. Cr, Al, Ag.
- ✓ Optical coatings – dielectric (anti-reflective and selective reflective), e.g. MgO, TiO<sub>2</sub>, ZrO<sub>2</sub>.
- ✓ Transparent electrical conductors, e.g. InO<sub>2</sub>, SnO<sub>2</sub>, In–Sn–O (ITO), ZnO–Al.
- ✓ Electrically conductive compounds, e.g. Cr<sub>2</sub>O<sub>3</sub>, RuO<sub>2</sub>.
- ✓ Transparent gas/vapour permeation barriers, e.g. SiO<sub>2</sub>, Al<sub>2</sub>O<sub>3</sub>.
- ✓ Diffraction gratings, e.g. C/W.
- ✓ Photomasks, e.g. Cr, Mo, W.

#### 1.3.1 Theoretical Concepts of Sputtering

Basically, sputtering is an etching process. It works with the principle of having a target surface bombarded with high energy species. This leads to the ejection of a vapour flux of the target material. Sputter deposition is the method in which this flux is used as a vapour source for film growth. The sputtered flux consists of atoms with energies typically ranging from a few eV up to a few 10 s of eV, moving away from the target at random angles. The target can consist of a single element, alloy or compound. Figure 1.8 shows the processes that occur at the surface, in the surface region, and in the near-surface region of the bombarded surface [33,34].

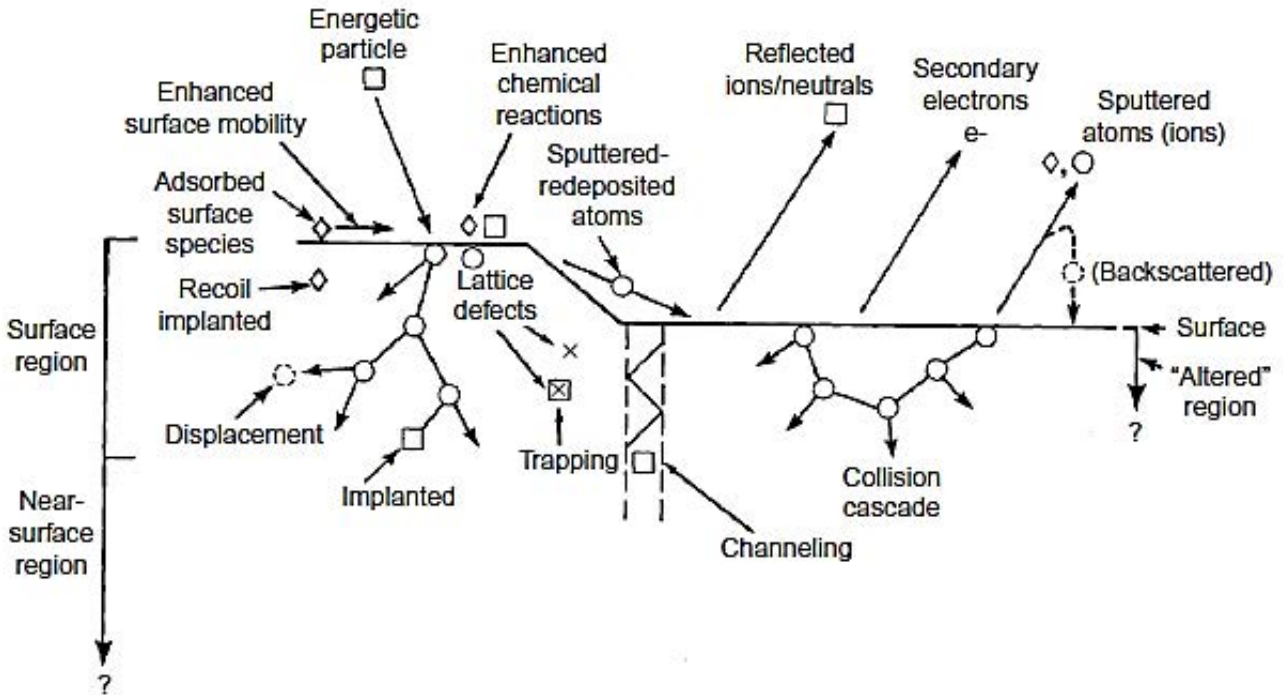


**Figure 1.8 The bombardment effects on a target surface [33]**

The bombarding particles might penetrate into the surface region, whereas the collision effects can occur into the near-surface region. The bombarding particle forms a collision cascade and some of the momentum is transferred to surface atoms, which may become ejected, thus sputtered. Most of the transferred energy (>95%) appears as heat in the surface region and near-surface region. Some of the bombarding particles get reflected as high energy neutrals and some become implanted into the surface.

For the sputter deposition to be implemented the conditions below must be provided:

- A good vacuum ( $<10^{-5}$  Torr).
- A low pressure gas environment in which sputtered particles are transported from the target to the substrate without gas phase collisions (i.e. pressure less than about 5 mTorr), using a plasma as the source of ions.
- A higher pressure gas where gas phase collisions and “thermalization” of the ejected particles occur but the pressure is low enough that gas phase nucleation is not important (i.e. pressure greater than about 5 mTorr but less than about 50 mTorr).

### **Sputtering Yield**

The sputtering yield is the ratio of the number of atoms ejected to the number of incident bombarding particles and depends on the chemical bonding of the target atoms and the energy transferred by collision. It is related to

the mass of the bombarding particles as well as their energy. It shows sensitivity for the angle of the bombarding particle. Figure 1.9 shows the relationship between the sputtering yields of some metals with respect to argon ion energy. There is a threshold energy below which sputtering cannot take place regardless of the intensity of the flux. Most sputtered atoms have higher kinetic energies than thermally evaporated atoms.

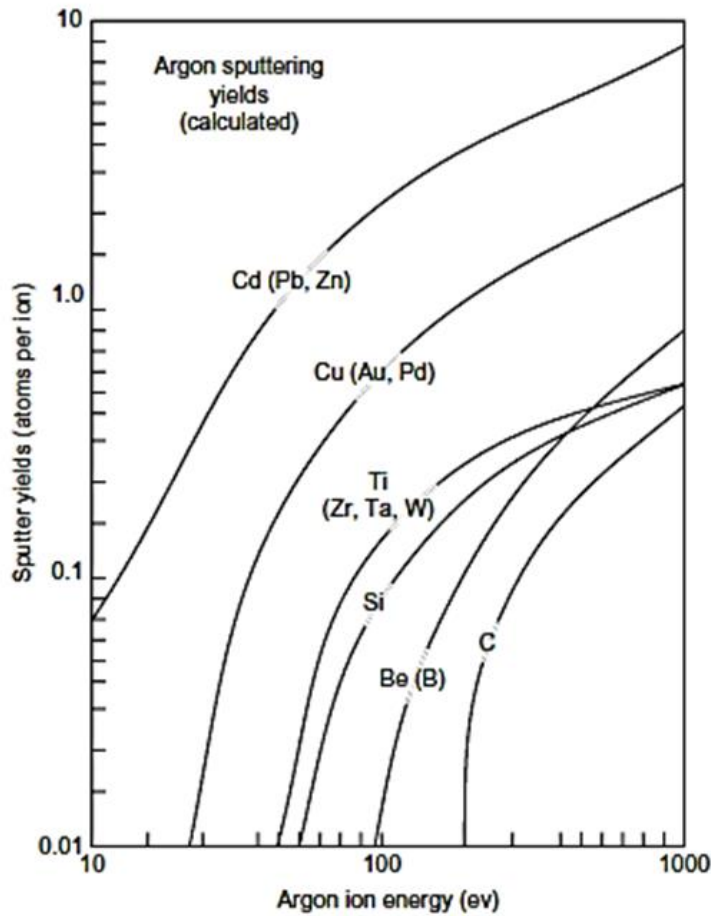


**Figure 1.9 The sputtering yields of some metals with argon ion energy [33]**

Sputtering yields are lower at higher kinetic energies causing atoms to lose their surface energy below the surface. No sputtering by electrons happens even at high temperatures. The secondary electron emission by ion bombardment is low while high rates from thermoelectronic emission can be expected if high temperatures were present [33,34].

The mass of the bombarding species determines the energy and momentum transferred to the film atoms during the collision. The energy,  $E_t$ , is given by the laws of conservation of energy and conservation of momentum (Equation 1.2).

$$E_t/E_i = 4M_tM_i \cos^2 \theta / (M_i + M_t) \quad \text{Equation 1.2}$$

Where,

$E$  = energy

$M$  = mass

$i$  = incident particle

$t$  = target particle

$\theta$  is the angle of incidence measured from line joining their centers of masses (as shown in Figure 1.10). The maximum energy is transferred when  $\cos \theta = 1$  (zero degrees) and  $M_i = M_t$ . Therefore, matching the atomic mass of the bombarding ion to the target atom is important to the sputtering yield. Examples of sputtering yield values for some elements are given in Table 1.1.

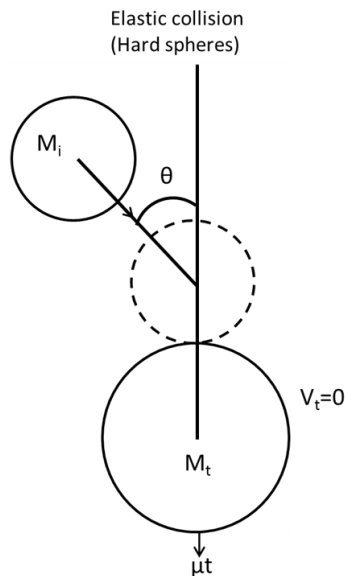


Figure 1.10 Collision of particles and the transfer of momentum

Table 1.1 Sputtering yield values for some elements [34]

Element	Sputtering Yield (atoms/ion) (for Ar at 500 eV)	Element	Sputtering Yield (atoms/ion) (for Ar at 500 eV)
Al	1.05	Ni	1.45
Au	2.40	Si	0.50
C	0.12	Ta	0.57

Sputtering yield for Al and Au using different bombarding gases are shown in Table 1.2.



**Table 1.2 Sputtering yield for Al and Au using different bombarding gases [34]**

Element	He (500 eV)	Ne (500 eV)	Ar (500 eV)	Ar (1000 eV)	Kr (500 eV)	Xe (500 eV)
Al	0.16	0.73	1.05	1.0	0.96	0.82
Au	0.07	1.08	2.40	3.6	3.06	3.01

### 1.3.2 Sputtering Configurations

Plasma based sputtering is the most commonly used sputtering form. In this method there is a plasma present and positive ions are accelerated to the target, which is at a negative potential with respect to plasma [33,34].

#### DC (Direct Current) Glow Discharge Sputter Deposition

Sputter deposition is generally achieved by means of a self-sustaining discharge in a low-pressure inert gas. The sputtering target acts as the cathode. In general, the substrate is placed on the anode, which is often at ground potential (Figure 1.11) [33,34].

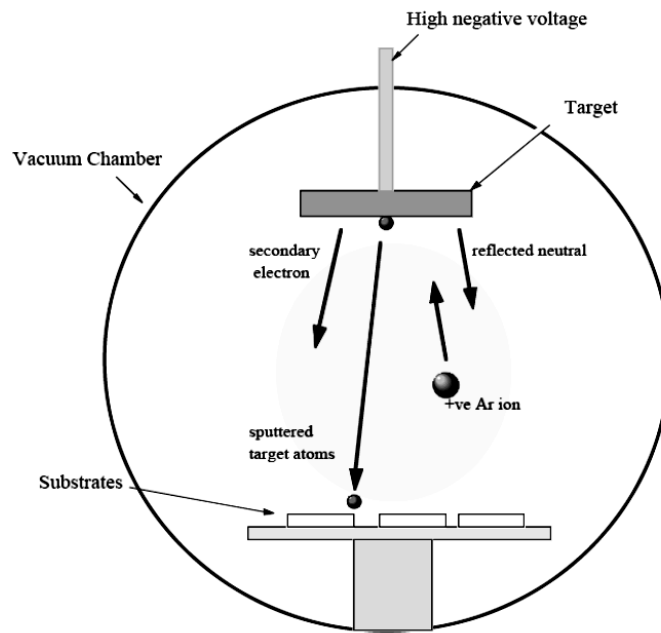


**Figure 1.11 Scheme of a sputter deposition equipment [34]**

In this method, the collision of ions with the cathode creates the secondary electrons. In turn, secondary electrons from the target surface get accelerated away from the cathode. Ions are formed due to the collision between these high energy electrons and atoms. Surfaces in the discharge chamber can be bombarded with some of these high energy electrons. This fact is not desired as it will heat the surfaces.

Sufficient gas pressure enabling a significant proportion of secondary electrons collide with gas atoms before they are lost to surroundings is required to have the discharge maintained. This corresponds to a pressure greater than a few Pa. The sputtered flux is supposed to travel through this gas to reach the substrates. However, if it is substantially scattered, it can coat the chamber walls and even being scattered back onto the target. Thus, this simple set-up is not quite efficient. Besides it is also dependent on the presence of a target with electrical conductance.

### **Radio Frequency Sputtering**

Sputter deposition of insulating materials (i.e. oxides, nitrides and ceramics) cannot be done with DC power as these materials have very large DC impedance and require very high voltages to create and maintain the plasma. Nevertheless, the impedance of these materials changes with the frequency of the applied power; hence, using power delivered at radio frequencies and an automatic impedance matching network, the total impedance of the circuit can be regulated and dielectric materials can be sputtered from the target. When an RF potential, with a large peak-to-peak voltage, is capacitively coupled to an electrode, an alternating positive/negative potential appears on the surface. During part of each half cycle, the potential is such that ions are accelerated to the surface with enough energy to cause sputtering, while, on alternate half cycles, electrons reach the surface to prevent any charge build-up. Radio frequencies used for sputter deposition vary between 0.5 to 30 MHz. The commercially used frequency is often 13.6 Hz. Lower pressure values are required for RF sputtering compared to DC sputtering. RF sputtering can be performed at lower gas pressures (<1mTorr) than those used for DC sputtering [33,34].

However, electron oscillations in an RF field can promote ionization and it becomes possible to maintain the discharge at slightly lower pressures. Magnetron sputtering provides solutions for the problems related to pressure [33,34].

### **Magnetron Sputtering**

Magnetron sputtering is a method that depends on the presence of a magnetic field developed at the target surface. It can be applied along with DC or RF sputtering techniques. Due to the formation of the magnetic field, the secondary electrons travelling away from the target surface can be trapped in a region of crossed electric and magnetic field leading to a cycloidal motion (Figure 1.11). As the electrons are kept near the target surface, their path length is increased and their residence time is prolonged. The collision probability is improved and denser discharge near the target surface that can be maintained down to lower pressure is obtained [33,34].

The planar magnetron configuration (Figure 1.12a) forms a vaporization source that consists of two parallel lines that can be of almost any length. It is the most common magnetron source. The principal advantage of this configuration is that dense plasma can form near the cathode at low pressures so that ions can be

accelerated from the plasma to the cathode without loss of energy due to physical and charge exchange collisions. This configuration allows sputtering at low pressures (<5 mTorr), where there is no thermalization of particles from the cathode, as well as at higher pressures (>5 mTorr), where some thermalization occurs [33].

A sputter erosion path is a closed circle or elongated circle (“racetrack”) on a flat surface that forms over several uses. The mechanism of how the electron moves to the anode (substrate) with respect to the magnetic field is shown in Figure 1.12b. One disadvantage of the planar magnetron configuration is that the plasma is not uniform over the target surface. Therefore, the deposition pattern is dependent on the position of the substrate with respect to the target. This means that various types of fixturing must be used to establish position equivalency for the substrate(s) [33].

The main advantage of using cylindrical magnetron sputtering process over planar magnetron sputtering process is the effective target utilization for deposition process because uniform erosion takes place on the target surface. The cylindrical post cathode source allows deposition on the inside of a cylinder or cylindrical fixture (Figure 1.12c). It is useful for coating inside hollow shapes such as a rod or wire as a target to coat uniformly inside a pipe or tube. The hollow cylindrical cathode is useful for coating three-dimensional parts since the flux comes from all directions (Figure 1.12d). A substrate, such as a fiber, can be passed up the axis of the cylinder and become uniformly coated. The hollow cylinder has the added advantage that the material that is not deposited on the part is deposited on the target and re-sputtered, giving good target material utilization [35].

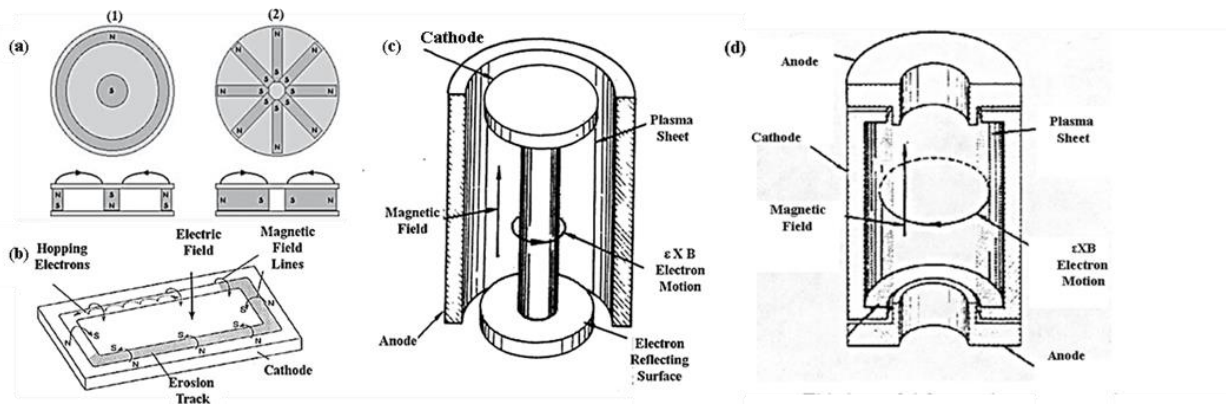


**Figure 1.12 (a) Schematic representations of two types of planar magnetron magnet arrangements setup used in sputtering process (b) Typical representation of movement of electrons in planar magnetron setup with respect to both electric and magnetic field (c) General view of cylindrical post cathode magnetron sputtering process with applied magnetic fields and electric field (d) Hollow cylindrical cathode [35]**

### 1.3.3 The Effects of the Energy of the Depositing Species on Deposit Properties

Sputtered atoms and reflected neutrals have relatively high kinetic energy, and the growing film is continuously bombarded by these energetic species. This leads to a range of effects, including re-sputtering of

deposited material, compaction, enhanced mobility, incorporation, implantation and formation of defects like nucleation sites. The effects of increasing ion energy are seen in Figure 1.13.

In ensuring coating uniformity, the behaviour of the sputtered species plays a crucial role. As the deposit flux travels from the target to the substrate surface, due to the mobility of the sputtering gas ions, it gets scattered causing various arrival angles at the substrate. This is an advantageous situation when complex shapes are used but in case a flat surface is to be coated, it is an undesired fact. Nevertheless, even in the case of coating complex shapes the scale of the features to be coated should be taken into consideration. Uniform coating can only take place for features significantly larger than the mean free path of the sputtered species in the gas [33,34].

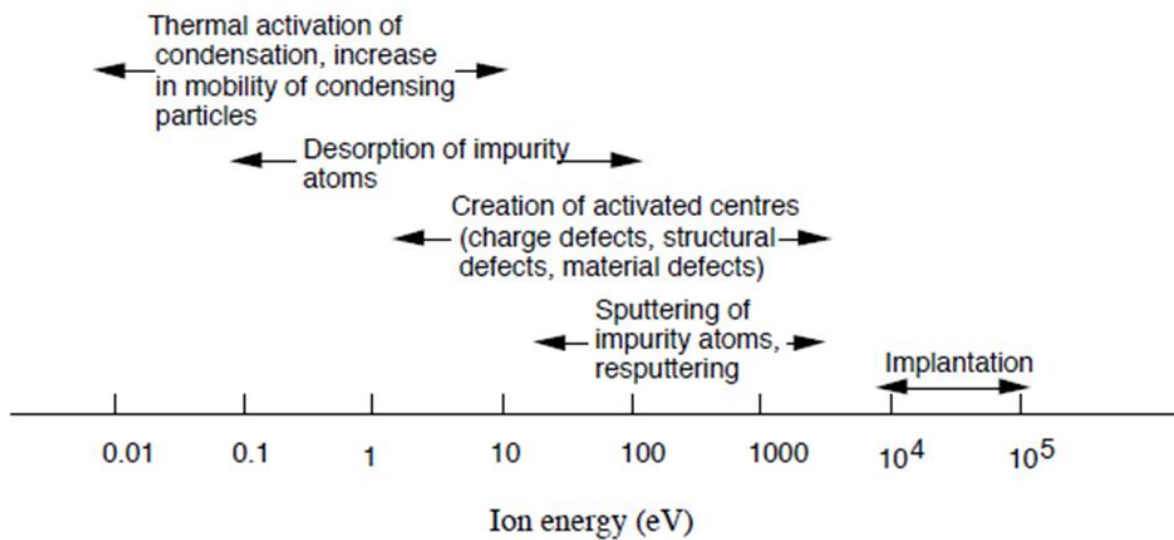


Figure 1.13 Effects that can be seen with respect to changing ion energy in sputtering processes [34]

### 1.3.4 Sputter Deposition Targets

#### Target Configurations

Targets can be in many forms. They must have the appropriate geometry for the fixture or for the substrate. Commonly, planar targets, hollow cylindrical targets, post cathodes and targets are used [33].

Being able to make variations in target configurations makes this technique more flexible. For example, sputtering from two or more independent targets is possible. The deposition rate from each target can be precisely controlled in order to have a complete control over the alloy composition. Sputtering from an alloyed single target is an option as well. Using a composite sputtering target with different areas fabricated from different components of the alloy is also possible. The relative target area controls the composition. Sputtering from compound targets can also be carried out, however it requires RF sputtering if it is insulating [33].

## **Target specifications**

Sputtering target specifications include [33]:

- Dimensions and tolerances including flatness and surface finish of any sealing surface.
- Purity, along with allowable and non-allowable impurities to specific levels.
- Grain size, particularly of compound materials.
- Inclusions and second phase material.
- Density.
- Outgassing rate.
- Fabrication method (e.g. required, preferred, not allowed).
- Residual stress.

## **Target surface changes with use**

The target's surface tends to change with use. This changing geometry can affect the deposition rate, vapor flux distribution and other deposition parameters. In case the surface morphology of the target material changes, roughening can occur on the surface and sputtering rates might decrease due to changes in the flux pattern. Roughening can happen because of the different crystallographic planes in a polycrystalline target or sputter texturing of the surface (i.e. cone formation and surface recrystallization) [33].

## **Target pre-conditioning**

Layers of oxides or contaminants might cover the target surface. In order to exclude them from the deposition process they can be pre-sputtered before the coating starts. A shutter can be placed between the target and the substrate during this process. Moving the substrate out of the deposition region while the pre-sputtering is performed is also an option [33].

## **Target power supplies**

Variations in power supply combinations are also a facility that sputter deposition provides as pointed out in section 1.3.2.

### **1.3.5 Process Control in Sputter Deposition**

Sputter deposition has several parameters (i.e. sputtering rate, system geometry, substrate temperature, etc) that must be controlled in order to have a reproducible process and product. Some of these parameters are related to:

## **Sputtering system**

A good working sputtering system should have good vacuum system. The vacuum capability is quite important as it provides a reproducible plasma environment to be constituted. Throttling the high vacuum valve or using variable orifice conductance valve, which can be servo or controlled by a pressure gauge, enables controlling the pumping speed [33].

## **Pressure**

Sputter-deposited films grow quite dependently on the gas pressure. The pressure determines the energization of the particles in the system. Therefore, precise monitoring of the pressure in the sputtering chamber is very important [33].

## **Target power and voltage**

Reproducible sputtering parameters mean monitoring the target power ( $\text{watts/cm}^2$ ) and voltage. Direct current power supplies should have an arc suppression circuit that reacts to a current surge or voltage drop. Arc suppression can be accomplished by shutting off the power or by providing a positive potential to counteract the arc [33].

## **Plasma properties**

Mostly, no monitoring is applied for the plasma properties of ion and electron density. Reproducible plasma can be obtained by utilizing constant geometry, gas pressure and target voltage and power [33].

## **Substrate temperature**

It is important to use either thermocouples embedded in or attached directly to the substrate material or infrared pyrometers to determine the temperature, if the surface emissivity and absorption in the optics is constant. It is also important in the manipulation of the process taking substrate temperature into consideration [33].

# **1.4 Electrodeposition of Bismuth and Bismuth Based Compounds**

## **1.4.1 Electrodeposition of Bismuth**

Bismuth is the 83<sup>rd</sup> numbered element of the periodic table. It has a whitish silver colour with an iridescent oxide layer on its surface that causes different wavelengths of light to interfere upon reflection. As a result, it exhibits many shades of colours. The liquid phase of bismuth is denser than its solid phase. This is a rare case that can only be seen in water, gallium, germanium and silicon besides bismuth. The fact that it expands over solidification makes it a favourable choice for typesetting alloys in filling printed moulds. Along with graphite,

it is one of the most diamagnetic materials known. It gets repelled by the magnetic field which makes it convenient for applications in magnetic levitation trains [24].

Bismuth shares the same layered structure as As and Sb, which are its neighbours in the periodic table. It has a rhombohedral lattice and it belongs to R-3m space group [36].

Its one electron band structure shows an indirect negative band gap between the valence band maximum and the conduction band minimum. Because of the small valence and conduction band overlap, bismuth is a semimetal with a reduced number of charge carriers at Fermi energy [37].

Electrodeposition of semi-metal bismuth has been an attractive topic due to its unique physicochemical properties. It has become a choice for a wide range of applications in different areas, including magnetoresistance [38,39], thermoelectricity [40], superhydrophobic surfaces [41], or electroanalysis [27,42, 43].

Electrodeposition of bismuth in a wide range of morphologies has been reported: Sparse particles varying from polyhedral (mostly hexagonal particles [44]) to rods, dendrites or fern-like structures, and dense or particulated films [45] have been obtained by manipulating deposition parameters. Aqueous nitrate solutions have been used in order to obtain continuous films, micro-nano/dendrites and hexagons. Jian et al. showed deposition of dendrite-like bismuth on Pt, Al and indium tin oxide (ITO) substrates from a diluted nitric acid bath with  $\text{Bi}(\text{NO}_3)_3 \cdot 5\text{H}_2\text{O}$  and ethylenediaminetetraacetic acid (EDTA) [46]. Glassy carbon electrodes (GCE) were used as the substrate in the studies of Yang and Hu in which bismuth reduction from a bath with 1 M  $\text{HNO}_3$  + 5–20 mM  $\text{Bi}(\text{NO}_3)_3 \cdot 5\text{H}_2\text{O}$  was implemented between -100 mV to -300 mV vs. Ag|AgCl (3 M KCl) for deposition times between 10 s and 350 s [47]. In the work done by Sandnes et al. the results of Bi electrodeposition from bath with different concentrations of  $\text{Bi}(\text{NO}_3)_3 \cdot 5\text{H}_2\text{O}$  dissolved in 1 M  $\text{HNO}_3$  were reported [48]. Au electrode is claimed to be the most suitable electrode to investigate the reduction of bismuth ions from acidic nitrate solutions due to the fact that nitrate electroreduction proceeds slowly and it is marginally detectable [49]. Bulk deposition of Bi was observed ca. -0.5 V vs. SSE (i.e., at -0.05 V vs. Ag|AgCl) upon pre-depositing Bi by underpotential deposition (UPD). The resulting morphologically compact, relatively thick films (1.0–15  $\mu\text{m}$  thick) were characterized morphologically and structurally. Hydrogen coevolution was encountered in a two-step deposition series applied between -0.5 V for 200 s followed by -0.8 V for 1000 s in which fern-shaped dendrites were obtained. In the second step, hydrogen formation accompanied the growth of bismuth [49].

Applications like heterogeneous catalysis, gas storage and sensing require a larger surface-to-volume ratio compared to continuous films which make the synthesis of submicron structures and nanostructures focus of many research studies. Low populated surfaces that consist of small nuclei/crystals relatively far away from each other are reported in the literature [44]. However, in particular cases, densely populated electrodes with a large density of, though not yet coalesced, particles can be utilized in interesting applications.

It is important to introduce different complexing agents in the bismuth electrodeposition baths in order to investigate its influence on bismuth growth. Deposition of Bi from citric acid, EDTA, and polyethylene glycol (PEG) baths has been studied [45,46] whereas the function of gluconate-containing acidic baths has been so far ignored.

#### **1.4.2 Electrodeposition of Bismuth (III) Oxide**

Due to its fluorite type crystal structure and its high ratio of oxygen vacancies, bismuth oxide is known as the best oxygen ionic conductor [50] which can be both p and n type [51,52]. It may exist in four crystalline structures:  $\alpha$ ,  $\beta$ ,  $\gamma$  and  $\delta$ . Each crystalline structure displays different electrical behaviour. Monoclinic  $\alpha$ - $\text{Bi}_2\text{O}_3$  is stable below 727 °C whereas tetragonal  $\beta$ -and body-centered cubic  $\gamma$ -phases can be achieved by cooling down from high temperature. The face-centered cubic  $\delta$ -phase shows stability between 727 °C and 825 °C, which is the melting point of bismuth oxide. Unlike the other phases of  $\text{Bi}_2\text{O}_3$ , all of which exhibit low electrical conductivity,  $\delta$  phase displays very high ionic conductivity [50].  $\delta$ - $\text{Bi}_2\text{O}_3$  has the highest oxygen ionic conductivity dominating the widely used yttria-stabilized zirconia (YSZ), which is usually used as the electrolyte in solid oxide fuel cell (SOFC) [53]. Most studies related to  $\text{Bi}_2\text{O}_3$  synthesis have been carried out by electroanalytical oxidation [51, 53,54].

Because  $\delta$ - $\text{Bi}_2\text{O}_3$  is only thermally stable between 727 °C and 825 °C, many research studies have been implemented to increase the domain of stability of this phase by making partial substitutions with rare earth elements [55]. However, this approach causes a decrease in electrical conductivity of the material. Stabilization of  $\delta$ -phase at room temperature was achieved by chemical vapour deposition [56]. To have bismuth oxide on SOFC applications, obtaining the  $\delta$  phase at low temperature is quite important. Switzer et al. [55] and Bohannan et al. [57] electrodeposited  $\delta$ - $\text{Bi}_2\text{O}_3$  at 65 °C from an alkaline bath with a pH of 14. Despite being a phase thermodynamically stable above 727 °C, the  $\text{Bi}_2\text{O}_3$  film was epitaxially deposited onto Au (110) substrate. In spite of the large lattice mismatch between the  $\text{Bi}_2\text{O}_3$  and the substrate, the fact that  $\text{Bi}_2\text{O}_3$  rotated 90° over the substrate provided the formation of the high temperature face-centered cubic phase at a low temperature. In this study the authors demonstrated that the  $\delta$  phase of  $\text{Bi}_2\text{O}_3$  could be stabilized at room temperature by electrochemical deposition. Additionally, Helfen et al. showed that by applying subsequent heat treatment upon electrodeposition the phase could be kept stable up to 340 °C [58]. In turn, electrodeposited  $\text{Bi}_2\text{O}_3$  thin films were used as electrochemical supercapacitors by Gujar et. al [59] successfully.

Studying the electrodeposition of  $\delta$ - $\text{Bi}_2\text{O}_3$  is significant since its miniaturization is essential for their use in energy production devices.



### 1.4.3 Electrodeposition of Bismuth Vanadate

In order to find solutions for the energy challenge, it is a very attractive approach to harvest energy directly from the sunlight by photosynthesis. Several attempts are devoted to find convenient materials and systems that can use solar energy to produce chemical fuels. For the reduction of water to H<sub>2</sub> or CO<sub>2</sub> to carbon-based molecules, one of the most feasible options is the construction of a photoelectrochemical cell [60]. N-type BiVO<sub>4</sub> has attracted much attention as a significant photoanode to be used in photoelectrochemical cells due to being capable of absorbing a substantial portion of the visible spectrum with a bandgap energy about 2.4 eV. Besides, it has a favorable conduction band edge position quite near the H<sub>2</sub> evolution potential [61].

So far, spin coating has been most typically used in order to prepare BiVO<sub>4</sub> electrodes by metal organic decomposition [62]. Hydrothermal synthesis [63] and vacuum deposition methods such as ballistic deposition (BD) and reactive ballistic deposition (RBD) [64] were implemented as well.

Electrochemical synthesis is another simple solution-based method recently explored for the synthesis of BiVO<sub>4</sub>. Seabold and Choi [65] prepared BiVO<sub>4</sub> by electrodeposition and subsequent heat treatment to be used in photoelectrochemical water splitting. The bath used had a pH of 4.7. The as-prepared films were subjected to heat treatment at 500 °C. As a result, BiVO<sub>4</sub> formation was obtained along with V<sub>2</sub>O<sub>5</sub>, which was later selectively dissolved in 1 M KOH. The resulting BiVO<sub>4</sub> photoanodes displayed considerable photocurrent for the photo-oxidation of sulfite. Seabold's bath was also used by Zhang and Chen to have BiVO<sub>4</sub> electrodeposited onto fluorine doped tin oxide (FTO) substrates previously coated by atomic layer deposition (ALD) method to construct a 3D FTO/TiO<sub>2</sub>/BiVO<sub>4</sub> composite inverse opals photoanode for photoelectrochemical hydrogen production [66].

W doped BiVO<sub>4</sub> synthesis by electrodeposition and subsequent heat treatment was studied by Cho et al. [67]. The authors observed that a more enhanced photoactivity performance could be obtained if the BiVO<sub>4</sub> structure was doped with W. The work carried out by Myung et al. [52] constitutes the first electrochemical synthesis approach toward BiVO<sub>4</sub>. A series of experiments based on the principle of having pre-electrodeposited Bi films stripped to produce Bi<sup>3+</sup> ions to either react with the VO<sub>4</sub><sup>3-</sup> ions (formed by hydrolysis of the bath components with VO<sup>3-</sup> anions) to make BiVO<sub>4</sub> or with the hydroxyl ions to make Bi<sub>2</sub>O<sub>3</sub> were carried out. The reaction products were deposited onto Pt substrates. It was observed that only BiVO<sub>4</sub> formation was encountered when the applied potential limit was kept at 0.5 V (vs. Ag|AgCl) whereas the formation of Bi<sub>2</sub>O<sub>3</sub> increased when the potential approached to 1.0 V (vs. Ag|AgCl). Only Bi<sub>2</sub>O<sub>3</sub> formation was obtained for the samples deposited at values above 1.0 V (vs. Ag|AgCl). Thus, the composite Bi<sub>2</sub>O<sub>3</sub>/BiVO<sub>4</sub> structures achieved from the depositions implemented between 0.5 V to 1.0 V (vs. Ag/AgCl), could arise as an interesting alternative to BiVO<sub>4</sub>/V<sub>2</sub>O<sub>5</sub> and BiVO<sub>4</sub>/WO<sub>3</sub> [52]. The enhanced photocatalytic properties of Bi<sub>2</sub>O<sub>3</sub>/BiVO<sub>4</sub> system were emphasized by Guan et al. [68] for core-shell Bi<sub>2</sub>O<sub>3</sub>/BiVO<sub>4</sub> microspheres.

#### **1.4.4 Electrodeposition of Bismuth Ferrite**

Multiferroic materials have come into focus of many researchers due to their interesting properties which unite ferromagnetism and ferroelectricity. This coupling of ferroelectric and magnetic properties allows the control of magnetism through electric fields or the other way around. This provides more opportunities in the design and manipulation of spintronic and memory devices in an energy efficient way [69,70]. Considerable energy loss is encountered due to Joule heating effect in typical spintronic and memory devices as they are fundamentally controlled by electric currents. Therefore, overall power consumption could be significantly decreased by partial substitution of electric current by electric fields as can be done in voltage-driven magnetic actuation [71,72].

$\text{BiFeO}_3$  is one of the few intrinsic multiferroic materials with a rhombohedral (R3c) structure. It belongs to the group of perovskites which are materials with  $\text{ABO}_3$  formula. In multiferroic perovskites, the origin of polarization mostly emerges from the A site. In turn, magnetization is provided by the B site. The ferroelectricity in  $\text{BiFeO}_3$  forms due to the lone pair ( $s^2$  orbital) of  $\text{Bi}^{3+}$  and magnetization is due to magnetic moments of  $\text{Fe}^{3+}$  [69,70]. It has a Curie temperature of 827 °C and a Néel temperature of 370 °C, which makes it one of the few multiferroics at room temperature [69-71].  $\text{BiFeO}_3$  is a suitable candidate to be used in applications related to photovoltaics, spintronics, sensors and data storage. Owing to its ferroelectricity, it is an appropriate sustainable lead-free substitute for PZT [28].

From the thermodynamical viewpoint,  $\text{BiFeO}_3$  is a metastable compound formed between the stable  $\text{Bi}_{25}\text{FeO}_{39}$  (sillenite) and  $\text{Bi}_2\text{Fe}_4\text{O}_9$  (mullite) compounds in the phase equilibrium diagram of  $\text{Bi}_2\text{O}_3$  and  $\text{Fe}_2\text{O}_3$ . It forms between 447 °C and 767 °C [69]. Consequently, there is a high tendency for formation of these two stable phases along with  $\text{BiFeO}_3$ . The qualities of the end product depend on several factors such as purity of the precursors, preparation method, chemical additives or heat treatment conditions [73-76]. The properties of  $\text{BiFeO}_3$  are quite sensitive to oxygen stoichiometry and tiny deviations might lead to undesired properties such as current leakages [77]. Furthermore, even though the material is antiferromagnetic, it often exhibits soft magnetism due to spin canting [78]. As spin canting reinforces, due to the partial suppression of the spiral spin structure, a larger saturation magnetisation is achieved [79]; hence, developing novel magnetoelectric materials with nanoscale architectures is of high interest [80,81]. Accordingly,  $\text{BiFeO}_3$ , in addition to its potential application in spintronics and data storage, it is a convenient alternative to be used in photovoltaic devices and related applications [82-85].

Various methods such as solid state reaction [75], sol-gel [86,87], pulsed laser deposition [88,89], sputtering [90], solution combustion [91], aqueous solution-gel route [92], microemulsion method [93], Pechini method [94] and microwave hydrothermal synthesis [95] have been implemented to obtain this material. It was seen that when synthesized by the conventional solid state reaction method, side products such as  $\text{Bi}_{25}\text{FeO}_{39}$  (sillenite) and  $\text{Bi}_2\text{Fe}_4\text{O}_9$  (mullite) formed along with  $\text{BiFeO}_3$ . To remove them, leaching with diluted  $\text{HNO}_3$

was applied [75]. In the studies carried out related to solid state reaction thermochemistry of BiFeO<sub>3</sub> synthesis, it was stated that Bi<sub>2</sub>O<sub>3</sub> and Fe<sub>2</sub>O<sub>3</sub> system is quite sensitive to impurity presence [73-75]. Moreover, the precipitation of other ternary oxides at grain boundaries is highly encountered. Among the previous studies to suppress these secondary phases, doping with La and Ce in solution combustion synthesis of BiFeO<sub>3</sub> [96] or doping with Sm in solid state synthesis of BiFeO<sub>3</sub> take place [97]. Sol-gel method was seen to provide weaker ferromagnetism and enhancement in ferroelectric properties of BiFeO<sub>3</sub> compared to solid state reaction method in the research carried out by Sharma et al. as it is a more suitable approach since the starting materials are mixed at molecular level, which renders improved properties upon further heat treatment [98].

Besides, studies by Chu's group [86] and Wu's group [87] report the fabrication of pure bismuth ferrite by sol-gel method. In addition to sol-gel technique, thin films of pure bismuth ferrite with enhanced ferroelectric properties were synthesized by Ramesh and his group [88] by pulsed laser deposition. In the epitaxial films grown, a large spontaneous polarization value of approximately 60  $\mu\text{C}/\text{cm}^2$  and an enhanced thickness-dependent magnetism was achieved as fine tuning of oxygen pressure was applied in pulsed laser deposition [88,89].

Among the techniques mentioned above, methods like solid state reaction or sol-gel typically result in powdery BiFeO<sub>3</sub> formation, which hinders the eventual integration of the material into devices since further immobilization on a substrate is required. Smooth coatings with compositional homogeneity are provided by pulsed laser deposition (PLD). However this is a costly method that requires high vacuum conditions. Furthermore, it does not allow the growth of films of several micrometers in thickness. In addition, deposition onto curved substrates or porosity control is not possible by PLD. Up to now, despite being a cost-effective method that functions at ambient pressure and provides micrometer thick films, electrodeposition studies on bismuth ferrite have been very scarce and the results have not been fully satisfactory as they lack a clear and unambiguous structural characterisation [99-101]. Besides, in these previous works, emphasis was laid on the electrochemical performance of the materials (i.e., BiFeO<sub>3</sub> nanoflake and thin film electrodes were applied in supercapacitor applications). The magnetic properties were overlooked.

## **1.5 Sputter Deposited Shape Memory Alloys**

### **1.5.1 Shape Memory Alloys**

Shape memory alloys are particular systems which display reversible behaviour when they are exposed to a mechanical load or temperature change. The reason of this behaviour lies in martensitic phase transformation where there is a cooperative motion of a large number of atoms, each being displaced only by a small distance from its neighbours. Martensitic phase transformation is a reversible transformation which has advantageous effects, such as a capacity to cycle a component between two different macroscopic shapes by cycling the temperature [102].

Shape memory alloys exist in two different phases and three different crystal structures including twinned martensite, detwinned martensite and austenite (Figure 1.14) [103,104]. The phase that is stable at high temperature is the austenite whereas the one stable at low temperature is the martensite.

The phase transformations that take place are explained as follows [105]:

- The austenitic phase start temperature,  $A_s$ , which is the temperature where the martensitic phase begins to transform into the parent (austenitic) phase.
- The austenitic phase end temperature,  $A_f$ , which is the temperature where the martensitic phase has completely transformed into the austenitic phase.
- The martensite start temperature,  $M_s$ , which is the temperature where the austenitic phase starts to transform into the martensite phase.
- The martensite end temperature,  $M_f$ , which is the temperature where the austenitic phase has completely transformed into the martensite phase.
- The highest temperature at which martensite can no longer be stress induced is called  $M_d$ , and the shape memory alloy is permanently deformed like any ordinary metallic material above this temperature.

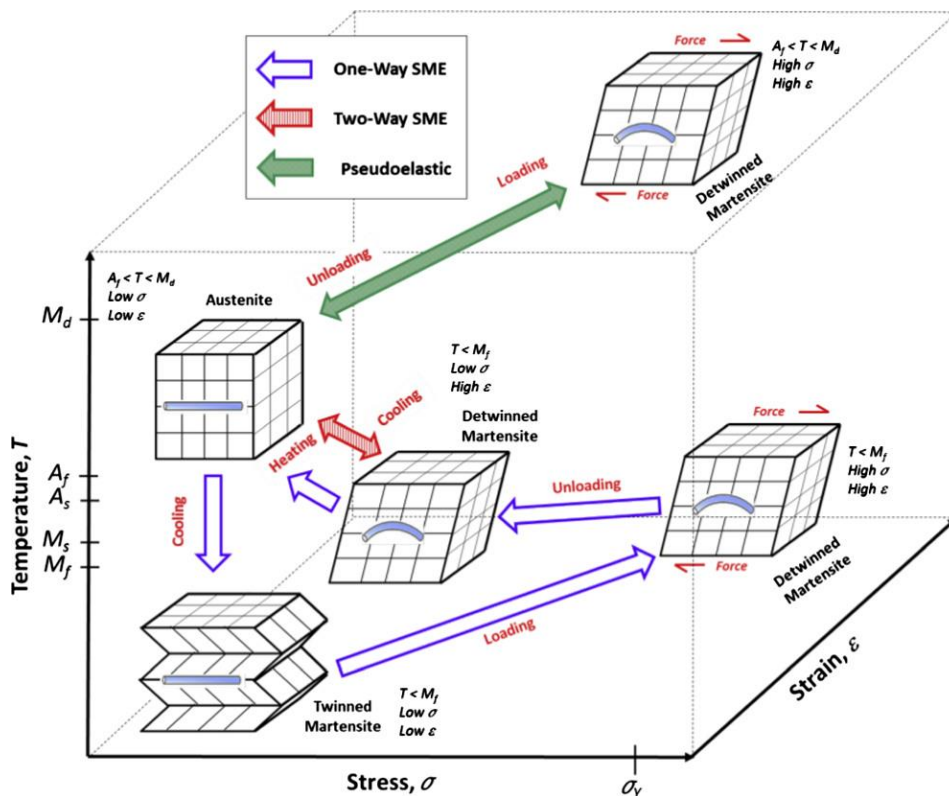
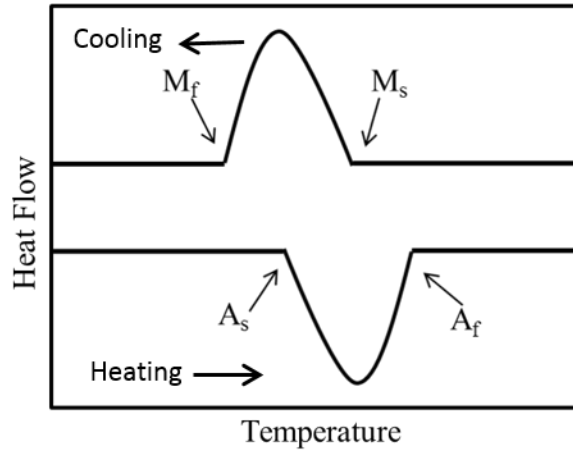


Figure 1.14 Shape memory alloy phases and crystal structures [105]

A transformation from martensite to austenite is observed for a shape memory alloy when it is heated above the austenitic start temperature,  $A_s$ . A schematic of a DSC curve for a shape memory alloy showing the phase transformations as peaks and the start and finish of martensite ( $M_s$ ,  $M_f$ ) and austenite ( $A_s$ ,  $A_f$ ) phases during heating and cooling is shown in Figure 1.15.



**Figure 1.15** A typical DSC curve for a shape memory alloy showing the phase transformations as peaks and the start and finish of martensite ( $M_s$ ,  $M_f$ ) and austenite ( $A_s$ ,  $A_f$ ) phases [106]

When the component is given a thermo-mechanical treatment, which involves holding at a high temperature (usually well above  $A_f$ ), followed by cooling (to below  $M_f$ ), while mechanically constrained to have a particular shape, stress relaxation occurs during the holding period and then, during cooling (in the constrained shape), the austenite-martensite transformation takes place in such a way as to minimise the overall shape change. When a portion of the austenitic lattice shears to form the martensitic phase, there are usually several alternative directions in which it can do this – forming what are often termed different “variants” – so it is possible for groups of variants to be formed which, taken together, have a very similar shape to the original parent material. This training predisposes the component to adopt the shape concerned when the phase transformation occurs, since this minimises the associated elastic strain energy. Once a component has been “trained” in this way, then, after it has been deformed in an arbitrary way, it can recover its “trained” shape just by reheating it to above its  $A_f$  temperature [102].

Shape memory alloys can exhibit superelasticity (when they are mechanically stressed in the austenite phase) or shape memory effect (which is a thermally induced effect that can be divided in one-way or two-way shape memory effect).

Alloys that exhibit one-way shape memory effect retain a deformed state after the removal of an external force, and then recover its original shape upon heating.

Alloys that display two-way shape memory effect are capable of remembering their shape both at high and low temperatures.

### Superelasticity:

A shape memory alloy displays superelasticity if it gains its original shape after applying mechanical loading at temperatures between  $A_f$  and  $M_d$  without any thermal activation [102].

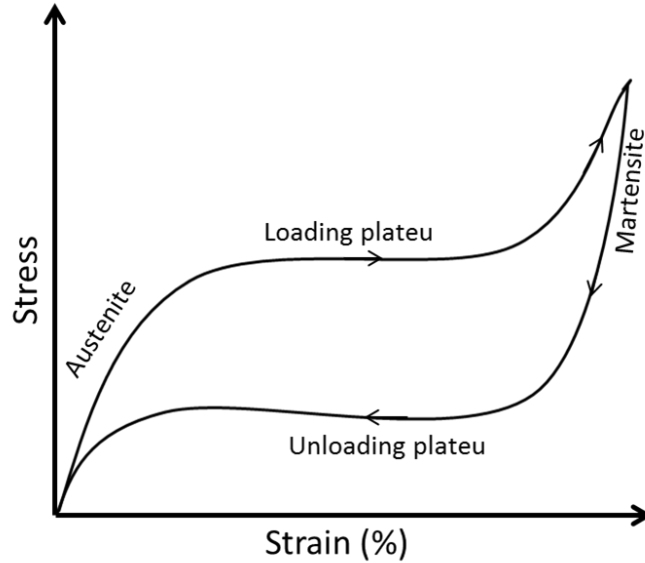


**Figure 1.16 Schematic stress-strain diagram of a superelastic shape memory alloy [107]**

A representative stress-strain diagram of a superelastic shape memory alloy is seen in Figure 1.16. It occurs without any change in temperature. When a mechanical strain is imposed, this can stimulate the transformation of austenite to martensite, sometimes termed “stress-induced martensite”. The associated shear of local regions accommodates the imposed macroscopic shape change, while the lower strain energy component ensures that the overall free energy is now lower than it would be if the austenitic phase were still predominant [102].

As the martensite to austenite transformation does not take place at the same stress levels during unloading as the forward transformation did during loading, stress-strain plots of superelastic alloys exhibit hysteresis. Small hysteresis loops provide better performance for rapid actuation applications such as MEMS and larger hysteresis loops are better to retain the predefined shape within a large temperature range such as deployable structures and pipe joining [106,107].

Shape memory alloys have a wide application range. For instance, superelastic stents are used to hold open arteries as they are capable of being compressed while being inserted to the body and, when set free, spring back to their larger shape. The shape memory effect is also used in actuators to generate motion with respect to temperature change [102]. Currently, there are over a hundred patents on shape memory alloys in automotive, aerospace, robotic and biomedical applications categorized against relevant commercial domains and rated according to design objectives of relevance to these domains [105,108,109].

## **1.5.2 Sputtered Shape Memory Thin Films**

Shape memory thin films are commonly produced as either stand-alone films or onto micromachined materials [105,110,111]. The high power to weight ratio, large achievable strain, and low driving voltage of SMA films and thin wires suggest a potential for superior microactuators [112]. The fast-growing field of MEMS has made shape memory thin films primary microactuator choices as they have a higher actuation force and displacement at lower frequencies [105,110,111]. So far, Ni–Ti is the most dominant product in commercial applications [107]. However, each shape memory thin film material brings its own advantage to technology.

### **1.5.2.1 Ni–Ti and Ni–Ti–X (with X = Cu, Pd, Hf) Thin Films**

Sputtering is the most commonly executed method to obtain Ni–Ti based shape memory alloys. Other methods such as PLD, ion beam deposition, arc plasma ion plating, plasma spray and flash evaporation were also reported but, along with problems such as non-uniformity in film thickness and composition, low deposition rate, or non-batch processing, they turn out to be noncompatible with MEMS fabrication process. Transformation temperatures, shape memory behaviors and superelasticity of the sputtered Ni–Ti films show sensitivity against metallurgical factors, sputtering conditions, and the application conditions [111].

Proper control of Ni/Ti ratio is crucial. Thus, the reported fundamental problems related to Ni–Ti sputtering are: (i) the yields of titanium and nickel at a sputtering power density are different, (ii) geometrical composition uniformity over substrate and along cross-section thickness of the coating is challenging and (iii) wear, erosion and roughening of targets during sputtering typically occurs [105,107,110-113]. Methods such as adding titanium plates [114,115] on Ni–Ti target, co-sputtering of Ni–Ti, or using two separate single element (Ni and Ti) targets [112,113] have been implemented in order to cope with the aforementioned problems. Variations in target temperature also affect the composition: sputtering the heated Ni–Ti target can limit the loss of Ti, thus improving the uniformity of film properties [105,116,117].

### **Ni–Ti: Post-annealed Films**

Ni–Ti films can be either deposited at room temperature or high temperatures based on the processing conditions. Ni–Ti films sputtered at room temperature are amorphous and require annealing as a post-treatment, mostly at temperatures higher than 450 °C. Yet, the martensite transformation and superelasticity of Ni–Ti films are sensitive to martensite transformation and superelasticity of Ni–Ti films is sensitive to post-annealing and/or aging temperature and duration [118,119]. For this reason, the lowest possible reaction temperatures must be applied [120].

### **Ni–Ti: In-situ Crystallization**

In-situ crystallization is achieved in films deposited around 400 °C. For the crystalline phase to form, the films can be deposited at relatively high temperatures (400-500 °C) at the beginning of the sputtering process and then, at lower temperatures (300 °C) to support the crystalline growth during the entire sputter deposition. It is also possible to deposit the films at a lower temperature, around 300 °C, to introduce partial crystallization and then apply annealing as a post-treatment at a rather higher temperature (i.e. 500 °C) to enhance further crystallization [112].

### **Ni–Ti–X Systems (with X = Cu, Pd, Hf)**

In case a large recovery strain is required for a microactuator, a smaller hysteresis, by approximately 30 K than that of Ni–Ti, is required [107]. Cu addition into Ni–Ti is effective in obtaining a smaller transformation temperature hysteresis without decreasing transformation temperatures. TiNiCu thin films with Cu-contents varying from 0 to 18 at% were investigated [121-124].

Additions of Pd and Hf as a third element have resulted in an increase of transformation temperatures [125-127]. Hf addition increases transformation temperature hysteresis while increasing the transformation temperatures. On the contrary, Pd addition decreases the transformation temperature hysteresis but increases transformation temperatures [126,127].

#### **1.5.2.2 Cu–Al–Ni Thin Films**

The Cu–Al–Ni system has come into focus in many research studies since it is a cost-effective solution that could replace the conventionally used Ni–Ti [23,128]. Moreover, Cu based shape memory alloys exhibit a narrower hysteresis in the transformation-retransformation process [129]. Cu–Al–Ni shape memory alloys can be used in applications up to 473 K and they have a large non-linear superelastic strain of approximately 18 % [130]. The good machinability, ease in forming process, high thermal stability, rapid heating and cooling rate, smaller hysteresis and a high Young's modulus are major advantages of the system [131-133]. Cu–Al–Ni systems shape memory alloys typically consist of Cu–Al14–Ni4 (wt%) composition. A gradual change in the room temperature phase from martensite to austenite is observed in these alloys due to slight changes in the Al and Ni concentration [134].

In the studies carried out by Minemura et al. [135], Cu–Al14–Ni4 (wt%) films, grown between 373 K and 573 K on Al substrates, exhibited bending when they were immersed in liquid nitrogen and turned back to original shape at room temperature. On the other hand, for the films grown below 373 K no shape memory effect was observed and martensite phase was present along with the austenite phase.



The group of Morán et al. [136] implemented the deposition of a sacrificial Fe layer onto c-cut  $\text{Al}_2\text{O}_3$  substrate before depositing Cu–Al–Ni thin films in order to prevent any kind of interaction between the Cu–Al–Ni film and the substrate during film growth. A mixed target with Cu–21Al–10Ni (wt%) composition was used for the experiments and the Fe layer was selectively etched to obtain free-standing films. When the films were exposed to liquid nitrogen, good recovery of their original shape was observed for the Cu–Al–Ni films grown between 533 K and 563 K.

In the studies carried out by Torres et al. [137] quenching in iced water upon heat treating the films at 1123 K was applied for Cu–Al–Ni films grown at room temperature from a mixed target with composition Cu–27.35Al–5.45Ni (at%). It was also observed that quenching is required in Cu–Al–Ni alloys to retain the austenitic phase at room temperature [137,138]. Textured Cu–Al–Ni thin films with micrometric grains were obtained. The films exhibited a microstructure with submicrometric grains. The change in resistance with respect to temperature was measured and it was seen that as the grain sizes became smaller the martensitic transformation took place with a larger hysteresis loop [137].

The study of the shape memory behaviour of Cu–Al–Ni thin films is of prime importance in order to constitute a place for it in the commercial market.

### **1.5.2.3 Magnetic Shape Memory alloys: Fe–Pd and Ni–Mn–Ga**

The underlying mechanism of magnetic shape memory or magnetostrictive alloys relies on the coupling of structural and ferromagnetic domains, which implies that any reorientation of magnetic domains caused by a magnetic field is associated with a reorientation of structural domains and vice versa. The option to control large strains by stress and magnetic field allows the development of novel Magnetic Shape Memory (MSM) actuators with large strains and short response times without the need of contacting the specimen [139]. Fe–Pd and Ni–Mn–Ga systems are sustainable candidates to replace the widely used rare-earth metal based  $\text{Tb}_x\text{Dy}_{1-x}\text{Fe}_2$  ( $x \sim 0.3$ ), Terfenol-D (see section 1.1.4), as they are even capable to exhibit larger strains [18,140].

#### **Fe–Pd Thin Films**

Sugimura et al. [141] studied the sputtered Fe–Pd films, with Pd content varying between 26 and 30 at. %, deposited from separate Fe and Pd targets. The as-deposited films displayed a highly supersaturated solid solution of Pd in Fe. On the other hand, if post-quenching was applied after holding the sample at 900 °C, the formation of the high temperature austenite phase at low temperature was possible.

Furuya's group [142] investigated Fe–Pd30 (at%) alloy thin films prepared on quartz substrates by RF magnetron sputtering. The structural properties of the films deposited at lower power values were improved by

post solution treatment at high temperature whereas the ones deposited at higher power values exhibited highly preferentially oriented structure without any need for further treatment. Magnetic properties of the thin films along the film surface were comparable with those of melt spun ribbons and they exhibited pronounced hysteresis loop.

Cialone et al. [18] worked on 80 nm thick  $\text{Fe}_{67}\text{Pd}_{33}$  (at%) films deposited by RF sputtering onto Si/SiO<sub>2</sub> substrates from a composite target prepared by adding Pd tiles on top of a Fe target. The single phase  $\text{Fe}_{67}\text{Pd}_{33}$  (at%) films were subjected to annealing as a novel post-deposition approach and multicomponent layered systems were obtained. Regarding the modeled temperature profile recorded across the film thickness, formation of a temperature gradient within the film showing a decrease from the film surface towards the substrate interface was observed. The fact that Fe atoms tended to diffuse towards the surface, due to presence of the temperature, caused enrichment of Fe in the upper section of the film. Modelled temperature profile across the film thickness showed that the film surface had a higher temperature as compared to the interface with the substrate. Iron atoms diffuse accordingly to the temperature gradient, thus making the lower section of the film rich in palladium by creating a variation of elemental composition across the thin film [18].

### **Ni–Mn–Ga Thin Films**

Polycrystalline Ni–Mn–Ga thin films have been deposited onto various substrates such as Si(100), molybdenum, glass, NaCl and Al<sub>2</sub>O<sub>3</sub>. In these studies submicron martensitic Ni<sub>2</sub>MnGa was obtained and all of them were capable of displaying structural and magnetic anisotropy [143].

Various studies related to epitaxial growth of Ni–Mn–Ga system have been carried out. Ranzieri et al. [144] investigated the dependence of epitaxial austenite formation to film thickness in a series of samples prepared with 10 to 100 nm thicknesses on MgO (100) substrates. Due to the low lattice mismatch between the substrate and the austenitic phase, films with lower thicknesses displayed proper epitaxial growth whereas formation of martensite along with austenite was encountered in the films thicker than 40 nm as the films started to evolve to their bulk state because of the weakening in the epitaxial constraints [144]. For the 100 nm thick films studied by Elmer's group [145] the tendency of epitaxial growth between Al<sub>2</sub>O<sub>3</sub> (11-20) and MgO (100) was compared and it was seen that martensitic phase was more stable in the films grown on Al<sub>2</sub>O<sub>3</sub> than the ones grown on MgO.

## **1.6 Size Effects of Shape Memory Alloys**

It is crucial to understand size scale dependence of martensitic transformations in order to have shape memory alloys utilized in suitable applications for devices in micro/nanoplatfroms. Basically, the grain size ( $d$ ) and the sample size ( $D$ ) are the two size scales that affect the martensitic transformation of a shape memory material [146].

A decrease in the volume or in one of the dimensions of a material, or a decrease in grain size and phase composition might result in a 'transition smearing' which can be explained as a decrease in the critical transition temperature and an increase of the temperature range over which the transition occurs. Materials have limiting grain sizes and film thicknesses below of which martensitic transformation do not take place [147].

In previous studies in literature it was shown for Cu–Al–Ni, Cu–Al–Mn, Cu–Al–Be, Cu–Zn–Al, Cu–Zn–Sn and Ti–Ni–Zr sheets or wires with a thickness or diameter  $D$  on the millimetre-scale that  $\sigma_{M_s}$ , the martensitic transformation stress value, increases with decreasing the  $d/D$  ratio. For these cases, the decrease in  $M_s$  and the increase in  $\sigma_{M_s}$  reveal that martensite formation is suppressed at smaller relative grain sizes, which points out an increasing grain constraint that acts against the nucleation of martensite from the austenite matrix [146].

For Cu–Al–Ni system it was shown that obtaining a  $d/D$  ratio close to 1 improved the superelastic recovery in a way that is superior to Ni–Ti. San Juan et al. [148,149] showed that Cu–Al–Ni pillars with  $D = 1.7 \mu\text{m}$  and  $0.9 \mu\text{m}$  displayed complete superelastic recovery better than that of Ni–Ti [150-151]. Furthermore, both  $\sigma_{M_s}$  and  $\Delta E/E$ , with  $\Delta E$  being the area within the hysteresis loop and  $E$  the maximum strain energy, in Cu–Al–Ni submicron pillars were found to be higher than in bulk single crystals with the same composition. The increase in  $\sigma_{M_s}$  was claimed to arise from the lack of martensite nucleation sites, while the increase in  $\Delta E/E$  was attributed to the release of elastic transformation strains at the pillar surface and the resulting delay in the reverse transformation [149].

For Ni–Ti system, suppression of martensitic transformation below 50 nm of critical size in nanocrystalline Ni–Ti thin films was shown by Waitz et al. [152,153]. Fu et al. [154] showed that sputtered Ni–Ti films with a thickness below 100 nm displayed no martensitic transformation under increasing grain constraints. Additionally Wan and Komvopoulos [155] reported that electrical resistivity hysteresis loops of sputtered Ni–Ti films went smaller as the thickness of the films decreased from 300 nm to 50 nm and finally disappeared below 50 nm.

In the study carried out by Dunand and Müllner [156] on size effects in Ni–Mn–Ga shape memory system, it was concluded that magnetic field induced strains were very large for monocrystalline Ni–Mn–Ga (up to 10%) whereas they were near zero (<0.01%) in fine-grained polycrystals due to incompatibilities during twinning of neighbouring grains and the resulting internal geometrical constraints.

## References

- [1] Magee, L., Scerri, A., James, P., Thom, J. A., Padgham, L., Hickmott, S., Cahill, F. Reframing Social Sustainability Reporting: Towards an Engaged Approach. *Environment, Development and Sustainability*, 15 (2013), 225–243.
- [2] Leung, H. Relationship between Environmental, Social and Economic Elements of Development (I), Basis of Sustainable Development, <http://eyesonhkbu.hkbu.edu.hk/index.php/en-GB/wetalk/55-english-categories/wetalk/community-and-environment/1167-putting-passion-to-work-environmental-sciences-part-ii-subtle-relationship-between-environmental-social-and-economic-elements-of-development-1>
- [3] An Introduction to MEMS (Microelectromechanical Systems). Prime Faraday Partnership. Wolfson School of Mechanical and Manufacturing Engineering. University of Loughborough. 2002.
- [4] MEMSnet, What is MEMS Technology, <http://www.memsnet.org/mems/>
- [5] Royal Society of Chemistry, Sol–Gel Definition, <http://www.rsc.org/publishing/journals/prospect/ontology.asp?id=CMO:0001313&MSID=B916355G>
- [6] Sahu, N., Parija, B., Panigrahi, S. Fundamental Understanding and Modelling of Spin Coating Process: A Review. *Indian Journal of Physics*, 83 (2009), 493–502.
- [7] Faustini, M., Drisko, G., Boissiere, C., Grosso D. Liquid Deposition Approaches to Self–Assembled Periodic Nanomasks. *Scripta Materialia*, 74 (2014), 13–18.
- [8] Pierson, H. O. *Handbook of Chemical Vapor Deposition, Principles, Technology and Applications*. William Andrew Publishing. New York. 1999.
- [9] Kaariainen, T., Cameron, D., Kaariainen, M.L., Sherman, A. *Atomic Layer Deposition: Principles, Characteristics and Nanotechnology Applications (Chapter in Atomic Layer Deposition (ALD), Second Edition)*. Scrivener Publishing. Beverly. 2013.
- [10] Groves, J. F., Wadley, H. N. G., Ritenour, A.P., Hass, D. D., Ratnaparkhi, P. L. *Electron Beam Directed Vapor Deposition. Proceedings of the Electron Beam Melting and Refining State of the Art*. Bakish Materials Corporation. Englewood. 1997.
- [11] Seshan, K. *Handbook of Thin Film Processes and Techniques, Principles, Methods, Equipment and Applications (Chapter in Deposition Technologies and Application: Introduction and Overview, Second Edition)*. Noyes Publications/William Andrew Publishing. Norwich. 2002.
- [12] Schneider C.W., Lippert T. *Laser Ablation and Thin Film Deposition. (Chapter in Laser Processing of Materials)*. Springer. Berlin. 2010.
- [13] Blunt, J., Balchin, N.C. *Thermal Spraying (Chapter in Health and Safety in Welding and Allied Processes, Fifth Edition)*. CRC Press. Boca Raton. 2002.
- [14] Geissler, M., Xia, Y. Patterning: Principles and Some New Developments. *Advanced Materials*, 16 (2004), 1249–1269.
- [15] Navinšek, B., Panjan, P., Milošev, I. PVD Coatings as an Environmentally Clean Alternative to Electroplating and Electroless Processes. *Surface and Coatings Technology*, 116–119 (1999), 476–487.
- [16] European Commission. *Critical Raw Materials for the EU, Report of the Ad-hoc Working Group on Defining Critical Raw Materials*. 2010. [https://ec.europa.eu/growth/tools-databases/eip-raw-materials/en/system/files/ged/79%20report-b\\_en.pdf](https://ec.europa.eu/growth/tools-databases/eip-raw-materials/en/system/files/ged/79%20report-b_en.pdf)
- [17] Coey, J. M. D. New Permanent Magnets; Manganese Compounds. *Journal of Physical Condensed Materials*, 26 (2014), 064211.
- [18] Cialone, M., Celegato, F., Coisson, M., Barrera, G., Fiore, G., Shvab, R., Klemet, U., Rizzi, P., Tiberto, P. Tailoring Magnetic Properties of Multicomponent Layered Structure via Current Annealing in FePd Thin Films. *Scientific Reports*, 7 (2017), 1–8.

- [19] Thyssen, J. P. Nickel and Cobalt Allergy Before and After Nickel Regulation – Evaluation of a Public Health Intervention. *Contact Dermatitis*, 65 (2011), 1–68.
- [20] EU – Amendment to Nickel Release Standard Published – EN 1811:2011 + A1:2015
- [21] Candidate List of Substances of Very High Concern for Authorisation, <https://echa.europa.eu/candidate-list-table/-/dislist/details/0b0236e1807daa34>
- [22] Beale, C. The Price of This Element Has Surged in 2017. <https://www.weforum.org/agenda/2017/12/cobalt-surged-2017-lithium-ion-batteries-electric-vehicles/>
- [23] Alaneme, K. K., Okotete, E. A. Reconciling Viability and Cost–Effective Shape Memory Alloy Options: A Review of Copper and Iron Based Shape Memory Metallic Systems. *Engineering Science and Technology. An International Journal*, 19 (2016), 1582–1592.
- [24] Mohan, R. Green Bismuth. *Nature Chemistry*, 2 (2010), 336.
- [25] DiPalma, J. R. Bismuth Toxicity, Often Mild, Can Result in Severe Poisonings. *Emergency Medicine News*, 23 (2001), 16.
- [26] Hopper, K.D., King, S.H., Lobell, M.E., TenHave, T.R., Weaver, J.S. The Breast: In–Plane X–Ray Protection during Diagnostic Thoracic CT–Shielding with Bismuth Radioprotective Garments. *Radiology*, 205 (1997), 353–358.
- [27] Wang, J. Stripping Analysis at Bismuth Electrodes: A Review. *Electroanalysis*, 17 (2005), 1341–1346.
- [28] Restriction of Hazardous Substances in Electrical and Electronic Equipment. Directive 2011/65/EU. [http://ec.europa.eu/environment/waste/rohs\\_eee/legis\\_en.htm](http://ec.europa.eu/environment/waste/rohs_eee/legis_en.htm)
- [29] Klochko, K. U. S. Geological Survey, Mineral Commodity Summaries, Bismuth. 2018. <http://minerals.usgs.gov/minerals/pubs/commodity/bismuth/index.html>
- [30] Zangl, S., Hendel, M., Blepp, M., Liu, R., Gensch, C. O., Deubzer, O. Adaptation to Scientific and Technical Progress of Annex II Directive 2000/53/EC. *Oko–Institut e.V.* 2008. [http://elv.exemptions.oeko.info/fileadmin/user\\_upload/Final\\_Report/Corr\\_Final\\_report\\_ELV\\_RoHS\\_28\\_07\\_2010.pdf](http://elv.exemptions.oeko.info/fileadmin/user_upload/Final_Report/Corr_Final_report_ELV_RoHS_28_07_2010.pdf)
- [31] La Fontaine, A., Keast, V. J. Compositional Distributions in Classical and Lead–Free Brasses. *Materials Characterization*, 57 (2006), 424–429.
- [32] Varea, A. PhD Thesis. Multifunctional Electrodeposited Nanocrystalline Cu–Ni Films. *Universitat Autònoma de Barcelona*. 2012.
- [33] Mattox, D. *Handbook of Physical Vapor Deposition Processing (Chapter in Physical Sputtering and Sputter Deposition, Second Edition)* William Andrew Publishing. Burlington. 2010.
- [34] Barber, Z. *Thin Film Notes*. University of Cambridge. 2017.
- [35] Santhosh, P. M.Sc. Thesis. Preparation and Characterization of Titanium Based Coatings by Direct Current (DC) Magnetron. *Tampere University of Technology*. 2015.
- [36] Cucka, P., Barrett, C. S. The Crystal Structure of Bi and of Solid Solutions of Pb, Sn, Sb and Te in Bi. *Acta Crystallographica*, 15 (1962), 865–872.
- [37] Craco, L., Leoni, S. Magnetoresistance in the Spin–Orbit Kondo State of Elemental Bismuth. *Scientific Reports*, 5 (2015), 1–9.
- [38] Liu, K., Chien, C. L., Searson, P. C., Yu-Zhang, K., Liu, K. Giant Positive Magnetoresistance in Arrays of Semi–Metallic Bismuth Nanowires. *IEEE Transactions on Magnetism*, 34 (1998), 1093–1095.
- [39] Yang, F. Y. Large Magnetoresistance of Electrodeposited Single–Crystal Bismuth Thin Films. *Science*, 284 (1999), 1335–1337.
- [40] Agapescu, C., Cojocaru, A., Cotarta, A., Visan, T. Electrodeposition of Bismuth, Tellurium, and Bismuth Telluride Thin Films from Choline Chloride–Oxalic Acid Ionic Liquid. *Journal of Applied Electrochemistry*, 43 (2013), 309–321.

- [41] Su, C., Lu, Z., Zhao, H., Yang, H., Chen, R. Photoinduced Switchable Wettability of Bismuth Coating with Hierarchical Dendritic Structure between Superhydrophobicity and Superhydrophilicity. *Applied Surface Science*, 353 (2015), 735–743.
- [42] Zhou, H., Hou, H., Dai, L., Li, Y., Zhu, J., Wang, L. Preparation of Dendritic Bismuth Film Electrodes and Their Application for Detection of Trace Pb(II) and Cd(II). *Chinese Journal of Chemical Engineering*, 24 (2016), 410–414.
- [43] Ananthi, A., Kumar, S. S., Phani, K. L. Facile One-Step Direct Electrodeposition of Bismuth Nanowires on Glassy Carbon Electrode for Selective Determination of Folic Acid. *Electrochimica Acta*, 151 (2015), 584–590.
- [44] Som, T., Simo, A., Fenger, R., Troppenz, G. V., Bansen, R., Pfänder, N., Emmerling, F., Rappich, J., Boeck, T., Rademann, K. Bismuth Hexagons: Facile Mass Synthesis, Stability and Applications. *ChemPhysChem*, 13 (2012), 2162–2169.
- [45] Tsai, Y. D., Lien, C. H., Hu, C. C. Effects of Polyethylene Glycol and Gelatin on the Crystal Size, Morphology, and Sn<sup>2+</sup>-Sensing Ability of Bismuth Deposits. *Electrochimica Acta*, 56 (2011), 7615–7621.
- [46] Jiang, S., Huang, Y. H., Luo, F., Du, N., Yan, C. H. Synthesis of Bismuth with Various Morphologies by Electrodeposition. *Inorganic Chemistry Communications*, 6 (2003), 781–785.
- [47] Yang, M., Hu, Z. Electrodeposition of Bismuth onto Glassy Carbon Electrodes from Nitrate Solutions. *Journal of Electroanalytical Chemistry*, 583 (2005), 46–55.
- [48] Sandnes, E., Williams, M. E., Bertocci, U., Vaudin, M. D., Stafford, G. R. Electrodeposition of Bismuth from Nitric Acid Electrolyte. *Electrochimica Acta*, 52 (2007), 6221–6228.
- [49] Yang, M. Fern-Shaped Bismuth Dendrites Electrodeposited at Hydrogen Evolution Potentials. *Journal of Materials Chemistry*, 21 (2011), 3119.
- [50] Laurent, K., Wang, G. Y., Tusseau-Nenez, S., Leprince-Wang, Y. Structure and Conductivity Studies of Electrodeposited  $\delta$ -Bi<sub>2</sub>O<sub>3</sub>. *Solid State Ionics*, 178 (2008), 1735–1739.
- [51] Metikos-Hukovic, M. The Photoelectrochemical Properties of Anodic Bi<sub>2</sub>O<sub>3</sub> Films. *Electrochimica Acta*, 26 (1981), 989–1000.
- [52] Myung, N., Ham, S., Choi, S., Chae, Y., Kim, W. G., Jeon, Y. J., Paeng, K.J., Chanmanes, W., Tacconi, N.R., Rajeshwar, K. Tailoring Interfaces for Electrochemical Synthesis of Semiconductor Films: BiVO<sub>4</sub>, Bi<sub>2</sub>O<sub>3</sub> or Composites. *Journal of Physical Chemistry C*, 115 (2011), 7793–7800.
- [53] Williams, D. E., Wright, G. A. Nucleation and Growth of Anodic Oxide Films on Bismuth–II, *Electrochimica Acta*, 24 (1979), 1179–1187.
- [54] Castillo, L. M., Peter, L. M. J. Internal Photoemission at the Bi/Anodic Bi<sub>2</sub>O<sub>3</sub> Interface. *Journal of Electroanalytical Chemistry and International Electrochemistry*, 146 (1983), 377–384.
- [55] Switzer, J. A. Electrodeposited Ceramic Single Crystals. *Science*, 284 (1999), 293–296.
- [56] Takeyama, T., Takahashi, N., Nakamura, T., Itoh, S.  $\delta$ -Bi<sub>2</sub>O<sub>3</sub> Thin Films Deposited on Dense YSZ Substrates by CVD Method under Atmospheric Pressure for Intermediate Temperature SOFC Applications. *Surface and Coatings Technology*, 200 (2006), 4797–4801.
- [57] Bohannon, E. W., Jaynes, C. C., Shumsky, M. G., Barton, J. K., Switzer, J. A. Low-Temperature Electrodeposition of the High-Temperature Cubic Polymorph of Bismuth (III) Oxide. *Solid State Ionics*, 131 (2000), 97–107.
- [58] Helfen, A., Merkourakis, S., Wang, G., Walls, M., Roy, E., Yuzhang, K., Leprince-Wang, Y. Structure and Stability Studies of Electrodeposited  $\delta$ -Bi<sub>2</sub>O<sub>3</sub>. *Solid State Ionics*, 176 (2005), 629–633.
- [59] Gujar, T. P., Shinde, V. R., Lokhande, C. D., Han, S. H. Electrosynthesis of Bi<sub>2</sub>O<sub>3</sub> Thin Films and Their Use in Electrochemical Supercapacitors. *Journal of Power Sources*, 161 (2006), 1479–1485.
- [60] Park, Y., McDonald, K. J., Choi, K. S. Progress in Bismuth Vanadate Photoanodes for Use in Solar Water Oxidation. *Chemical Society Reviews*, 42 (2013), 2321–2337.

- [61] Kim, T. W., Choi, K.S. Nanoporous BiVO<sub>4</sub> Photoanodes with Dual-Layer Oxygen Evolution Catalysts for Solar Water Splitting. *Science*, 343 (2014), 990–994.
- [62] Abdi, F. F., Van De Krol, R. Nature and Light Dependence of Bulk Recombination in Co–Pi–Catalyzed BiVO<sub>4</sub> Photoanodes. *Journal of Physical Chemistry C*, 116 (2012), 9398–9404.
- [63] Wang, D., Li, R., Zhu, J., Shi, J., Han, J., Zong, X., Li, C. Photocatalytic Water Oxidation on BiVO<sub>4</sub> with the Electrocatalyst as an Oxidation Cocatalyst: Essential Relations between Electrocatalyst and Photocatalyst. *Journal of Physical Chemistry C*, 116 (2012), 5082–5089.
- [64] Berglund, S. P., Flaherty, D. W., Hahn, N. T., Bard, A. J., Mullins, C. B. Photoelectrochemical Oxidation of Water Using Nanostructured BiVO<sub>4</sub> Films. *Journal of Physical Chemistry C*, 115 (2011), 3794–3802.
- [65] Seabold, J. A., Choi, K. S. Efficient and Stable Photo-Oxidation of Water by a Bismuth Vanadate Photoanode Coupled with an Iron Oxyhydroxide Oxygen Evolution Catalyst. *Journal of the American Chemical Society*, 134 (2012), 2186–2192.
- [66] Zhang, H., Cheng, C. Three-Dimensional FTO/TiO<sub>2</sub>/BiVO<sub>4</sub> Composite Inverse Opals Photoanode with Excellent Photoelectrochemical Performance. *ACS Energy Letters*, 2 (2017), 813–821.
- [67] Cho, S. K., Park, H. S., Lee, H. C., Nam, K. M., Bard, A. J. Metal Doping of BiVO<sub>4</sub> by Composite Electrodeposition with Improved Photoelectrochemical Water Oxidation. *Journal of Physical Chemistry C*, 117 (2013), 23048–23056.
- [68] Guan, M. L., Ma, D. K., Hu, S. W., Chen, Y. J., Huang, S. M. From Hollow Olive–Shaped BiVO<sub>4</sub> to n–p Core–Shell BiVO<sub>4</sub>–Bi<sub>2</sub>O<sub>3</sub> Microspheres: Controlled Synthesis and Enhanced Visible–Light-Responsive Photocatalytic Properties. *Inorganic Chemistry*, 50 (2011), 800–805.
- [69] Izyumskaya, N., Alivov, Y., Morkoç, H. Oxides, Oxides, and More Oxides: High-κ Oxides, Ferroelectrics, Ferromagnetics, and Multiferroics. *Critical Reviews in Solid State and Materials Sciences*, 34 (2009), 89–179.
- [70] Catalan, G., Scott, J. F. Physics and Applications of Bismuth Ferrite. *Advanced Materials*, 21 (2009), 2463–2485.
- [71] Dieny, B., Sousa, R. C., Herault, J., Papusoi, C., Prenat, G., Ebels, U. Houssameddine D., Rodmacq B., Auffret S., Buda–Prejbeanu, L. D. Spin–Transfer Effect and Its Use in Spintronic Components. *International Journal of Nanotechnology*, 7 (2010), 591–614.
- [72] Hu, J. M., Li, Z., Chen, L. Q., Nan, C. W. High–Density Magnetoresistive Random Access Memory Operating at Ultralow Voltage at Room Temperature. *Nature Communications*, 2 (2011), 553–558.
- [73] Valant, M., Axelsson, A., Alford, N. Peculiarities of a Solid–State Synthesis of Multiferroic Polycrystalline BiFeO<sub>3</sub>. *Chemistry of Materials*, 19 (2007), 5431–5436.
- [74] Lindh, R., Kraemer, W. P., Kämper, M. On the Thermodynamic Stability of BiFeO<sub>3</sub>. *Journal of Physical Chemistry A*, 103 (1999), 8295–8302.
- [75] Achenbach, G. D., James, W. J., Gerson, R. Preparation of Single–Phase Polycrystalline BiFeO<sub>3</sub>, *Journal of American Ceramic Society*, 50 (1967), 437.
- [76] Liu, T., Xu, Y., Zhao, J. Low-Temperature Synthesis of BiFeO<sub>3</sub> via PVA Sol-Gel Route. *Journal of the American Ceramic Society*, 93 (2010), 3637–3641.
- [77] Yang, H., Wang, Y. Q., Wang, H., Jia, Q. X. Oxygen Concentration and Its Effect on the Leakage Current in BiFeO<sub>3</sub> Thin Films. *Applied Physics Letters*, 96 (2010), 94–97.
- [78] Ramazanoglu, M., Laver, M., Ratcliff, W., Watson, S. M., Chen, W. C., Jackson, A., Kothpalli, K., Lee, S., Cheong, S. W., Kiryukhin, V. Local Weak Ferromagnetism in Single–Crystalline Ferroelectric BiFeO<sub>3</sub>. *Physical Review Letters*, 107 (2011), 1–5.
- [79] Huang, F., Wang, Z., Lu, X., Zhang, J., Min, K., Lin, W., Ti, R., Xu, T., He, J., Chen, Y., Zhu, J. Peculiar Magnetism of BiFeO<sub>3</sub> Nanoparticles with Size Approaching the Period of the Spiral Spin Structure. *Scientific Reports*, 3 (2013), 1–7.

- [80] Bèa, H., Bibes, M., Petit, S., Kreisel, J. Barthèlèmy, A. Structural Distortion and Magnetism of BiFeO<sub>3</sub> Epitaxial Thin Films: A Raman Spectroscopy and Neutron Diffraction Study. *Philosophical Magazine Letters*, 87 (2007), 165–174.
- [81] Quickel, T. E., Schelhas, L. T., Farrell, R. A., Petkov, N., Le, V. H., Tolbert, S. H. Mesoporous Bismuth Ferrite with Amplified Magnetoelectric Coupling and Electric Field-Induced Ferrimagnetism. *Nature Communications*, 6 (2015), 1–7.
- [82] Park, T. J., Papaefthymiou, G. C., Viescas, A. J., Moodenbaugh, A. R., Wong, S. S. Size-Dependent Magnetic Properties of Single-Crystalline Multiferroic BiFeO<sub>3</sub> Nanoparticles. *Nano Letters*, 7 (2007), 766–772.
- [83] Yang, S. Y., Martin, L. W., Byrnes, S. J., Conry, T. E., Basu, S. R., Paran, D., Reichertz, L., Ihlefeld, J., Adamo, C., Melviller, A., Chu, Y.H., Yang, C.H., Musfeldt, J.L., Schlom, D.G., Ager III, J.W., Ramesh, R. Photovoltaic Effects in BiFeO<sub>3</sub>. *Applied Physics Letters*, 95 (2009), 1–4.
- [84] Yang, S. Y., Seidel, J., Byrnes, S. J., Shafer, P., Yang, C. H., Rossell, M. D., Yu, P., Chu, Y. H., Scott, J. F., Ager III, J. W., Martin, L. W., Ramesh, R. Above-Bandgap Voltages from Ferroelectric Photovoltaic Devices. *Nature Nanotechnology*, 5 (2010), 143–147.
- [85] Alexe, M., Hesse, D. Tip Enhanced Photovoltaic Effects in Bismuth Ferrite. *Nature Communications*, 2 (2011), 255–256.
- [86] Huang, D., Deng, H., Yang, P., Chu, J. Optical and Electrical Properties of Multiferroic Bismuth Ferrite Thin Films Fabricated by Sol-Gel Technique. *Materials Letters*, 64 (2010), 2233–2235.
- [87] Wang, X., Zhang, Y., Wu, Z. Magnetic and Optical Properties of Multiferroic Bismuth Ferrite Nanoparticles by Tartaric Acid-Assisted Sol-Gel Strategy. *Materials Letters*, 64 (2010), 486–488.
- [88] Wang, J., Neaton, J. B., Zheng, H., Nagarajan, V., Ogale, S. B., Liu, B, Viehland, D., Vaithyanathan, V., Schlom, D. G., Waghmare, U. V., Spaldin, N. A., Rabe, K. M., Wuttig, M., Ramesh, R. Epitaxial BiFeO<sub>3</sub> Multiferroic Thin Film Heterostructures. *Science*, 299 (2003), 1719–1722.
- [89] Jiang, K., Zhu, J. J., Wu, J. D., Sun, J., Hu, Z. G., Chu, J. H. Influences of Oxygen Pressure on Optical Properties and Interband Electronic Transitions in Multiferroic Bismuth Ferrite Nanocrystalline Films Grown by Pulsed Laser Deposition. *ACS Applied Materials and Interfaces*, 3 (2011), 4844–4852.
- [90] Plyaka, P. S., Tolmachev, G. N. Features of the Spectra of Optical Emission from High-Frequency Discharge Plasma during Bismuth Ferrite Sputtering. *Technical Physics Letters*, 36 (2010), 192–194.
- [91] Sarkar, K., Mukherjee, S., Mukherjee, S. Structural, Electrical and Magnetic Behaviour of Undoped and Nickel Doped Nanocrystalline Bismuth Ferrite by Solution Combustion Route, 9 (2015), 53–60.
- [92] Hardy, A., Gielis, S., Van den Rul, H., D’Haen, J., Van Bael, M. K., Mullens, J. Effects of Precursor Chemistry and Thermal Treatment Conditions on Obtaining Phase Pure Bismuth Ferrite from Aqueous Gel Precursors. *Journal of the European Ceramic Society*, 29 (2009), 3007–3013.
- [93] Das, N., Majumdar, R., Sen, A., Maiti, H. S. Nanosized Bismuth Ferrite Powder Prepared Through Sonochemical and Microemulsion Techniques. *Materials Letters*, 61 (2007), 2100–2104.
- [94] Ferri, E. A. V., Santos, I. A., Radovanovic, E., Bonzanini, R., Giroto, E. M. Chemical Characterization of BiFeO<sub>3</sub> Obtained by Pechini Method. *Journal of the Brazilian Chemical Society*, 19 (2008), 1153–1157.
- [95] Ponzoni, C., Cannio, M., Boccaccini, D. N., Bahl, C. R. H., Agersted, K., Leonelli, C. Ultrafast Microwave Hydrothermal Synthesis and Characterization of Bi<sub>1-x</sub>La<sub>x</sub>FeO<sub>3</sub> Micronized Particles. *Materials Chemistry and Physics*, 162 (2015), 69–75.
- [96] Priyadharsini, P., Pradeep, Salthymoorthy, B., Chandrasekaran, G., Enhanced Multiferroic Properties in La and Ce Co-Doped BiFeO<sub>3</sub> Nanoparticles. *Journal of Combustion Science and Technology*, 186 (2014), 297–312.
- [97] Nalwa, K. S., Garg, A., Upadhyaya, A. Effect of Samarium Doping on the Properties of Solid-State Synthesized Multiferroic Bismuth Ferrite. *Materials Letters*, 62 (2008), 878–881.



- [98] Sharma, S., Singh, V., Kotnala, R.K., Dwivedi, R.K. Comparative Studies of Pure BiFeO<sub>3</sub> Prepared by Sol–Gel versus Conventional Solid–State–Reaction Method. *Journal of Materials Science and Materials Electronics*, 25 (2014), 1915–1921.
- [99] Gujar, T. P., Shinde, V. R., Kulkarni, S. S., Pathan, H. M., Lokhande, C. D. Room Temperature Electrodeposition and Characterization of Bismuth Ferric Oxide (BFO) Thin Films from Aqueous Nitrate Bath. *Applied Surface Science*, 252 (2006), 3585–3590.
- [100] Jadhav, V. V., Zate, M. K., Liu, S., Naushad, M., Mane, R. S., Hui, K. N., Han, S. H. Mixed–phase Bismuth Ferrite Nanoflake Electrodes for Supercapacitor Application. *Applied Nanoscience*, 6 (2016), 511–519.
- [101] Gujar, T. P., Shinde, V. R., Lokhande, C. D., Mane, R. S., Han, S. H. Nonthermal Electrochemical Synthesis of Single–Phase, Porous, Nanostructured BiFeO<sub>3</sub> Platelets. *Electrochemical and Solid-State Letters*, 10 (2007), D1–D5.
- [102] Shape Memory Alloys, DoITPoMS, University of Cambridge, [https://www.doitpoms.ac.uk/tlplib/superelasticity/shape\\_memory1.php](https://www.doitpoms.ac.uk/tlplib/superelasticity/shape_memory1.php)
- [103] Sun, L., Huang, W. M. Nature of the Multistage Transformation in Shape Memory Alloys upon Heating. *Metal Science and Heat Treatment*, 51 (2009), 573–578.
- [104] Mihálcz, I. Fundamental Characteristics and Design Method for Nickel–Titanium Shape Memory Alloy. *Periodica Polytechnica Mechanical Engineering*, 45 (2001), 75–86.
- [105] Jani, J. M., Leary, M., Subic, A., Gibson, M. A. A Review of Shape Memory Alloy Research, Applications and Opportunities. *Materials and Design*, 56 (2014), 1078–1113.
- [106] Chen, H.R. Shape Memory Alloys: Manufacture, Properties and Applications (Chapter in Some Factors Affecting The Transformation Hysteresis in Shape Memory Alloys) Nova Science Publishers. New York. 2010.
- [107] Miyazaki, S., Fu, Y. Q., Huang, W. M. Thin Film Shape Memory Alloys: Fundamentals and Device Applications (Chapter in Overview of Sputter Deposited TiNi Based Thin Films) Cambridge University Press. Cambridge. 2009.
- [108] Fernandes, D. J., Peres, R. V., Mendes, A. M., Elias, C. N. Understanding the Shape–Memory Alloys Used in Orthodontics. *ISRN Dentistry*, 2011 (2011), 1–6.
- [109] Zahrai, S. M., Hamidia, M. J. Studying the Rehabilitation of Existing Structures Using Compound System of Cables and Shape Memory Alloys. *Proceedings of the ATC & SEI Conference on Improving the Seismic Performance of Existing Buildings and Other Structures*. California. 2009.
- [110] Winzek, B., Schmitz, S., Rumpf, H., Sterzl, T., Hassdorf, R., Thienhaus, S., Feyd., J., Moske, M., Quandt, E. Recent Developments in Shape Memory Thin Film Technology. *Materials Science and Engineering A*, 378 (2004), 40–46.
- [111] Fu, Y., Du, H., Huang, W., Zhang, S., Hu, M. TiNi–Based Thin Films in MEMS Applications: A Review. *Sensors and Actuators, A: Physical*, 112 (2004), 395–408.
- [112] Krulevitch, P., Lee, A. P., Ramsey, P. B., Trevino, J. C., Hamilton, J., Northrup, M. A. Thin Film Shape Memory Alloy Microactuators. *Journal of Microelectromechanical Systems*, 5 (1996), 270–282.
- [113] Shih, C.L., Lai, B.K., Kahn, H., Philips, S.M., Heuer, A.H. A Robust Co–Sputtering Fabrication Procedure for TiNi Shape–Memory Alloys for MEMS. *Journal of Microelectromechanical Systems*, 10 (2001), 69–79.
- [114] Miyazaki, S., Ishida, A. Martensitic Transformation and Shape Memory Behavior in Sputter–Deposited TiNi–Base Thin Films. *Materials Science and Engineering: A*, 273–275 (1999), 106–133.
- [115] Wolf, R. H. Heuer, A.H. TiNi (Shape Memory) Films on Silicon for MEMS applications. *Journal of Microelectromechanical Systems*, 4 (1995), 206–212.
- [116] Ho, K. K., Mohanchandra, K. P., Carman, G. P. Examination of the Sputtering Profile of NiTi under Target Heating Conditions. *Thin Solid Films*, 413 (2002), 1–7.

- [117] Ho, K. K., Carman, G. P. Sputter Deposition of NiTi Thin Film Shape Memory Alloy Using a Heated Target. *Thin Solid Films*, 370 (2000), 18–29.
- [118] Lehnert, T., Crevoiserat, S., Gotthardt, R. Transformation Properties and Microstructure of Sputter-Deposited Ni–Ti Shape Memory Alloy Thin Films. *Journal of Materials Science*, 37 (2002), 1523–1533.
- [119] Surbled, P., Clerc, C., Le, B., Ataka, M., Fujita, H. Effect of the Composition and Thermal Annealing on the Transformation Temperatures of Sputtered TiNi Shape Memory Alloy Thin Films. *Thin Solid Films*, 401 (2001), 52–59.
- [120] Isalgue, A., Torra, V., Seguin, J. L., Bendahan, M., Amigo, J., Esteve–Cano, V. Shape Memory NiTi Thin Films Deposited at Low Temperature. *Materials Science and Engineering: A*, 273–275 (1999), 717–721.
- [121] Miyazaki, S., Hashinaga, T., Ishida, A. Martensitic Transformations in Sputter-Deposited Ti–Ni–Cu Shape Memory Alloy Thin Films. *Thin Solid Films*, 281–282 (1996), 364–367.
- [122] Meng, X. L., Sato, M., Ishida, A. Structure of Martensite in Ti–Rich Ti–Ni–Cu Thin Films Annealed at Different Temperatures. *Acta Materialia*, 56 (2008), 3394–3402.
- [123] Meng, X. L., Sato, M., Ishida, A. Transmission Electron Microscopy Study of the Microstructure of B19 Martensite in Sputter-Deposited  $Ti_{50.2}Ni_{30}Cu_{19.8}$  Thin Films. *Scripta Materialia*, 59 (2008), 451–454.
- [124] Ishida, A., Sato, M., Ogawa, K. Microstructure and Shape Memory Behavior of Annealed Ti–36.8 at.% Ni–11.6 at.% Cu Thin Film. *Materials Science and Engineering A*, 481–482 (2008), 91–94.
- [125] Quandt, E., Halene, C., Holleck, H., Feit, K., Kohl, M., Schloßmacher, P., Skokank., A., Skrobanck, K. Sputter Deposition of TiNi, TiNiPd and TiPd Films Displaying the Two–Way Shape–Memory Effect. *Sensors and Actuators A: Physical*, 53 (1996), 434–439.
- [126] Baldwin, E., Thomas, B., Lee, J. W., Rabiei, A. Processing TiPdNi Base Thin–Film Shape Memory Alloys Using Ion Beam Assisted Deposition. *Surface and Coatings Technology*, 200 (2005), 2571–2579.
- [127] Lee, J. W., Thomas, B., Rabiei, A. Microstructural Study of Titanium–Palladium–Nickel Base Thin Film Shape Memory Alloys. *Thin Solid Films*, 500 (2006), 309–315.
- [128] Todorović, A., Rudolf R., Romčević, N., Đorđević, D., Milošević, N., Trifković, B., Veselinović, V., Čolić, M. Biocompatibility Evaluation of Cu–Al–Ni Shape Memory Alloys. *V–2* (2014), 228–238.
- [129] Lovey, F. C., Torra, V., Shape memory in Cu Based Alloys: Phenomenological Behavior at the Mesoscale Level and Interaction of Martensitic Transformation with Structural Defects in Cu–Zn–Al. *Progress in Materials Science*, 44 (1999), 189–289.
- [130] Suresh, N., Ramamurty, U. Aging Response and Its Effect on the Functional Properties of Cu–Al–Ni Shape Memory Alloys. *Journal of Alloys and Compounds*, 449 (2008), 113–118.
- [131] Araujo, V. E. A., Gastien, R., Zelaya, E., Beiroa, J. I., Corro, I., Sade, M., Lovey, F. C. Effects on the Martensitic Transformations and the Microstructure of CuAlNi Single Crystals after Ageing at 473 K. *Journal of Alloys and Compounds*, 641 (2015), 155–161.
- [132] Segui, C. Characterization of a Hot Rolled CuAlNiTi Shape Memory Alloy. *Materials Science and Engineering A*, 275 (1999), 625–629.
- [133] Akash. K., Mani Prabu, S. S., Shukla, A. K., Nath, T., Karthick, S., Palani, I. A. Investigations on the Life Cycle Behavior of Cu–Al–Ni/polyimide Shape Memory Alloy Bi–Morph at Varying Substrate Thickness and Actuation Conditions. *Sensors and Actuators, A: Physical*, 254 (2017), 28–35.
- [134] Recarte, V., Pérez-Sáez, R. B., San Juan, J., Bocanegra, E. H., Nó, M. L. Influence of Al and Ni Concentration on the Martensitic Transformation in Cu–Al–Ni Shape-Memory Alloys. *Metallurgical and Materials Transactions A*, 33 (2002), 2581–2591.
- [135] Minemura, T., Andoh, H., Kita, Y., Ikuta, I. Shape Memory Effect and Microstructures of Sputter-Deposited Cu–Al–Ni Films. *Journal of Materials Science Letters*, 4 (1985), 793–796.
- [136] Morán, M. J., Condó, A. M., Soldera, F., Sirena, M., Haberkorn, N. Martensitic Transformation in Freestanding and Supported Cu–Al–Ni Thin Films Obtained at Low Deposition Temperatures. *Materials*

Letters, 184 (2016), 177–180.

- [137] Torres, C., E., Condó, A. M., Haberkorn, N., Zelaya, E., Schryvers, D., Guimpel, J., Lovey, F. C. Structures in Textured Cu–Al–Ni Shape Memory Thin Films Grown by Sputtering. *Materials Characterization*, 96 (2014), 256–262.
- [138] Humbeeck, J. V., Chandrasekaran, M., Delaey, L. The Influence of Post Quench Aging in the Beta-Phase on the Transformation Characteristics and the Physical and Mechanical Properties of Martensite in a Cu–Al–Ni Shape Memory Alloy. *ISIJ International*, 29 (1989), 388–394.
- [139] Kohl, M., Schmitt, M., Backen, A., Schultz, L., Krevet, B., Fähler, S. Ni–Mn–Ga Shape Memory Nanoactuation. *Applied Physics Letters*, 104 (2014), 043111.
- [140] Inoue, S., Inoue, K., Koterazawa, K., Mizuuchi, K. Shape Memory Behavior of Fe–Pd Alloy Thin Films Prepared by DC Magnetron Sputtering. *Materials Science and Engineering: A*, 339 (2003), 29–34.
- [141] Sugimura, Y., Cohen-Karni, I., McCluskey, P., Vlassak, J. J. Stress Evolution in Sputter–Deposited Fe–Pd Shape–Memory Thin Films. *Journal of Materials Research*, 20 (2005), 2279–2287.
- [142] Wang, Z., Iijima, T., He, G., Oikawa, K., Wulff, L., Sanada, N., Furuya, Y. Preparation of Sputter–Deposited Fe–Pd Thin Films. *Materials Transaction, JIM*, 41 (2000), 1139–1141.
- [143] Chernenko, V. A., Besseghini, S., Hagler, M., Müllner, P., Ohtsuka, M., Stortiero, F. Properties of Sputter–Deposited Ni–Mn–Ga Thin Films. *Materials Science and Engineering A*, 481–482 (2008), 271–274.
- [144] Ranzieri, P., Fabbri, S., Nasi, L., Righi, L., Casoli, F., Chernenko, V. A., Villa, E., Albertini, F. Epitaxial Ni–Mn–Ga/MgO(100) Thin Films Ranging in Thickness from 10 to 100 nm. *Acta Materialia*, 61 (2013), 263–272.
- [145] Jakob, G., Eichhorn, T., Kallmayer, M., Elmers, H. J. Correlation of Electronic Structure and Martensitic Transition in Epitaxial Ni<sub>2</sub>MnGa films. *Physical Review B*, 76 (2007), 3–8.
- [146] Chen, Y., Schuh, C. A. Size Effects in Shape Memory Alloy Microwires. *Acta Materialia*, 59 (2011), 537–553.
- [147] Malygin, G. A. Nanoscopic Size Effects on Martensitic Transformations in Shape Memory Alloys. *Physics of the Solid State*, 50 (2008), 1538–1543.
- [148] San Juan, J., Nó, M. L., Schuh, C. A. Superelasticity and Shape Memory in Micro– and Nanometer–Scale Pillars. *Advanced Materials*, 20 (2008), 272–278.
- [149] San Juan, J., Nó, M. L., Schuh, C. A. Nanoscale Shape–Memory Alloys for Ultrahigh Mechanical Damping. *Nature Nanotechnology*, 4 (2009), 415–419.
- [150] Frick, C. P., Orso, S., Arzt, E. Loss of Pseudoelasticity in Nickel–Titanium Sub–Micron Compression Pillars. *Acta Materialia*, 55 (2007), 3845–3855.
- [151] Frick, C. P., Clark, B. G., Orso, S., Sonnweber–Ribic, P., Arzt, E. Orientation–Independent Pseudoelasticity in Small–Scale NiTi Compression Pillars. *Scripta Materialia*, 59 (2008), 7–10.
- [152] Waitz, T., Antretter, T., Fischer, F.D., Karnthaler, H.P. Size Effects on Martensitic Phase Transformations in Nanocrystalline NiTi Shape Memory Alloys. *Materials Science and Technology*, 24 (2008), 934–940.
- [153] Waitz, T., Tsuchiya, K., Antretter, T., Fischer, F. D. Phase Transformations of Nanocrystalline Martensitic Materials. *MRS Bulletin*, 34 (2009), 814–821.
- [154] Fu, Y. Q., Zhang, S., Wu, M. J., Huang, W. M., Du, H. J., Luo, J. K., Flewit, A. J., Milne, W. I. On the Lower Thickness Boundary of Sputtered TiNi Films for Shape Memory Application. *Thin Solid Films*, 515 (2006), 80–86.
- [155] Wan, D., Komvopoulos, K. Thickness Effect on Thermally Induced Phase Transformations in Sputtered Titanium–Nickel Shape–Memory Films. *Journal of Materials Research*, 20 (2005), 1606–1612.
- [156] Dunand, D. C., Müllner, P. Size Effects on Magnetic Actuation in Ni–Mn–Ga Shape Memory Alloys. *Advanced Materials*, 23 (2011), 216–232.

## 2. Experimental Methods

### 2.1 Film Synthesis

#### 2.1.1 Electrodeposited Films

Methrohm Autolab potentiostat/galvanostat AUTO50435 (Eco Chemie) belonging to the Gnm<sup>3</sup> group (Figure 2.1) was used for all electrodeposition experiments.

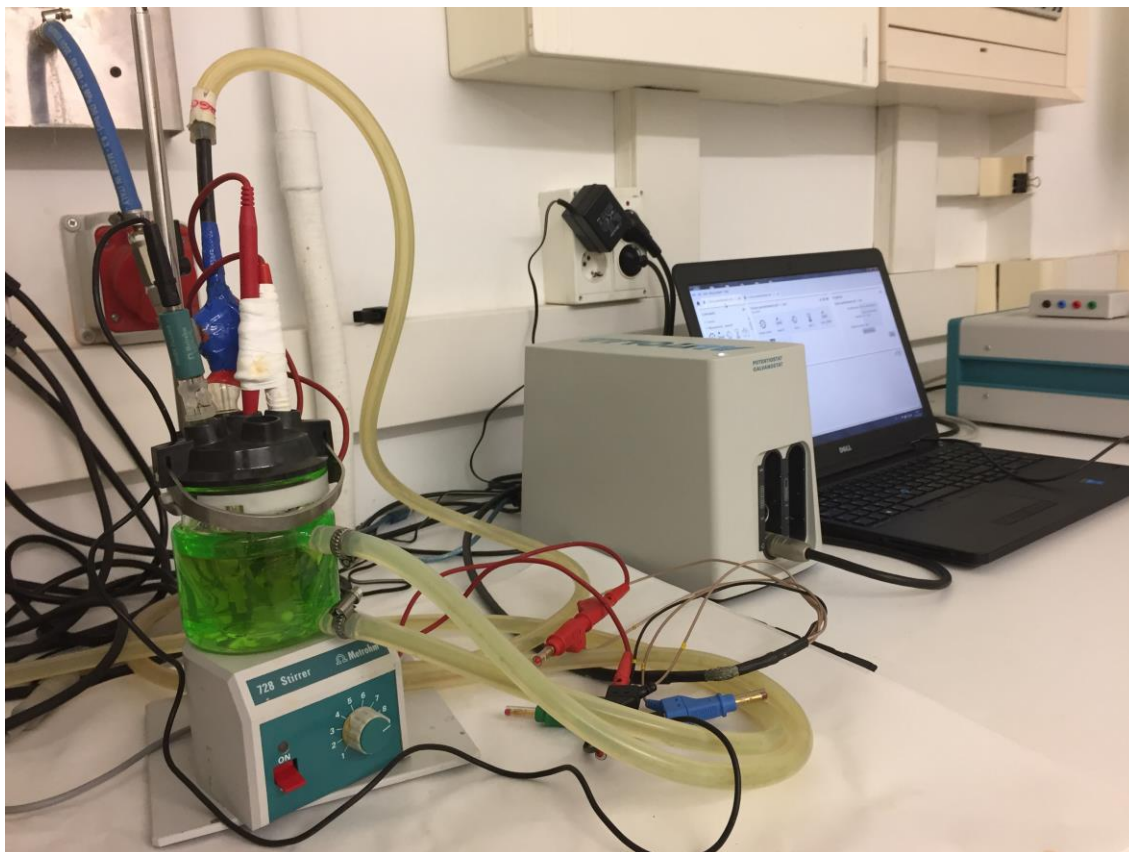


**Figure 2.1 Potentiostat/galvanostat used for electrodeposition purposes**

The electrolytic cell used was a conventional three electrode cell equipped with a thermostatzation jacket. As shown in Figure 2.2, a platinum wire served as the counter electrode. The reference electrode was Ag|AgCl ( $E^{\circ} = +0.210$  V versus standard hydrogen electrode (SHE)) filled with 3 M potassium chloride inner solution and 1 M sodium sulfate outer solution. The arrangement and distances between the electrodes were kept the same for each deposition process carried out.

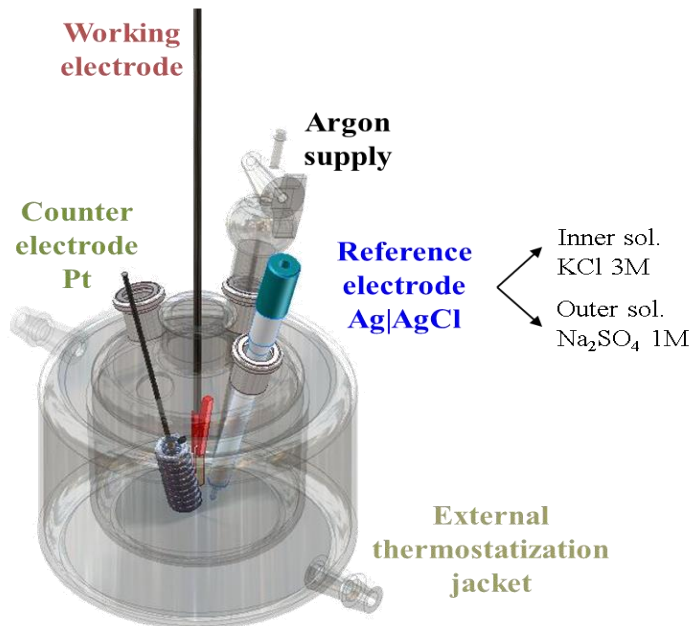


Figure 2.2 Sketch of the three electrode electrodeposition cell. Courtesy from Dr. S. Pané (ETHZ).

#### 2.1.1.1 Deposition Conditions

- **Bismuth**

Two different baths were used for bismuth electrodeposition. One of them consisted of 5 mM  $\text{Bi}(\text{NO}_3)_3 \cdot 5\text{H}_2\text{O}$  (Sigma-Aldrich, 98.0%) and 1.5 M  $\text{HNO}_3$  while the other one also included 0.05 M  $\text{NaC}_6\text{H}_{11}\text{O}_7$  (sodium gluconate), apart from the components formerly mentioned. Argon purging inside the electrolyte both before and during the electrodeposition was applied in order to avoid possible oxidation and favour mass transport.

- **Bismuth Ferrite**

Films with Bi:Fe  $\sim 1$  were prepared by potentiostatic electrodeposition from a bath containing 6 g/l  $\text{Bi}(\text{NO}_3)_3 \cdot 5\text{H}_2\text{O}$  (Sigma-Aldrich, 98.0%) and 10 g/l  $\text{Fe}(\text{NO}_3)_3 \cdot 9\text{H}_2\text{O}$  (Sigma-Aldrich, 99.95%) dissolved in dimethylformamide (DMF) (Sigma-Aldrich, 99.8%). Particularly, the depositions were performed under direct current conditions at 28 °C for 1800 s. 200 rpm stirring was used during deposition. Unless otherwise stated, the cathodic potential applied was  $-1.3$  V.

#### Preparation of Substrates

Bismuth films were electrodeposited onto various substrates in order to study the influence of substrate activity in the reduction process (Figure 2.3). As a metal substrate surface, gold was used. 90 nm of gold was sputtered onto silicon substrates, which were previously sputter coated with a 10 nm thick titanium layer to provide adhesion between the layers. In addition to gold substrates, indium tin oxide (ITO) and fluorine doped tin oxide (FTO) were employed as conductive oxide substrates [1] which were purchased from Sigma-Aldrich.

The substrates consisted of FTO and ITO layers that were coated onto glass surfaces. Glass/FTO and glass/ITO substrates used had resistivity values of 8  $\Omega$ /sq and 8–12  $\Omega$ /sq, respectively.

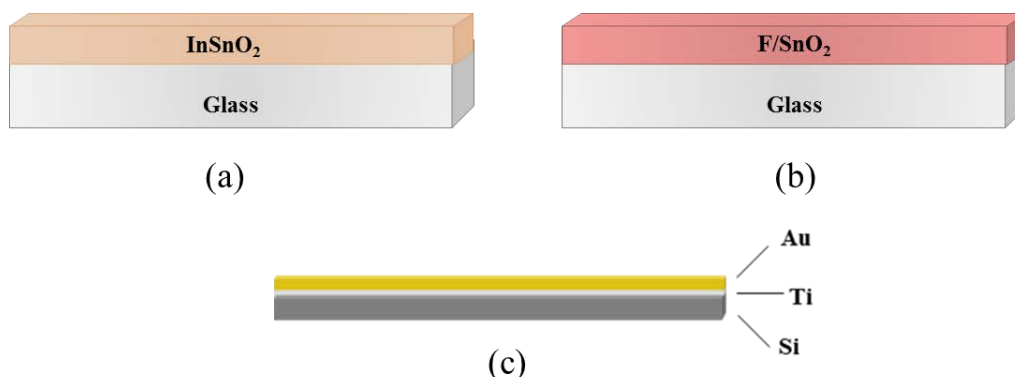


**Figure 2.3 Schemes of substrates used for bismuth electrodeposition (a) glass /ITO, (b) glass / FTO, and (c) Si/Ti/Au**

Bismuth ferrite films were electrodeposited onto Si/Ti/Cu (Figure 2.4) substrates, which were prepared following the same steps as for the preparation of Si/Ti/Au substrates.



**Figure 2.4 Scheme of Si/Ti/Cu substrate used for bismuth ferrite electrodeposition**

A pre-treatment of substrates before electrodeposition was performed as follows:

#### **For bismuth synthesis;**

Before electrodeposition, Si/Ti/Au substrates were cleaned with acetone, isopropanol and finally with Milli-Q water and dried with nitrogen, whereas glass/FTO and glass/ITO substrates were cleaned with isopropanol and dried. The working area was kept between 0.25 and 0.56 cm<sup>2</sup>. The electrodeposits were rinsed in Milli-Q water and hot dried after electrodeposition.

#### **For bismuth ferrite synthesis;**

Si/Ti/Cu substrates were cleaned with acetone, isopropanol and, as a last step, with Milli-Q water. Before being placed in the electrolyte, they were dried with nitrogen. The working area was kept between 0.25 and 0.27 cm<sup>2</sup>. After electrodeposition, the films were rinsed in Milli-Q water and hot dried.

### 2.1.1.2 Cyclic Voltammetry Studies

Cyclic voltammetry is an electroanalytical method typically used to examine the electrochemical behaviour of the bath species in a defined potential window. The x-axis represents the applied potential (E) while the y-axis is the resulting current (i) passed. An arrow is typically depicted to indicate the beginning and sweep direction of the first segment named “forward scan”. The cyclic voltammeteries were recorded in the same three-electrode cell configuration above described. The pre-treated substrates were inserted into the bath and polarized at a scan rate of 50 mV/s in order to determine reduction and oxidation potentials of the ions and deposited species, respectively, in the bath.

## 2.2 Sputter Deposited Films

Sputter deposition was used to synthesize Cu–Al–Ni shape memory thin films. Two approaches, one at room temperature and the other one at high temperature, were implemented to obtain the films.

### 2.2.1 Room Temperature Sputter Deposition

Ultra-high vacuum AJA International sputtering equipment was used for room temperature sputter deposition. The equipment is located at Universitat Autònoma de Barcelona, Gnm<sup>3</sup> group (Figure 2.5).

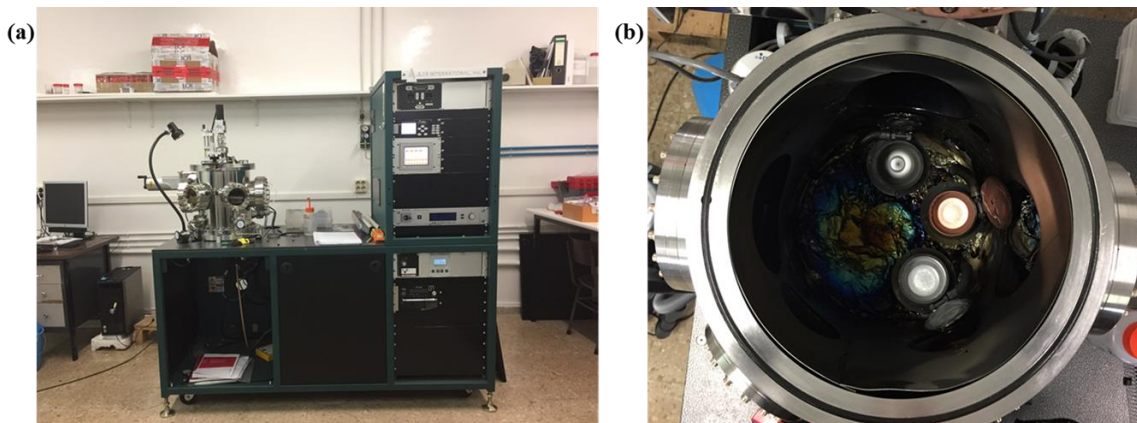


**Figure 2.5 (a) Sputter deposition equipment used for room temperature deposited samples (b) Target configuration inside the chamber**

Free-standing multi-layered films, which were to be subjected to post-quenching (see 2.3.2), were synthesized. In order to produce free-standing Cu–Al–Ni films, Si substrates were covered with resin by spin coating before sputtering. Deposition was carried out from individual Cu, Al and Ni targets. The chamber pressure applied during sputtering was set to  $3 \times 10^{-3}$  Torr. Seven layers were prepared consisting of three Al layers deposited between four co-deposited Cu and Ni layers (Figure 2.6).



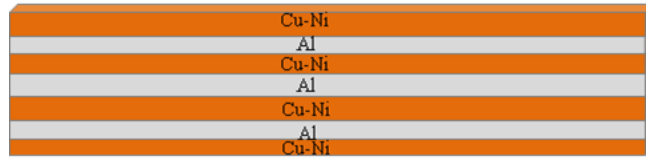


**Figure 2.6 Scheme of the sputter deposited multilayers before heat treatment**

DC (Direct Current) sputter deposition was used for Cu and Al whereas RF (Radio Frequency) sputter deposition was applied for Ni. For the top and bottom Cu-Ni layers, half of the deposition time applied for the Cu-Ni layers in between was applied. The details of the deposition conditions of the layers between the top and bottom Cu-Ni layers can be seen in Table 2.1. After the deposition, the samples were rinsed in acetone and alcohol, respectively, to have the resin dissolved and the film separated from the substrate. In order to trigger alloying between the layers, post-quenching was applied (see 2.3.2) following heat-treatment and Cu–Al–Ni thin films were obtained.

**Table 2.1 Sputter Deposition conditions applied for layers between the top and bottom Cu-Ni layers. Note: The top and bottom layers were produced using half the duration specified in the table**

	Cu-Ni			Al	
	P(W)		t(min)	P(W)	t(min)
	Cu	Ni			
Cu-14Al-4Ni (wt%)	200	60	10	200	14
Cu-13Al-5Ni (wt%)	200	75	9	200	15.5
Cu-12Al-7Ni (wt%)	200	85	10	200	17

### 2.2.2 High Temperature Sputter Deposition

For the sputter deposition of Cu–Al–Ni along with in-situ heat treatment, MgO (001) was chosen as the substrate due to its stability at high temperature and the low lattice mismatch between the lattice parameters of MgO (001) and austenitic  $\beta$  phase of Cu–Al–Ni (Figure 2.7). After being cleaned with acetone and isopropanol, the substrate was dried by an air gun.

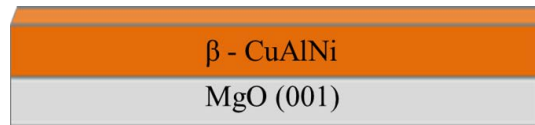


**Figure 2.7 Scheme of austenitic Cu–Al–Ni grown on MgO (001) substrate**

Ultra-high vacuum sputtering equipment (Figure 2.8a), located at the Device Materials Group at University of Cambridge, was used. The flange employed is shown in Figure 2.8b. The magnetrons were water cooled to avoid target heating during deposition. Stainless steel shielding was used in order to minimise cross-contamination



between targets. The heater used consisted of a uniform strip of Ta foil on which the substrate is placed. A constant DC current was passed by low resistance copper arms. Deposition was carried out from individual Cu, Al and Ni targets simultaneously.

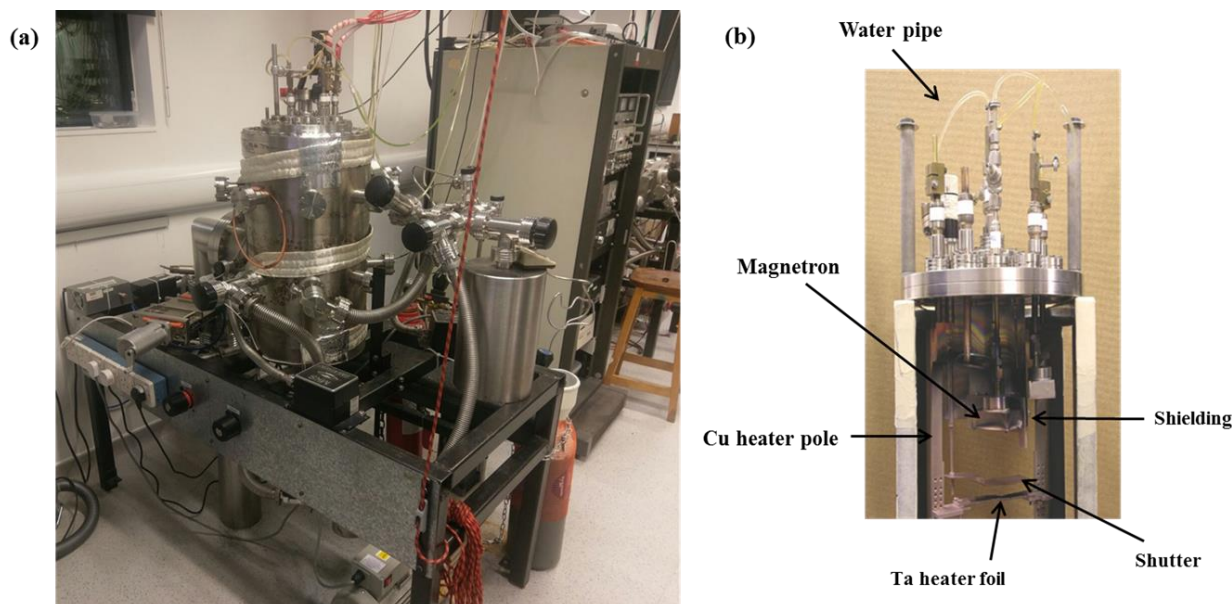


**Figure 2.8 (a) Sputtering system and (b) Side view of the flange used for high temperature deposition**

In order for high vacuum to be provided, the system was pumping overnight. Deposition of Cu-12Al-7Ni (wt%) thin film was carried out applying the power values listed in Table 2.2.

**Table 2.2 Power values applied at the three targets to obtain Cu–12Al–7Ni (% wt) thin films**

Metal target	Power (W)
Cu	22
Al	30
Ni	5

$4.5 \times 10^{-3}$  Torr Ar pressure was used. The duration for deposition was 2.5 hours. For high temperature conditions to be provided, a heater, adjusted to 700 °C, was connected to the equipment. No pre-heating of the substrate was applied. After the deposition, the sample was post-annealed for 10 minutes at the same temperature.

### 2.3 Heat treatment

Heat treatment was required for electrodeposited BiFeO<sub>3</sub> and sputter deposited Cu–Al–Ni shape memory system to obtain the required crystallographic structures. A Carbolite MTF 9/15/130 tubular furnace (Figure 2.9) was used for the heat treatment processes.

### 2.3.1 Equilibrium Heat Treatment

Heat treatment was useful in order to induce crystallization in as-deposited amorphous Bi–Fe–O films. The heating rate used was 1°C/min. The as-deposited samples were subjected to heat treatments at 500, 600, 700 and 800 °C for 2 h. After the treatment, the samples were cooled in air.

For the epitaxial growth of the austenitic Cu–Al–Ni thin films, heat treatment was applied along with the growth of the film (see 2.2.2).



Figure 2.9 Tubular furnace used for heat treatment processes

### 2.3.2 Post-quenching

It is well-known that post-quenching is an effective way of introducing martensitic transformation behaviour in Cu–Al–Ni shape memory alloys [2]. The sputtered Cu–Ni and Al layers were heat treated at high temperature in order to provide, primarily, the mixing between the layers and, secondly, the formation of the required crystallographic structure. Upon heat treatment, the samples were quenched in iced water to obtain the desired phases. The samples were wrapped in Ta foils and placed in a sealed quartz tube while being treated. Cu–14Al–4Ni (wt%) and Cu–13Al–5Ni (wt%) samples were held at 900 °C for 60 min before becoming quenched in iced water whereas Cu–12Al–7Ni (wt%) samples were held at 800 °C for 60 min.

## 2.4 Thickness Measurement

Confocal microscope is an optical imaging technique for increasing optical resolution and contrast of a micrograph via using a spatial pinhole to block out-of-focus light in image formation. Reconstruction of three-dimensional structures within an object is acquired by capturing multiple two dimensional images at different depths in a sample [3].

Thickness measurements were carried out using a 3D Optical Surface Metrology System Leica DCM 3D confocal microscope, which is located at UAB microscopy service. The magnification used was 50X. The thickness calculated for bismuth ferrite samples was 10  $\mu\text{m}$ . For the Cu–Al<sub>12</sub>–Ni<sub>7</sub> (wt %) film grown on MgO substrate at 700 °C, the calculated value was 650 nm. Table 2.3 shows the thickness values of the sputtered and subsequently heat treated multilayers.

**Table 2.3 Thickness values of the free-standing Cu–Al–Ni films obtained by holding the samples at high temperature followed by heat treatment**

Sample	Total thickness
Cu-14Al-4Ni (wt%)	950 nm
Cu-13Al-5Ni (wt%)	915 nm
Cu-12Al-7Ni (wt%)	1.25 $\mu\text{m}$

## 2.5 Scanning Electron Microscopy (SEM)

Scanning electron microscopes scan the surface of a sample with a focused beam of electrons. It allows the investigation of structures that are too small to be investigated by optical microscopes.

### Interaction Between the Electron Beam and the Sample

Different signals are produced when a surface is exposed to a bombardment by electrons. The incidence angle of the beam, the magnitude of its current, the accelerating voltage and the average atomic number ( $Z$ ) of the sample determines the penetration depth of the electrons. Several interactions between the electron beam and the surface atoms occur in the volume of the interaction. As a result, different types of signals are produced (Figure 2.10):

#### Auger Electrons:

These electrons become emitted due to de-energization of the specimen atom after a secondary electron is produced. As a core (usually K-shell) electron becomes emitted from the atom during the secondary electron process, a vacancy forms. A higher energy electron from the same atom can fall into this vacancy. This condition results in an energy surplus in the atom which can be corrected by emitting an outer (lower energy) electron; an Auger electron. The energy and depth range of these electrons are between 0.5 and 2 nm. No information from the internal parts of the sample can be obtained by Auger electrons but the energy of these electrons is

characteristic for the emitting atom. So, composition information can be gathered from the small regions on the sample surface.

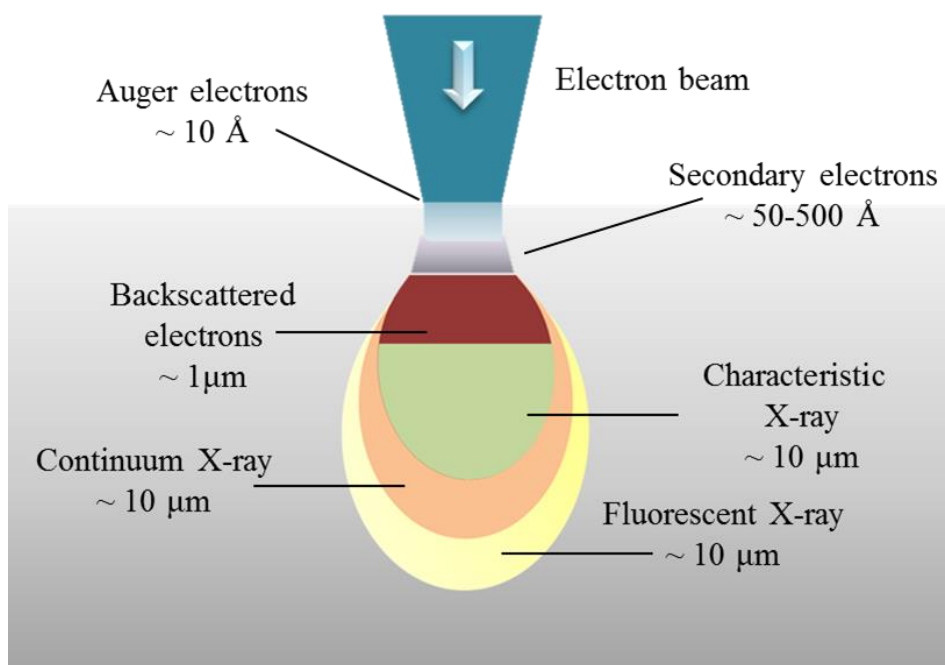


**Figure 2.10 Schematic illustration of various electron-specimen interactions**

### **Secondary Electrons:**

These electrons are produced when an incident electron excites an electron in the sample and loses some of its energy in the process. The excited electron suffers elastic and inelastic collisions until it gets the surface. From here it can escape if its energy exceeds the surface work function ( $E_w$ ), which is the amount of energy needed to remove electrons from the surface of a material. Secondary electrons are characterized by energies between 0 and 50 eV. They provide information on the topography of the surface. However, all information obtained from secondary electrons is restricted to a penetration between 5 and 50 nm.

### **Backscattered Electrons:**

Backscattered electrons are produced when the electron beam interacts elastically with the nuclei of the surface atoms. The intensity of the effect changes with respect to the atomic number of the elements present in the sample. It is useful at obtaining maps with information about the composition of the sample surface. Elements with high atomic numbers backscatter more strongly than elements with low atomic numbers which results in brighter images to form for the heavy elements.

### **Characteristic X-rays:**

As a result of a collision between an incident electron beam with a sample atom inducing the emission of another electron, the corresponding hole is directly occupied by an electron from an outer higher energy shell. The energy

difference between the higher energy shell and the lower energy shell becomes released as an X-ray. The wavelengths of the emitted X-rays are characteristic of the sample atoms. The spectrum obtained is used to study the elemental composition of the sample and it is named as Energy Dispersive X-ray Spectroscopy (EDX) pattern.

The EDX analysis and morphological characterization of the samples were carried out by Merlin Zeiss SEM located in the Microscopy Service of the Universitat Autònoma de Barcelona. For morphological investigation 2 kV was used, whereas 15 kV was applied for EDX analysis.

## 2.6 X-ray Diffraction (XRD) Method

X-ray diffraction is a commonly used characterisation method that is useful at giving information about the structure of the samples. The phases in a sample, the presence of any texturing, the degree of crystallinity, lattice parameters, and the crystallite sizes can be determined by this method. It is non-destructive and the sample preparation is minimal.

In this method, it is assumed that the incident X-ray beam is monochromatic (a single wavelength) and is perfectly collimated. Once a crystal with an interplanar spacing,  $d$ , (crystal lattice constant) is irradiated by X-ray beam with a comparable wavelength,  $\lambda$ , the X-ray diffraction, or the constructive interference between elastically scattered X-ray beams can be observed at specific angles when the Bragg's Law (Figure 2.11) is satisfied.

$$n\lambda = 2d_{hkl} \sin \theta \quad \text{Equation 2.1}$$

where  $n$  is the order of reflection,  $d_{hkl}$  is the interplanar distance of crystallographic planes belonging to the same family (h,k,l) and  $\theta$  is the scattering angle.

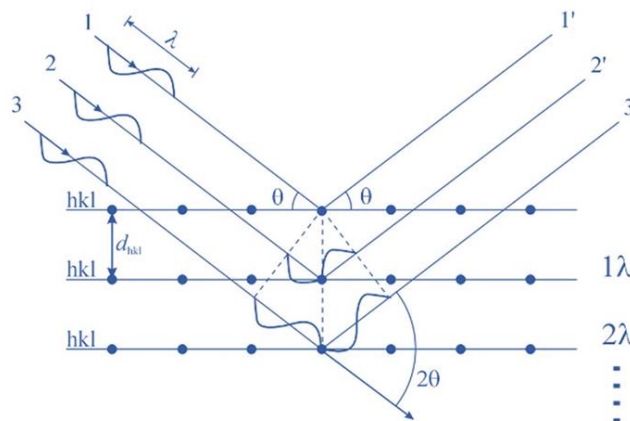


Figure 2.11 Bragg's Law [4]

In case this relationship is satisfied, X-rays are in phase and form a constructive interference. It can be used to determine the angular position of peaks in a particular family of diffracted planes. The crystal is assumed to be perfect in Bragg's Law. The possible presence of structural defects is ignored. The crystal sizes and the microdeformations affect the width of the diffracted peaks. The crystallite size is calculated considering that the peaks can be adjusted to a pseudo-Voigt function, which is a linear combination of Gaussian and Lorentzian (Cauchy) functions. The crystal size can be determined from the Lorentzian as the integral of the peak width  $\beta_C^f$ :

$$d_{hkl} = \frac{\lambda}{\beta_C^f \cdot \cos \theta} \quad \text{Equation 2.2}$$

where  $\theta$  is the angular position of the peak (in degree) and  $\lambda$  is the wavelength. This equation is named as the Scherrer formula. Additionally, the microdeformations can be determined from the Gaussian contribution upon integrating the peak width  $\beta_G^f$ :

$$\text{microdeformation} = \langle e \rangle = \frac{\beta_G^f}{4 \tan \theta} \quad \text{Equation 2.3}$$

### **Bragg-Brentano (BB) Geometry**

Powder diffractometers generally use Bragg-Brentano parafocusing geometry (Figure 2.12) offering high-resolution and high beam-intensity analysis at the cost of very precise alignment requirements and carefully prepared samples [5].

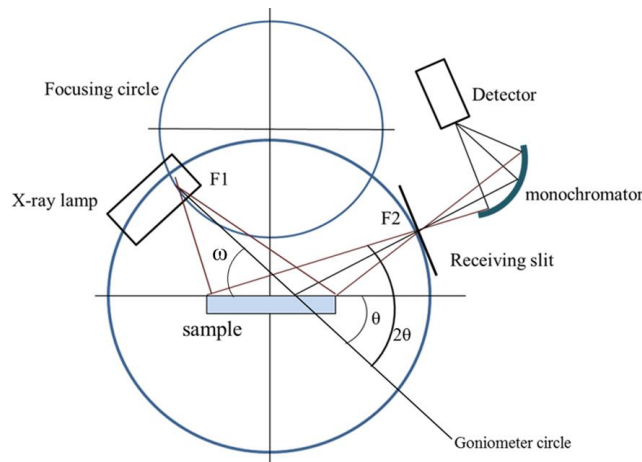


**Figure 2.12 Bragg-Brentano geometry**

The incident angle  $\omega$  between X-ray source and the sample is always 1/2 of the detector angle  $2\theta$ . By varying  $\omega$  and  $\theta$  values and ratios, different types of scans are possible:

- 1)  $\omega:2\theta$  or  $\theta:2\theta$  scan: with the X-ray tube fixed, the sample rotates at  $\theta/\text{min}$  and the detector always at  $2\theta/\text{min}$ ;
- 2)  $\theta:\theta$  scan: the sample is fixed and the tube rotates at the same rate as the detector at  $\theta/\text{min}$ .

The surface of the sample is placed on the tangent plane of the focusing circle defined by three spots of sample, X-ray source and receiving slit.

The incident- and diffracted-beam slits move on a circle that is at the center of sample surface. Divergent X-rays from the source hit the sample at different points on its surface. During the diffraction process the X-rays are refocused at the detector slit.

### **Parallel-Beam (PB) Geometry**

Regardless of the sample shape, PB optics (Figure 2.13) provides precise measurement of diffracted X-ray positions. It is quite useful at analysing powder sample profiles, the degree of preferred orientation and thin films [5].

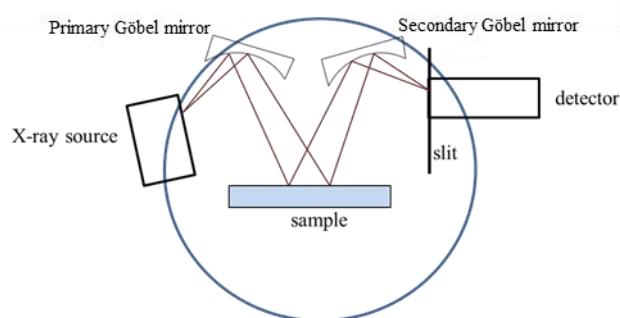


**Figure 1.13 Parallel beam geometry**

The use of parallel beam, which is monochromated to  $K_{\alpha}$  radiation by optical devices such as Göbel mirrors, is an effective way to minimize the reflection of the single crystal substrates while investigating thin film coatings [6].

A polycapillary collimating optic (Göbel Mirror) is used to form an intense parallel X-ray excitation beam resulting in very high X-ray intensities at the sample surface.

There are no restrictions on XRD configuration unlike there is for BB geometry which allows broader range of sample shapes and sizes.

### **In plane Pole Figure Reflection Method**

The diffractometer angles can be altered in the axes mentioned below to obtain details about crystal structure (Figure 2.14) [7].

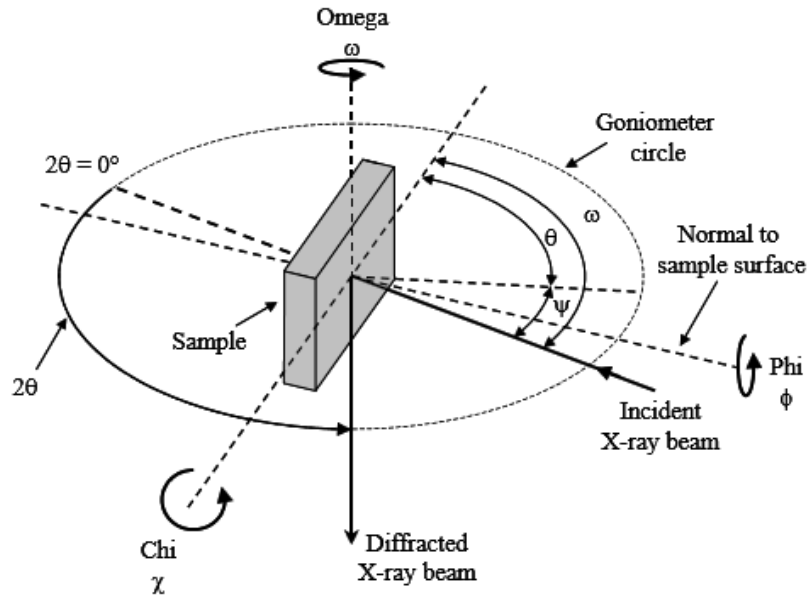


Figure 2.14 Angles and rotations used in XRD measurement [7]

### **2-theta ( $2\theta$ )**

The Bragg angle is the angle between the incident (transmitted) and diffracted X-ray beams.

### **Omega ( $\omega$ )**

The angle between the incident X-ray beam and the sample surface is the omega angle. Both omega and 2-theta lie in the same plane.

### **Phi ( $\phi$ )**

The angle of rotation of the sample about its surface normal is the phi.

### **Chi ( $\chi$ )**

Chi rotates in the plane normal to that containing omega and 2-theta.

### **Psi ( $\psi$ )**

An angle through which the sample is rotated is the  $\sin^2\psi$  method. Typically, at  $\psi = 0$ , where omega is half of 2-theta and add (or subtract) successive psi offsets, for example, 10, 20, 30 and 40° is the starting point.

XRD patterns of bismuth, bismuth ferrite and post-treated Cu–Al–Ni thin films were acquired by a Philips Bragg Brentano X'Pert diffractometer (Almelo, The Netherlands) in the X-ray Diffraction Service of Universitat Autònoma de Barcelona. Cu  $K\alpha$  radiation was used.



The  $2\theta$  range used was  $20^\circ$ – $75^\circ$  for bismuth samples. The step size used was  $0.0026^\circ$  and the step time was 200 s. Rietveld refinement using MAUD (Materials Analysis Using Diffraction) software [8] was carried out to determine the lattice parameters. Crystallite size was calculated by profile fitting using the Williamson-Hall plot option in the X'Pert HighScore Plus software (PANalytical, Almelo, The Netherlands).

For bismuth ferrite samples the  $2\theta$  range used was  $20^\circ$ – $60^\circ$ . The step size used was  $0.0026^\circ$  and the step time was 600 s. Rietveld refinements of the XRD patterns using the MAUD software were carried out to determine the crystallite size of the main phases.

Post-quenched Cu–Al–Ni shape memory thin films were  $2\theta$  scanned between  $20^\circ$ – $90^\circ$  with a step size of  $0.0026^\circ$  and a step time of 1000 s. X'Pert HighScore Plus software was used for the analysis of the samples.

Cu–Al–Ni sample grown on MgO substrate at  $700^\circ\text{C}$  was investigated by Philips X'Pert Parallel Beam XRD equipment at X-ray Facilities of University of Cambridge. The  $2\theta$  range scanned was  $20^\circ$ – $90^\circ$  with a step size of  $0.0025^\circ$  and a step time of 1500 s. In order to detect the rotation angle between the substrate and the film,  $\varphi$  scan was carried out for the (022) peak that was acquired from the  $2\theta$  scan.

## 2.7 Transmission Electron Microscopy (TEM)

The principle of TEM is based on the emission of electrons driven toward the object under observation by a system of magnetic lenses and the detection and visualization of electrons passing through the specimen (Figure 2.15). The objective lens gathers the transmitted beam and forms the image display. The objective and selected area aperture are used to choose the elastically scattered electrons that will form the image and the projector lens. A monitor displays the formed image. TEM operates at an ultra-high vacuum and at a high voltage. The specimens should have quite low thickness in order to have transparency for electrons.

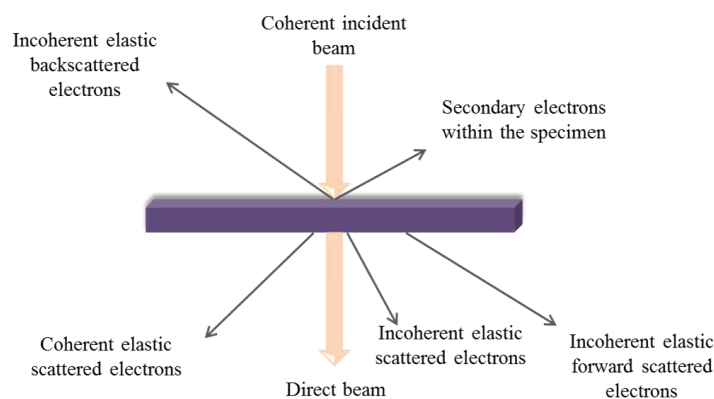


**Figure 2.15 Schematic representation of the generation of the electron signal in TEM**

The different types of signals in TEM are described:

**Elastic scattering:** It is formed by coherently scattered electrons like electrons scattered in the forward direction, nearly parallel to the incident beam direction.

**Imaging:** Elastic scattering of electrons by the Coulomb potential of the nucleus is the most important interaction which contributes to image contrast. The contribution of different parameters to the elastic scattering are expressed by the atomic scattering factor  $f(\theta)$ , which is the measure of the amplitude of an electron wave, scattered from an isolated atom.  $|f(\theta)|^2$  is proportional to the scattered intensity:

$$f(\theta) = \frac{1 + \left(\frac{E}{E_0}\right)}{8\pi^2 a_0} \cdot \left(\frac{\lambda}{\sin\theta/2}\right)^2 \cdot (Z - f_x) \quad \text{Equation 2.4}$$

Where  $\theta$  is the scattering angle,  $E_0$  is the rest energy of a single electron ( $E_0 = mc^2$ ),  $E$  the beam energy in keV,  $a_0$  the Bohr radius of the scattering atom,  $\lambda$  the wavelength,  $Z$  the atomic number and  $f_x$  the scattering factor for X-ray.

**Diffraction:** When no aperture is placed in the back focal plane of the objective lens, the diffraction pattern itself can be observed and recorded. Inserting an aperture at the image plane of the objective lens allows us to select the field from which the diffracted information is acquired; this is referred to as selected area electron diffraction (SAED). The use of such an aperture makes it possible to obtain diffraction from small portions of the specimen. In this way, a direct correlation can be made between the morphological information obtained by imaging and the crystallographic information obtained by diffraction from very small areas. Typical intermediate aperture sizes range from 50  $\mu\text{m}$  to 5  $\mu\text{m}$ . The necessary condition to obtain diffraction is represented by Bragg's Law (Equation 2.1). This equation can be simplified taking into account the small wavelength for electrons in TEM as:

$$n\lambda = 2d \cdot \theta \quad \text{Equation 2.5}$$

Planes that are parallel (with a few degrees) to the incident beam will be represented in the diffraction pattern by a diffraction spot located along the normal of the crystallographic plane it represents and at a distance  $\lambda L/d$  from the center of the diffraction pattern.  $L$  is the camera length and  $\lambda L$  is the camera constant. Assuming that  $n=1$ , for small angles  $2\theta = R/L$ .  $Rd = \lambda L$  is obtained. Then  $R$  is inversely proportional to  $d$  spacing so simply measuring  $R$  on the pattern  $d$  can be obtained.

**Inelastic scattering:** is concentrated within smaller scattering angles and the excitation of energy states results in energy losses. The dominant mechanisms are plasmon and interband excitations, which can be described by the dielectric theory. These inelastic scattering processes are less localized than elastic scattering and cannot contribute to high resolution. Inner shell ionizations result in edge-shaped structures in the electron energy loss spectrum (EELS) which can be used for analytical electron microscopy at high resolution.

**EDX:** For generation of characteristic X-rays and their role in characterisation see section 2.5.

**EELS:** EELS signal is the result of the inner-shell ionisation of atoms by the primary electrons. The electron that ionized the atom is deviated only a small angle ( $\leq 10 \text{ mrad}$ ) since its loss in energy is quite small, and it is likely to pass through the sample. These inelastically scattered electrons with a characteristic energy of  $E = E_0 - E_{\text{binding}}$  are measured by EELS microanalysis. EELS tends to work at its best at relatively low  $Z$ -number atoms. Specimen thickness is very crucial for EELS analysis and should be less than 50 nm. With EELS, atomic composition, chemical bonding, valence and conduction band electronic properties, surface properties and element-specific pair distance functions can be studied. EELS has the ability to determine local electronic structures for the extraction of local chemical bonding by analysing near-edge and to extend fine structures of ionization edges. EELS has a better resolution than EDX because the sample volume which provides the information can be defined by apertures confining the collection angle of the spectrometer.

TEMs might be divided into two main groups: low voltage TEM and high voltage (high resolution, HR) TEM. In the former the energy of electrons does not exceed 120 keV, whereas electrons with 200 keV are used in the latter one.

The TEM investigations were made on a JEOL JEM-2011 microscope operated at 200 kV, equipped with an EDX detector from Oxford, located at the Microscopy Service of the Universitat Autònoma de Barcelona.

## 2.8 Vibrating Sample Magnetometry (VSM)

The principle of a magnetometer is to measure the electromotive force formed by a ferromagnetic sample while it is vibrating sinusoidally, usually by a piezoelectric material, in the presence of a static and uniform magnetic field ( $H$ ). In Faraday's law, the electromotive force induced in a coil,  $V_{\text{fem}}$ , is proportional to the temporal variation of the magnetic flux,  $\phi$ , passing through it.

$$V_{\text{fem}} = -\frac{d\phi}{dt} \quad \text{Equation 2.6}$$

Where  $\theta$  is the magnetic flux and  $t$  is the time.

Linear attenuator based components are used in VSMs which were initially obtained by modifying audio speakers. This approach was dropped due to the interference through the in-phase magnetic noise produced, as the magnetic flux through a nearby pickup coil varies sinusoidally.

Assuming a solenoid to be consisting of  $N$  turns for a constant cross-section,  $A$ , the magnetic induction inside the coil,  $B$ , can be expressed as follows:

$$B = \frac{\phi}{A} N \quad \text{Equation 2.7}$$

Therefore,

$$V_{fem} = -NA \frac{dB}{dt} \quad \text{Equation 2.8}$$

As the sample is vibrating, the magnetic moment can be expressed as  $m(t) = m_0 \sin(ft)$ , where  $m_0$  is the moment amplitude and  $f$  is the frequency. As  $B = \mu_0(H + M)$ ,  $M = m/V$  ( $B$  being the magnetic induction,  $M$  the magnetization and  $V$  the volume of the sample,  $\mu_0$  the permeability of free space and  $H$  is constant),  $dB/dt$  can be obtained as follows:

$$dB / dt = (\mu_0 mf / V) \cos ft \quad \text{Equation 2.9}$$

So, the amplitude induced voltage in the pickup coil is proportional to the sample's magnetic moment, but it is independent from the strength of the applied magnetic field:

$$V_{fem} \propto f \mu_0 G(z) \quad \text{Equation 2.10}$$

where  $G(z)$  is a function that defines the dependence of  $V_{fem}$  to the sample position in the holder relative to the coils. Thus, it is dependent on the design of the coils. In principle, the VSM measures the difference of magnetic induction between one region of space with the sample and another without the sample. This situation allows calculation of the magnetic moment ( $m$ ), and obtaining the hysteresis loops of a certain material. A schematic diagram of different components of VSM is shown in Figure 2.16

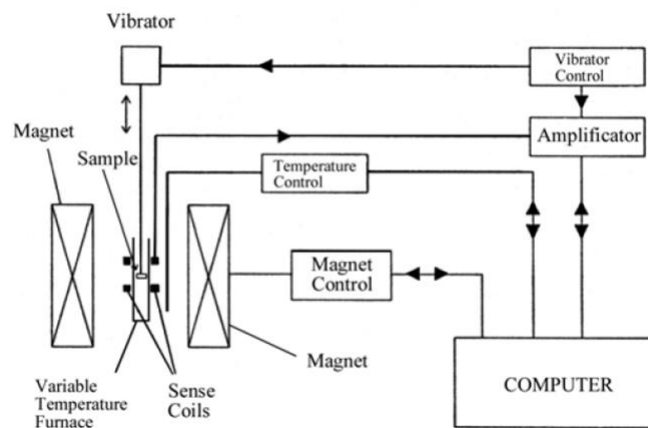


**Figure 2.16 Schematic diagram of different components of VSM**

For the VSM measurements a Micro-Sense (LOT-Quantum Design) VSM (Fig. 2.17), located at the Gnm<sup>3</sup> group, with a maximum applied magnetic field of 2 T generated by an electromagnet was used. The sample is located at the end of a rigid holder which is oscillated in the vertical direction, perpendicular to the magnetic field. All measurements were carried out at room temperature.



Figure 2.17 The VSM equipment used

## 2.9 Electrical resistance (ER) –Temperature (T) Measurements

The electric resistance (ER) change with respect to temperature is a commonly used method for shape memory alloys to detect the transformation temperatures of the thermoelastic martensitic transformation. This technique exploits the resistivity change due to the electronic structure modification within a temperature domain [9].

To figure out martensitic transformation characteristics in austenitic Cu–12Al–7Ni (wt%) shape memory samples, ER measurements were carried out. It was implemented by a standard 4-point geometry using a constant current supply and standard digital voltmeters. The equipment is located at the Device Materials Laboratory of University of Cambridge. Spring-loaded pins placed in the corners of the sample were used to make contact with the film. The resistance was measured between 50 K and 300 K by applying a heating rate of 2 K/min.

## References

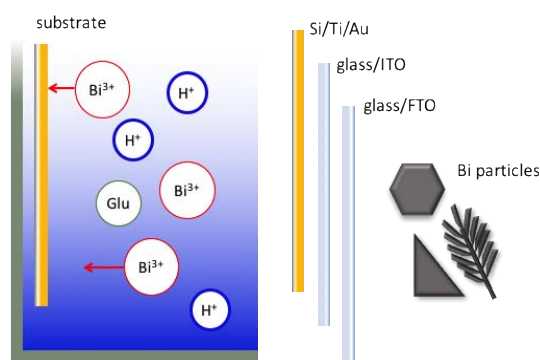
- [1] Kwak, D. J., Moon, B. H., Lee, D. K., Park, C. S., Sung, Y. M. Comparison of Transparent Conductive Indium Tin Oxide, Titanium–Doped Indium Oxide, and Fluorine-Doped Tin Oxide Films for Dye-Sensitized Solar Cell Application. *Journal of Electrical Engineering and Technology*, 6 (2011), 684–687.
- [2] Humbeeck, J. V., Chandrasekaran, M., Delaey, L. The Influence of Post Quench Aging in the Beta-Phase on the Transformation Characteristics and the Physical and Mechanical Properties of Martensite in a Cu–Al–Ni Shape Memory Alloy. *ISIJ International*, 29 (1989), 388–394.
- [3] Johnston, D., Page, A. *Confocal Microscopy–Principles and Applications*. Southampton University, Biomedical Imaging Unit. 2009
- [4] *Development of X-ray Crystallography*, University of Illinois at Urbana-Champaign.  
<https://publish.illinois.edu/x-raycrystallography/2014/12/18/introduction/>
- [5] XRD Principle, Yale University, West Campus X-ray Characterization Core.  
<https://ywcmatsci.yale.edu/principle-0>
- [6] Nagao, K., Kagami, E. X–ray Thin Film Measurement Techniques: VII. Pole Figure Measurement. *The Rigaku Journal*, 27 (2011), 6–14.
- [7] Fitzpatrick, M., Fry, A., Holdway, P., Kandil, F., Shackleton, J., Suominen, L. *Determination of Residual Stresses by X-ray Diffraction*. National Physical Laboratory. Teddington. 2005.
- [8] MAUD (Materials Analysis Using Diffraction), <http://maud.radiographema.com/>
- [9] Airoidi, G., Lodi, D. A., Pozzi, M. The Electric Resistance of Shape Memory Alloys in the Pseudoelastic Regime. *Le Journal de Physique IV*, (1997), 507–512.

### 3. Results and Discussion

#### 3.1 Electrodeposition of Bismuth

Bismuth (Bi) is a semi-metal currently involved in a number of cutting-edge applications, ranging from electroanalysis to energy harvesting (e.g. BiTe thermoelectric material). Therefore, studies focusing on the production of Bi in either form (films, particles, wires) as well as the effect of the synthesis variables are timely and relevant. In this work, Bi particles with micrometer and submicrometer sizes are prepared by electrodeposition from an aqueous acid bath onto three different substrates, namely Si/Ti/Au, indium tin oxide (ITO)- and fluorine tin oxide (FTO)-coated glasses (Scheme 3.1).

The effect of gluconate addition to the electrolyte and the shape and size of the particles as a function of the deposition potential and substrate type will be discussed.



**Scheme 3.1 Schematic figure of bismuth electrodeposition onto three different substrates**

##### 3.1.1 Cyclic Voltammetry (CV) Studies

The CV responses from 5 mM  $\text{Bi}(\text{NO}_3)_3 \cdot 5\text{H}_2\text{O}$  + 1.5 M  $\text{HNO}_3$  electrolyte onto Si/Ti/Au, glass/FTO, and glass/ITO substrates are shown in Figure 3.1a. Due to the different activity of the substrates, the onset of reduction is different, this being shifted towards more negative potentials within the series of Si/Ti/Au > glass/FTO > glass/ITO. Deposition of bulk Bi took place from  $-40$  mV on Au surface, in agreement with [1]. A diffusion-like peak was recorded in all cases. In the anodic scan, a single oxidation peak was recorded on all electrodes, as well, between  $-30$  and  $300$  mV.

Enhanced mass transfer provided by Ar bubbling through the electrolyte during the entire CV led to higher current densities in the cathodic scan and, concomitantly, higher oxidation currents in the anodic scan (not shown). In order to confirm that  $\text{H}_2$  co-evolution was not involved (or marginally involved) at the screened potentials in spite of the low pH, CVs including initiation of Ar purging at the positive sweep were carried out and compared to those obtained under stagnant conditions (Figure 3.1b). The oxidation current did not

decrease when the Ar flux was switched on at the crossover. Therefore, almost no H<sub>2</sub> bubbles had been previously adsorbed onto the cathode in the negative sweep. If that would have been the case, detachment of hydrogen bubbles from the surface due to Ar purging would have caused a significant decrease of the oxidation current.

The addition of gluconate to the electrolyte did not delay the onset of deposition but caused a shift toward more positive potentials (Figure 3.1c). This effect was more pronounced on Si/Ti/Au substrate than on glass/FTO and glass/ITO substrates. At the working pH, gluconate protonation takes place. Moreover, it has been reported that the protonation of gluconate is coupled with the lactonization of gluconic acid [2]. The ability of gluconic acid to bind metal ions is rather weak in acidic conditions [3] and this can explain why the onset of deposition is not shifted toward more negative potentials.

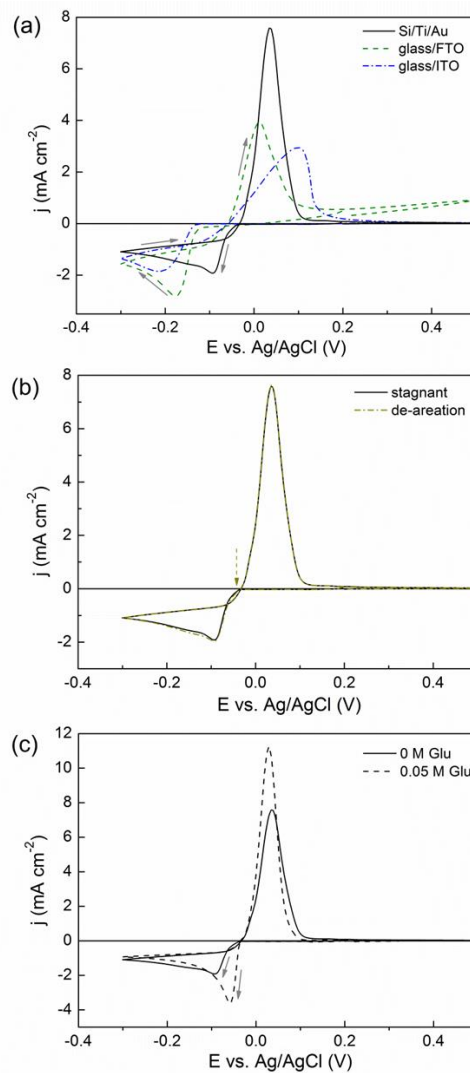


**Figure 3.1** CV curves recorded at  $50 \text{ mV}\cdot\text{s}^{-1}$  from  $5 \text{ mM Bi}(\text{NO}_3)_3\cdot 5\text{H}_2\text{O} + 1.5 \text{ M HNO}_3 + x \text{ M NaC}_6\text{H}_{11}\text{O}_7$  with (a)  $x = 0$  onto different substrates in stagnant conditions, (b)  $x = 0$  onto Si/Ti/Au in stagnant and Ar-bubbling conditions (initiated at the crossover toward positive potentials as indicated by the dashed arrow), and (c)  $x = 0$  and  $x = 0.05$  onto Si/Ti/Au in stagnant conditions



### 3.1.2 Potentiostatic Deposition and Morphological Characterization of Deposits

Micrometer- and submicrometer-sized Bi particles were grown by applying constant potentials between  $-0.20$  and  $-0.28$  V, i.e., within 80 mV interval, for deposition times ranging from 120 to 800 s. Noisy  $j$ - $t$  curves were recorded (Figure 3.2) as argon was made to continuously bubble during deposition. For all three electrodes, higher current density was measured as the applied cathodic potential was made more negative.

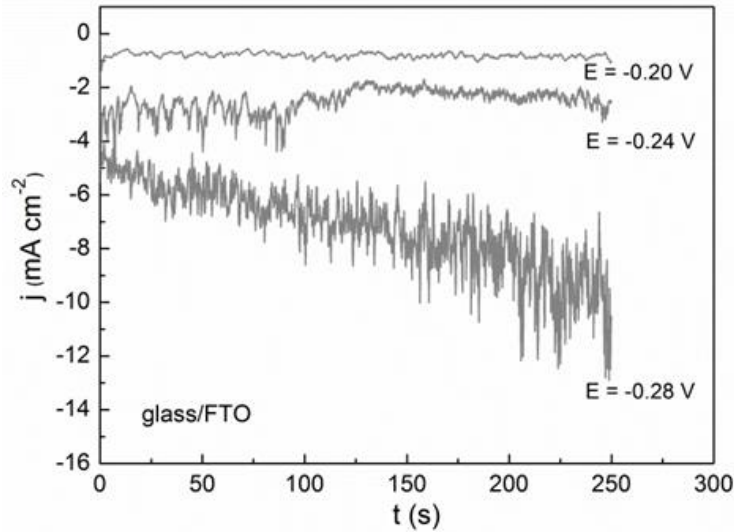


**Figure 3.2** Current density-time ( $j$ - $t$ ) curves recorded from 5 mM  $\text{Bi}(\text{NO}_3)_3 \cdot 5\text{H}_2\text{O}$  + 1.5 M  $\text{HNO}_3$  onto glass/FTO electrode under Ar bubbling

The cathodic potential could not be extended beyond  $-0.3$  V, especially on glass/ITO, as ITO suffered from instabilities at such acidic pH during cathodic polarization, mostly causing an abrupt increase of the resistance [4]. Moreover, since  $\text{SnO}_2$  in both FTO and ITO gets dissolved in the solution at high cathodic potentials in the low pH media, the bath cannot be reused further [5].

Immediately after deposition, deposits were rinsed in deionized water and dried in hot air. It was noticed that a  $\text{N}_2$  flux was not fully efficient to dry the deposits, i.e., in many cases the particles displayed an intricate morphology and remained wet. Meanwhile, if the samples were left to dry spontaneously, the remaining water droplets were capable of fully oxidizing the Bi film.

The substrate type had an obvious impact on the particles' shape. For example, sharper dendrites were observed on glass/FTO than on glass/ITO under identical deposition conditions (Figure 3.3). Deposition time also caused a change on particles' morphology. Deposits obtained on glass/ITO at low deposition times displayed highly-faceted incipient dendrites which evolved toward a more branched type at higher deposition times (Figure 3.4). Nevertheless, deposition times longer than 250–300 s were not recommended since detachment of the as-deposited material was observed.

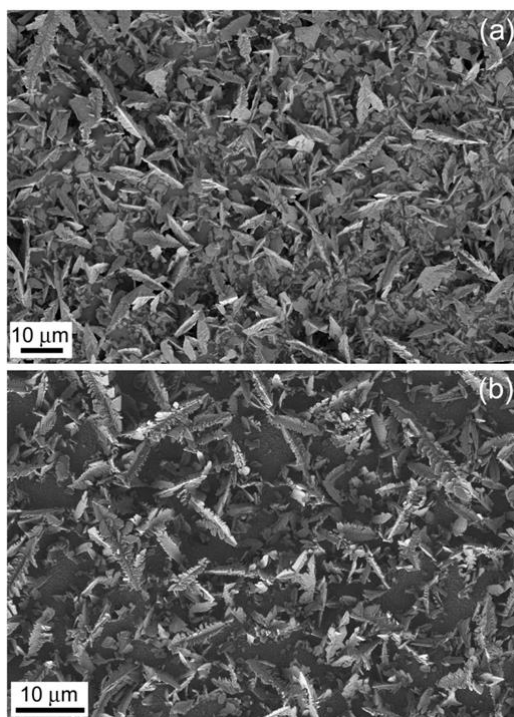


**Figure 3.3** SEM images of Bi deposits obtained from 5 mM  $\text{Bi}(\text{NO}_3)_3 \cdot 5\text{H}_2\text{O}$  + 1.5 M  $\text{HNO}_3$  bath under Ar bubbling at  $-0.28$  V for 250 s on (a) glass/ITO and (b) glass/FTO

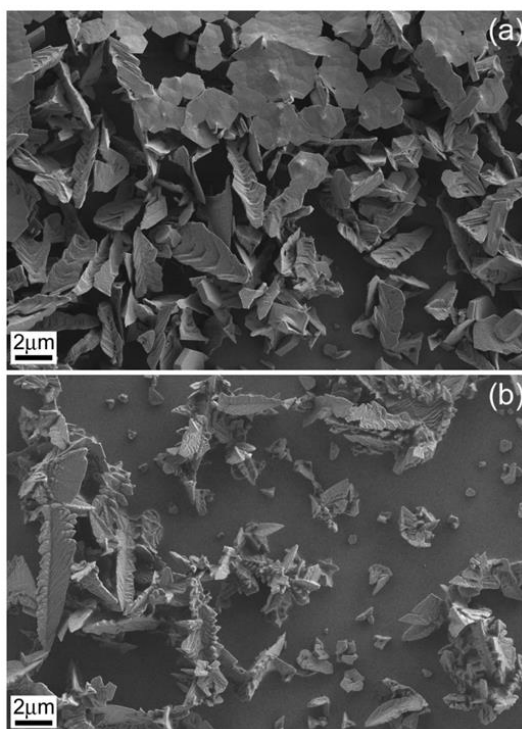


**Figure 3.4** SEM images of Bi deposits obtained from 5 mM  $\text{Bi}(\text{NO}_3)_3 \cdot 5\text{H}_2\text{O}$  + 1.5 M  $\text{HNO}_3$  bath under Ar bubbling at  $-0.28$  V on ITO/glass for (a) 120 s and (b) 800 s

The addition of gluconate to the electrolyte enabled the production of more uniformly covered substrates (Figure 3.5a,b). As aforementioned, gluconate mainly exists as gluconic acid in the bath. The complexing

capacity of gluconic acid is much lower than that of the gluconate anion [6]. As a result, gluconic acid acts as a throwing power additive rather than as a complexing agent. A representative energy dispersive X-ray (EDX) pattern is shown in Figure 3.5c, indicating the presence of Bi along with a residual contribution of O and the peaks coming from the substrate.

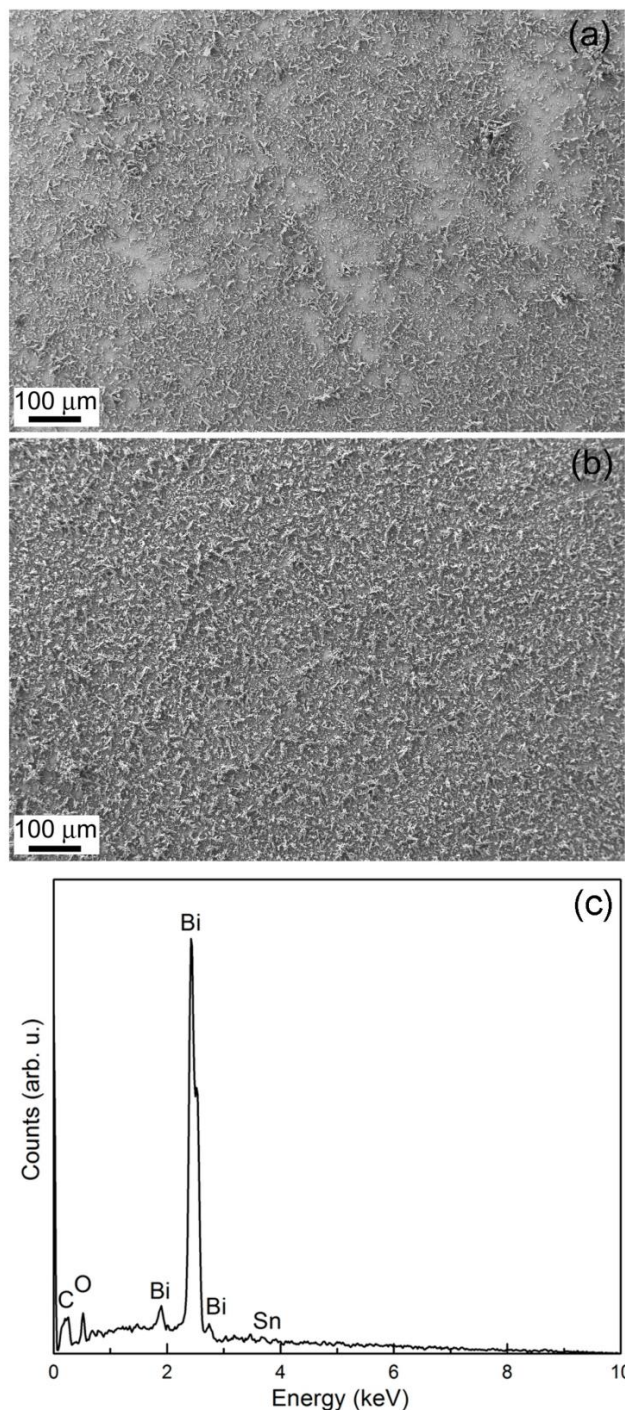


**Figure 3.5** Sample synthesized at  $-0.24$  V for 250 s on ITO/glass substrate from a bath with 5 mM  $\text{Bi}(\text{NO}_3)_3 \cdot 5\text{H}_2\text{O}$  + 1.5 M  $\text{HNO}_3$  + x M  $\text{NaC}_6\text{H}_{11}\text{O}_7$  for (a) x = 0 and (b) x = 0.05. (c) EDX pattern of the sample shown in (b)

Good adhesion was noticed on all substrates for deposition times up to 250 s. Applying longer durations caused detachments from the substrate, similar to the gluconate-free bath. Polyhedral particles and incipient dendrites were observed on glass/FTO at  $-0.20$  V (Figure 3.6). Dendrites continued to form at  $-0.24$  V and fully developed at  $-0.28$  V. A transition from polyhedrons to dendrites was also observed on Si/Ti/Au, although the particles looked much more pointed (i.e., triangles) at the lowest potential applied. Meanwhile, both incomplete and perfect hexagons were mostly found on glass/ITO at  $-0.20$  V. Dendrite formation started at  $-0.24$  V and progressed at  $-0.28$  V. Dendrites were sharper on glass/FTO and Si/Ti/Au substrates than on glass/ITO. It was, thus, clear that the particles' morphology was dependent on substrate type. The cathodic potential was not further increased as this caused the dendrites to detach from the substrate, in agreement with previous observations [1]. This transition from polyhedrons toward dendrites with slightly decreasing the potential was previously reported on glass/ITO substrate from a less acidic electrolyte and shorter deposition times [7].

The nature of the substrate influences the coating structure within the initial electrodeposition stages. Surface characteristics including surface finish (roughness), conductivity, and structure (amorphous, single-crystal, polycrystalline), have a decisive impact on the nucleation rate. In our case, Au is a metal whilst both ITO and FTO are semiconductors. Therefore, island nucleation and growth might be affected by substrate conductivity to a great extent [8]. This is clear upon observing when dendrites are formed, a phenomenon which is somehow delayed on both ITO and FTO compared to Si/Ti/Au substrates.

At  $-0.20$  V, the polyhedrons formed on Si/Ti/Au had sizes varying from 1 to  $4.5$   $\mu\text{m}$ . On glass/ITO, they had lengths between 1.4 and  $7$   $\mu\text{m}$  and width of  $1$   $\mu\text{m}$ . Meanwhile, polyhedrons with a width up to  $2$   $\mu\text{m}$  formed on glass/FTO, accompanied with dendrites up to  $4$   $\mu\text{m}$  in length and  $2$   $\mu\text{m}$  in width. As aforementioned, well-shaped hexagons were only observed on glass/ITO. In this case, their size distribution became narrower as the potential was made more negative; namely, at  $-0.20$  V they exhibited sizes ranging from  $600$  nm to  $3$   $\mu\text{m}$ , whereas at  $-0.24$  V  $1$   $\mu\text{m}$  sized hexagons were obtained. Concomitantly, dendrites with lengths up to  $7.2$   $\mu\text{m}$  and widths up to  $2$   $\mu\text{m}$  were seen on this substrate. Compared to glass/ITO, smaller dendrites formed on glass/FTO at  $-0.24$  V, with lengths reaching up to  $4$   $\mu\text{m}$  and widths of  $600$  nm. As the absolute value of the cathodic potential increased from  $-0.24$  V to  $-0.28$  V, the lengths of the dendrites showed an increase on each substrate up to  $10$   $\mu\text{m}$  and a decrease in their widths down to  $600$  nm.

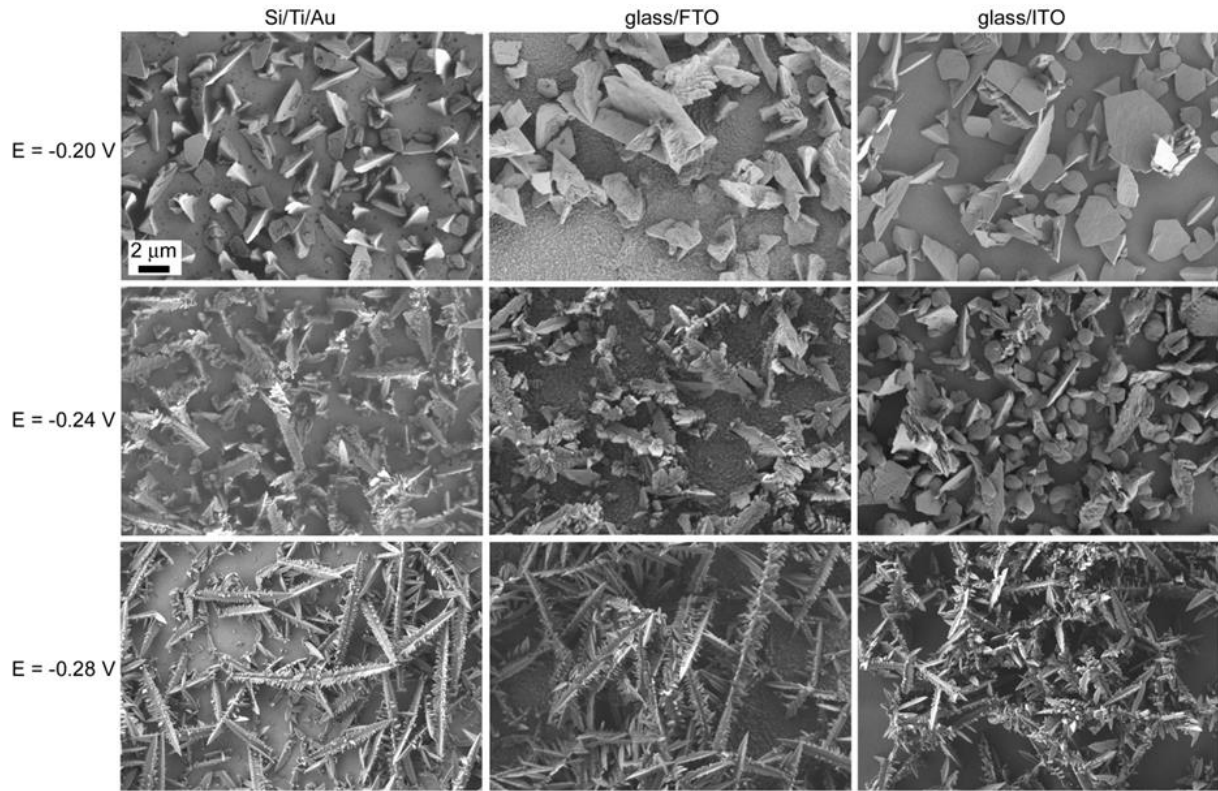


Figure 3.6 SEM images of bismuth electrodeposited at  $-0.20$  V,  $-0.24$  V and  $-0.28$  V for 250 s from 5 mM  $\text{Bi}(\text{NO}_3)_3 \cdot 5\text{H}_2\text{O}$  + 1.5 M  $\text{HNO}_3$  + 0.05 M  $\text{NaC}_6\text{H}_{11}\text{O}_7$  bath on Si/TiAu, glass/FTO and glass/ITO substrates. The scale bar is the same for all images

### 3.1.3 X-ray Diffraction Analysis

The collected X-ray diffraction (XRD) patterns indicated that single-phase deposits consisting of pure Bi crystallizing in the rhombohedral lattice (space group  $R\bar{3}m$ , classed into the hexagonal crystal system) were obtained irrespective of the applied potential and substrate type. In order to study the influence of the substrate on the microstructure, XRD patterns of Bi electrodeposited at  $-0.28$  V on Si/Ti/Au, glass/FTO, and glass/ITO substrates are presented in Figure 3.7a. At first glance, slight differences on the relative intensity of peaks among the deposits, which is indicative of texture, can be detected. To point this out, intensity ratios between the different reflections (i.e., (003), (104), etc.) and the most intense one (012) are calculated in Table 3.1. According to the  $I_{(hkl)}/I_{(012)}$  ratios obtained, Bi dendrites grown on Si/Ti/Au, glass/FTO, and glass/ITO substrates show a predominant orientation along the (003) plane (i.e., the plane parallel to the base of the rhombohedron). This orientation is exacerbated in the dendrites grown on the glass/ITO substrates.

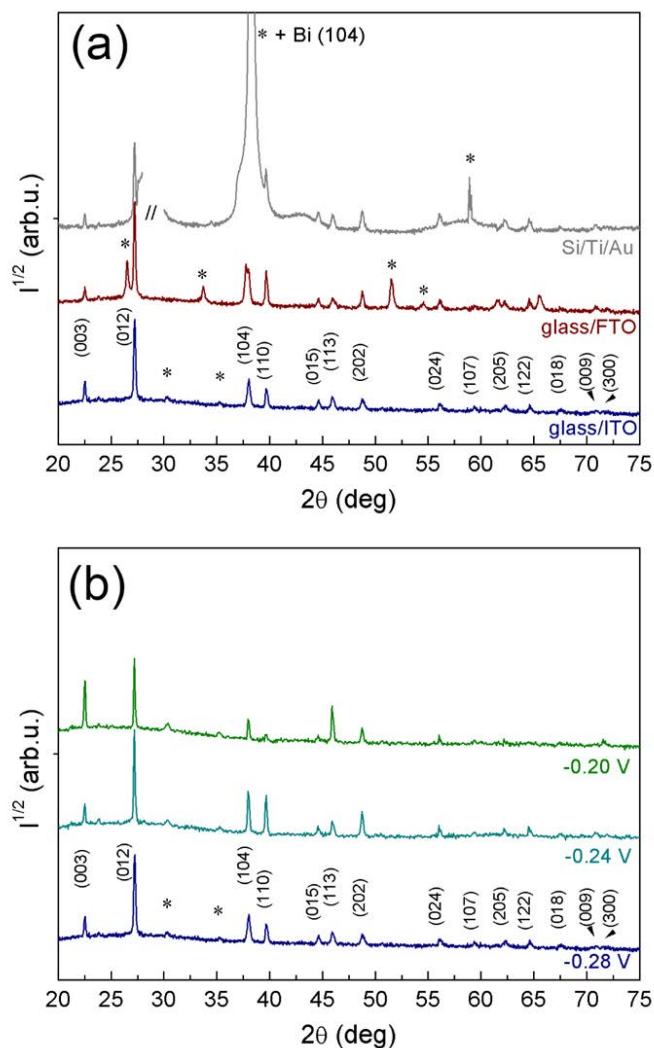


Figure 3.7 XRD patterns of Bi deposits obtained from 5 mM  $\text{Bi}(\text{NO}_3)_3 \cdot 5\text{H}_2\text{O}$  + 1.5 M  $\text{HNO}_3$  + 0.05 M  $\text{NaC}_6\text{H}_{11}\text{O}_7$  for 250 s (a) at  $-0.28$  V on Si/Ti/Au, glass/FTO, and glass/ITO substrates and (b) on glass/ITO substrates at  $-0.20$  V,  $-0.24$  V and  $-0.28$  V. Peaks denoted with (\*) belong to the substrate

Table 3.1 Theoretical (reference code 01-085-1329) and experimental intensity ratios, the latter determined from the XRD patterns shown in Figure 3.7 for Bi deposits obtained on glass/FTO, Si/Ti/Au, and glass/ITO

Plane	$I_{(hkl)}/I_{(012)}$ (%)					
	Theoretical	glass/FTO ( $-0.28$ V)	Si/Ti/Au ( $-0.28$ V)	glass/ITO ( $-0.28$ V)	glass/ITO ( $-0.24$ V)	glass/ITO ( $-0.20$ V)
(003)	5	9	7	16	17	62
(012)	100	100	100	100	100	100
(104)	33	24	–	18	26	17
(110)	34	19	30	11	23	7
(202)	16	7	6	5	12	10

Lattice parameters calculated by Rietveld refinement, as well as crystallite sizes determined by profile fitting, are listed in Table 3.2. According to Rietveld refinement, the lattice parameters of rhombohedral Bi at an applied potential of  $-0.28$  V are close to the theoretical ones ( $a = 4.546$  Å and  $c = 11.862$  Å) but slightly lower, indicating possible lattice distortion. For each diffraction pattern, the full width at half maximum (FWHM) intensity of each peak was measured and the crystallite size was determined using the Williamson-Hall plot. At  $-0.28$  V, slightly larger crystallite sizes are obtained for Bi grown on glass/FTO substrate ( $\sim 49$  nm), while smaller crystallite sizes are obtained for that grown on Si/Ti/Au substrate ( $\sim 37$  nm). To evaluate the contribution of the deposition potential on the microstructural features of Bi, XRD of deposits grown on glass/ITO at the three potentials studied in this work was carried out. The obtained diffraction patterns are presented in Figure 3.7b and cell parameters and crystallite sizes listed in Table 3.2.

**Table 3.2 Theoretical (reference code 01-085-1329) and experimental intensity ratios, the latter determined from the XRD patterns shown in Figure 3.7 for Bi deposits obtained on glass/FTO, Si/Ti/Au, and glass/ITO**

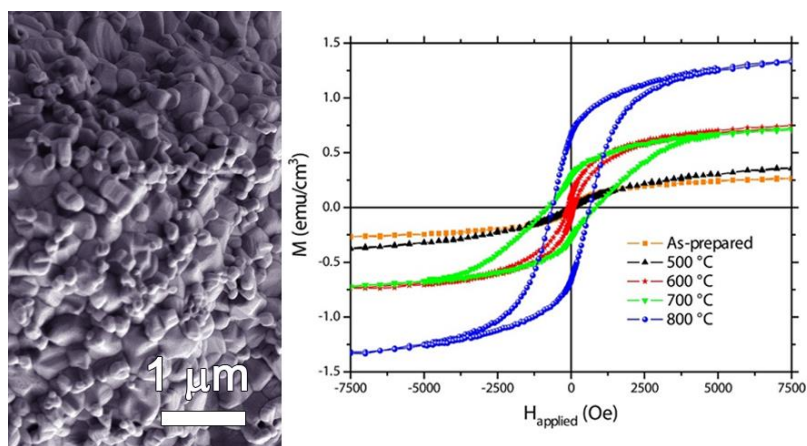
Substrate	Potential (V)	Cell parameter (Å)		Crystallite Size (Å)
		<i>a</i>	<i>c</i>	
glass/FTO	-0.28	4.542	11.849	486±59
Si/Ti/Au	-0.28	4.545	11.849	369±45
glass/ITO	-0.28	4.541	11.850	456±52
glass/ITO	-0.24	4.546	11.861	770±96
glass/ITO	-0.20	4.548	11.861	154±62

According to the  $I_{(hkl)}/I_{(012)}$  ratios (Table 3.1) the more textured Bi grows at  $-0.20$  V. In this case, strongly preferred orientation of (003) planes is readily apparent; this is in agreement with the morphology observed by SEM, where completed and truncated hexagons are observed from the top view; on the opposite way, the intensity of several other reflections, such as the (104), (110), and (202), decreases. This result seems to be in line with the analysis carried out by Sandnes et al. [1] where the reflection of the (003) plane only appears at their lowest applied potential ( $-0.05$  V vs. Ag|AgCl (3 M KCl)). An important reduction on crystallite size is also detected for the particles grown at  $-0.20$  V. It is worth noticing that the cell parameters of the Bi deposited at  $-0.20$  V and  $-0.24$  V are closer to the theoretical values.



### 3.2 Electrodeposition of Bismuth Ferrite followed by Heat Treatment

This work reports the synthesis of  $\text{BiFeO}_3$  films with rhombohedral structure by electrodeposition from a dimethylformamide bath followed by a thermal treatment in air. A detailed structural characterization is carried out in the as-prepared and annealed bismuth ferrite thin films to elucidate the existence of  $\text{BiFeO}_3$  and other secondary binary and ternary oxides. The produced thin films are also studied from a magnetic viewpoint and the eventual contribution from secondary phases to the observed ferromagnetic-like response is discussed (Scheme 3.2).



**Scheme 3.2** On the left, SEM image of the thin film annealed at 600 °C. On the right, hysteresis loops recorded by VSM of the as-prepared and annealed samples

#### 3.2.1 Electrochemical Deposition

Metals and metal matrix/nanoparticle composites have been deposited from N,N-dimethylformamide (DMF) in the past [9,10]. The examples available, although scarce compared to water-based electrolytes, mainly focus on cobalt, nickel and their alloys. Little is known about the electrodeposition of metal oxides from DMF baths. In our laboratory, attempts to produce Bi- and Fe-containing films with  $\text{Bi:Fe} \approx 1$  from aqueous solution (0.045 M  $\text{Fe}(\text{NO}_3)_3 \cdot 9\text{H}_2\text{O}$ , 0.01 M  $\text{Bi}(\text{NO}_3)_3 \cdot 5\text{H}_2\text{O}$  and 0.1 M triethanolamine) failed. In particular, only Bi-rich deposits were obtained at pH 12.5 and  $T = 65$  °C for deposition potentials ranging from  $-0.8$  V to  $-1.5$  V. On the contrary, codeposition of both Bi and Fe elements in comparable amounts was possible from the DMF bath. This is because the deposition potentials in water and DMF media are different.

Fig. 3.8a shows the CV curve recorded from the DMF bath under stagnant conditions. Negative currents were detected from  $+0.25$  V during the cathodic going sweep. Prior to reversing the scan toward anodic potentials, a diffusion-controlled peak was recorded at  $-1.1$  V. Fig. 3.8b shows the  $j-t$  curves recorded between  $-1.25$  V and  $-1.35$  V under stagnant conditions. Whilst less negative currents were observed for an applied potential of  $-1.25$  V during the first 200 s of deposition, fluctuations caused the currents to almost merge afterwards. A similar trend was observed under stirred conditions (see inset of Fig. 3.8b). In this case the  $j-t$  transients



showed even more pronounced fluctuations. Since the currents were similar,  $-1.30$  V was selected for the subsequent growth of  $\text{BiFeO}_3$  films. Fig. 3.8c shows an SEM image of an as-deposited film. A rough morphology consisting of not fully dense nodules was noticed. At a low magnification, the coating displayed a cracked appearance, likely caused by layer dehydration in the SEM vacuum chamber. The presence of small amount of water is unavoidable when using DMF as solvent. These cracks are frequently observed in metal oxides produced by electrodeposition in aqueous solutions [11].

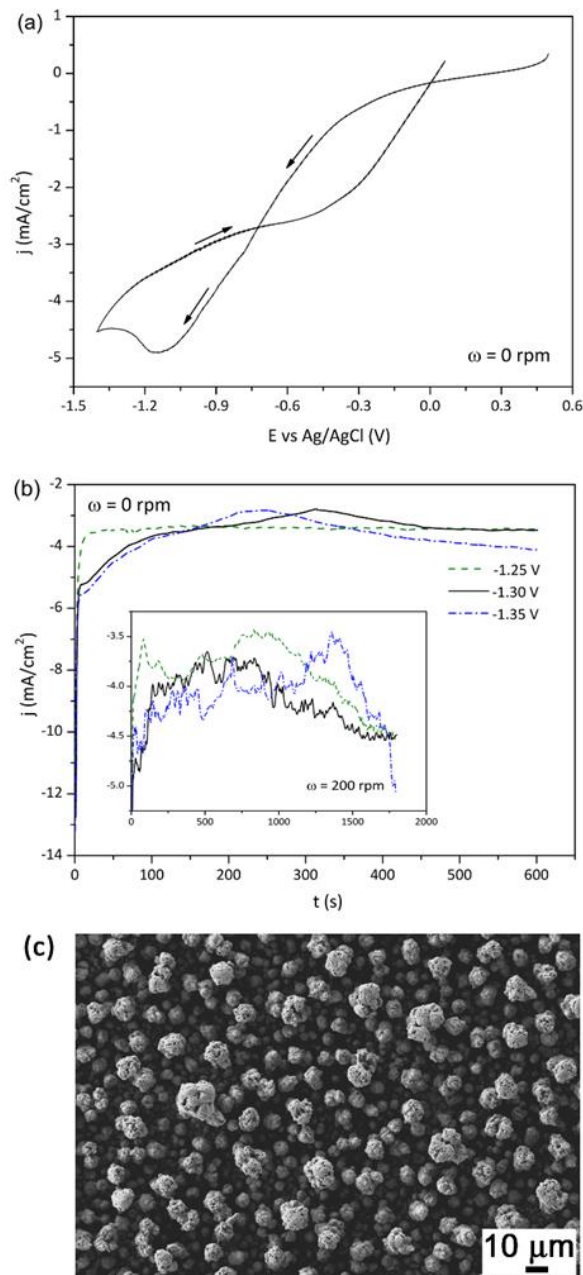


**Figure 3.8** (a) CV curve recorded under quiescent conditions, initially scanning from  $+0.5$  V toward negative potentials, at  $50$  mV  $\text{s}^{-1}$ . (b)  $j$ - $t$  curves recorded under stagnant conditions at  $-1.25$  V,  $-1.30$  V and  $-1.35$  V for  $600$  s. The inset shows the  $j$ - $t$  curves recorded at the same potentials but under stirred conditions ( $\omega = 200$  rpm) for longer deposition time ( $1800$  s). (c) SEM image, taken with secondary electrons, of an as-electrodeposited film at  $-1.30$  V for  $1800$  s

### 3.2.2 Structural and Morphological Characterisation

The XRD pattern of the as-deposited sample (not shown) is consistent with an amorphous-like phase since, besides peaks arising from the substrate, only wide halos are observable. As can be seen in Fig. 3.9, crystallisation takes place upon heat treatment. At 500 °C, rhombohedral BiFeO<sub>3</sub> with a crystallite size of around 42 nm is formed together with Bi<sub>2</sub>O<sub>3</sub>, Fe<sub>2</sub>O<sub>3</sub>, Fe<sub>3</sub>O<sub>4</sub> and ternary oxides, such as Bi<sub>24</sub>Fe<sub>2</sub>O<sub>39</sub> or Bi<sub>2</sub>Fe<sub>4</sub>O<sub>9</sub>. According to the phase diagram [12] the presence of these phases indicates that 500 °C is still a mild condition for the BiFeO<sub>3</sub> formation.

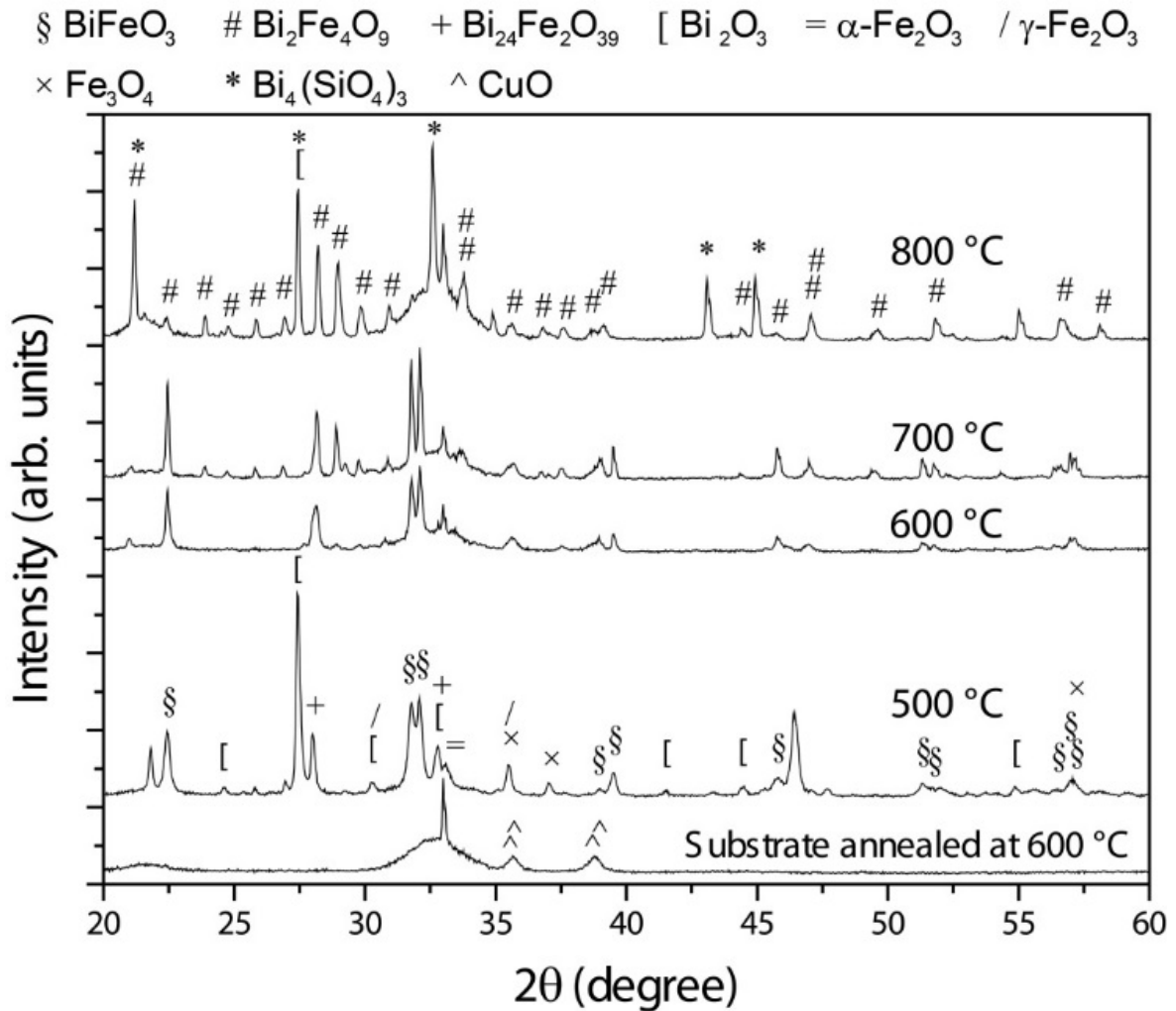


Figure 3.9  $\theta/2\theta$  X-ray diffraction patterns of the samples annealed at 500, 600, 700 and 800 °C. To serve as reference, the pattern of the substrate annealed at 600 °C is also included. The peaks have been labelled according to the existing crystallographic phases (between parentheses, the used symbol to represent the phase together with its ICDD File Card No.): BiFeO<sub>3</sub> (§, 01-072-2321), Bi<sub>2</sub>Fe<sub>4</sub>O<sub>9</sub> (#, 01-072-1832), Bi<sub>24</sub>Fe<sub>2</sub>O<sub>39</sub> (+, 00-042-0201), Bi<sub>2</sub>O<sub>3</sub> ([, 00-045-1344), α-Fe<sub>2</sub>O<sub>3</sub> (=, 01-085-0987), γ-Fe<sub>2</sub>O<sub>3</sub> (/ , 00-039-1346), Fe<sub>3</sub>O<sub>4</sub> (×, 00-001-1111), Bi<sub>4</sub>(SiO<sub>4</sub>)<sub>3</sub> (\*, 01-088-0243) and CuO (^, 00-041-0254)

From a thermodynamic point of view, BiFeO<sub>3</sub> is formed from equal parts of Bi<sub>2</sub>O<sub>3</sub> and Fe<sub>2</sub>O<sub>3</sub>. Upon annealing at 600 °C, the amount of BiFeO<sub>3</sub> further increases in detriment mainly of Bi<sub>2</sub>O<sub>3</sub> and Fe<sub>2</sub>O<sub>3</sub>, becoming nearly the only phase. The crystallite size grows up to around 80 nm, suggesting that ternary phases, which tend to

grow at the grain boundaries of  $\text{BiFeO}_3$ , have strongly vanished, as suggested by the XRD characterisation. The thermal treatment at 700 °C leads to a significant formation of  $\text{Bi}_2\text{Fe}_4\text{O}_9$  at expenses of  $\text{BiFeO}_3$ , which still shows an increased crystallite size (about 146 nm). In turn, the crystallite size of the  $\text{Bi}_2\text{Fe}_4\text{O}_9$  phase is around 100 nm. The relatively large crystallite size of  $\text{BiFeO}_3$  suggests that  $\text{Bi}_2\text{Fe}_4\text{O}_9$  grows in cluster-like form rather than precipitate-like at the grain boundaries of  $\text{BiFeO}_3$ , which would result in a decreased  $\text{BiFeO}_3$  crystallite size. Upon annealing at 800 °C,  $\text{Bi}_2\text{Fe}_4\text{O}_9$  becomes the main phase. In comparison with  $\text{BiFeO}_3$ , this ternary phase is an Fe-rich phase, thus, to keep the stoichiometry, Fe-free phases must be formed. As expected, the XRD pattern of the sample thermally treated at 800 °C shows that  $\text{Bi}_2\text{Fe}_4\text{O}_9$  forms along with  $\text{Bi}_2\text{O}_3$  and  $\text{Bi}_4(\text{SiO}_4)_3$ . At this temperature, the crystallite size of the  $\text{Bi}_2\text{Fe}_4\text{O}_9$  significantly grows, reaching a value above 200 nm, which cannot be estimated by line profile analysis [13]. At the same time, the amount of  $\text{BiFeO}_3$  strongly diminishes and the residual  $\text{BiFeO}_3$  is highly nanostructured as evidenced by its weak and broad XRD peaks, respectively (note that the  $\text{BiFeO}_3$  peaks located at 31.8 and 32.1 degrees nearly vanish upon annealing at 800 °C).

The film annealed at 700 °C was investigated by TEM (Fig. 3.10). The occurrence of both  $\text{Bi}_2\text{Fe}_4\text{O}_9$  and  $\text{BiFeO}_3$  phases was seen in the Fast Fourier Transform (FFT) patterns taken on different areas of the sample, in agreement with XRD results.

As aforementioned, the as-prepared sample is not fully dense. Moreover, the film is very rough (Fig. 3.8c). Even though the thermal treatment at 500 °C leads to a somewhat denser film, the ‘open’ structure remains (Fig. 3.11a). It is at 600 °C where the morphology starts to evolve towards more particulate-like, although some voids are still preserved. The particles adopt prism morphologies, indicating the formation of rhombohedral  $\text{BiFeO}_3$  (Fig. 3.11b). This is in concordance with the XRD analysis, which reveals that 500 °C is still a mild condition for the formation of  $\text{BiFeO}_3$ . With further increase of the annealing temperature (i.e., 700 °C), the size of the particles slightly increases and the prism morphology becomes more well-defined (Fig. 3.11c). At 800 °C, even though the prism morphology remains, a significant particle coarsening occurs, resulting in a significant increase of the size of the particles. This is in agreement with the structural analysis which indicates that the crystallite size of the  $\text{Bi}_2\text{Fe}_4\text{O}_9$  phase increases upon annealing at 800 °C up to values that cannot even be estimated by Rietveld refinement.

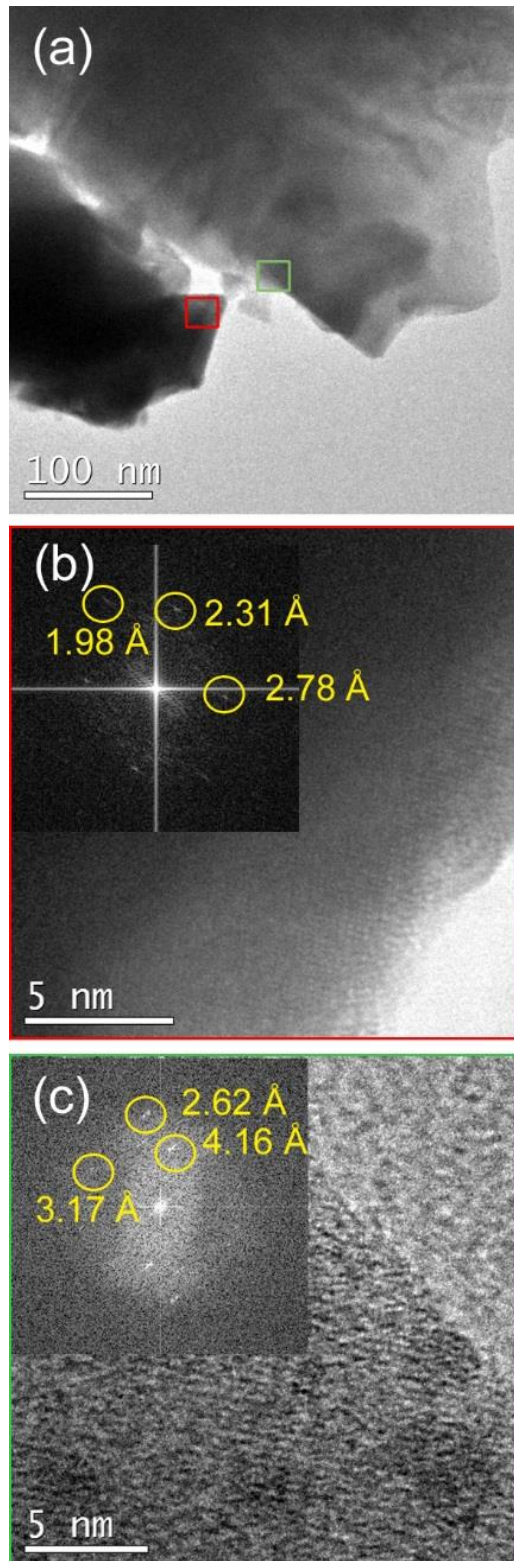


Figure 3.10 (a) TEM image of a representative zone of the sample annealed at 700 °C. (b) HRTEM image of the red square depicted in panel (a). The inset corresponds to its FFT. The interplanar distances are characteristic of  $\text{Bi}_2\text{Fe}_4\text{O}_9$ . (c) HRTEM image of the green square illustrated in panel (a). The inset corresponds to its FFT and the interplanar distances belong to  $\text{BiFeO}_3$  phase

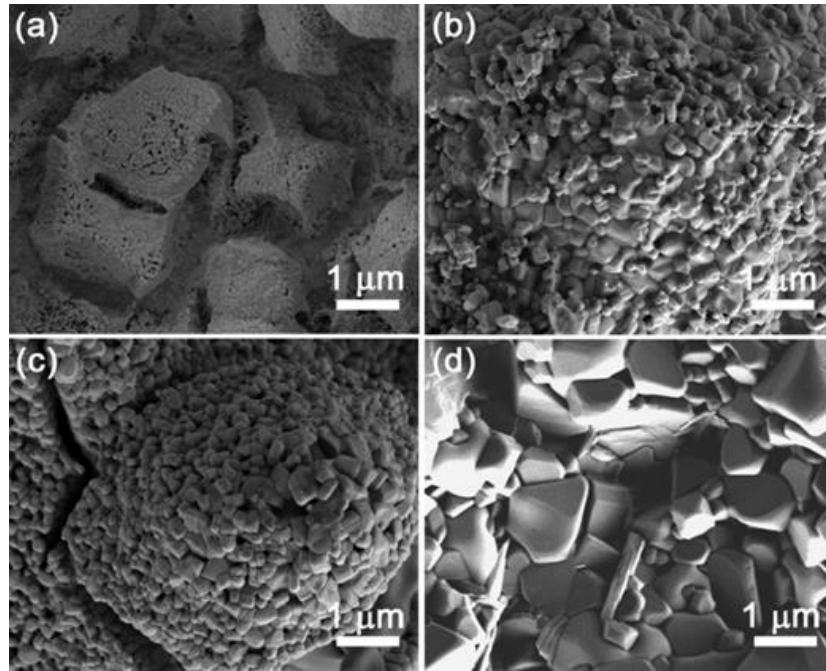


Figure 3.11 SEM images, taken with secondary electrons, of the samples annealed at (a) 500, (b) 600, (c) 700 and (d) 800 °C

### 3.2.3 Magnetic Characterisation

Magnetisation ( $M$ ) vs. applied magnetic field ( $H_{\text{applied}}$ ) curves (i.e., hysteresis loops) are shown in Fig. 3.12. The as-prepared sample already exhibits traces of ferromagnetism which might be ascribed to Fe-rich areas in the amorphous oxide films.

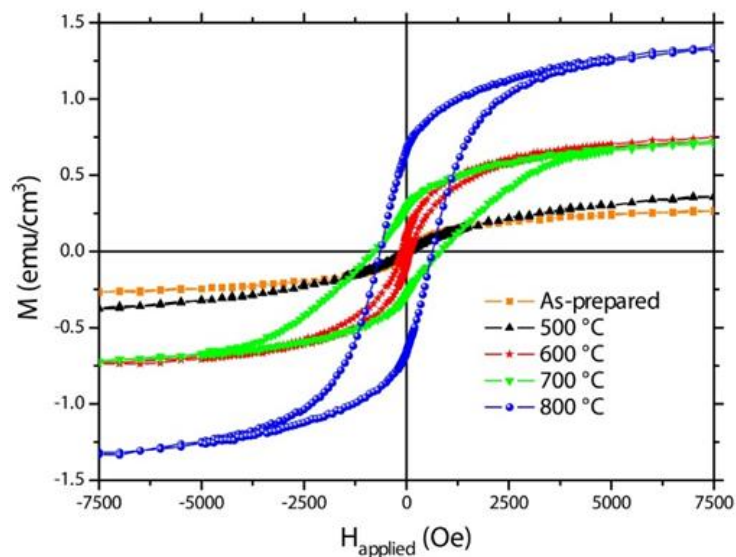


Figure 3.12 Hysteresis loops recorded by vibrating sample magnetometry of the as-prepared sample and the samples annealed at 500, 600, 700 and 800 °C

Crystallisation takes place upon heat treatment. Annealing at 500 °C results in a slightly increased saturation magnetization, which might be ascribed to the residual formation of iron oxides (see Fig. 3.12 and Table 3.3).

At room temperature,  $\alpha$ -Fe<sub>2</sub>O<sub>3</sub> shows weak ferromagnetic-like behaviour due to its nanoscale nature [14,15] and Fe<sub>3</sub>O<sub>4</sub> and  $\gamma$ -Fe<sub>2</sub>O<sub>3</sub> are ferromagnetic [16]. On top of this, BiFeO<sub>3</sub> may also contribute to ferromagnetism due to size effects, which result in antiferromagnetic spin canting, due to the suppression of the spiral spin structure [17-20]. From a magnetic point of view, the ternary phases play a minor role since they are usually paramagnetic at room temperature [21,22]. For instance, Bi<sub>2</sub>Fe<sub>4</sub>O<sub>9</sub> becomes antiferromagnetic but only below 250 K [16]. At 600 °C, the saturation magnetisation significantly increases. From the structural and morphological analyses, this is accompanied with the formation of a nearly pure BiFeO<sub>3</sub> in detriment of both Fe-based oxides and ternary phases (Fig. 3.9). Therefore, the observed ferromagnetic response could be primarily ascribed to nanostructuring effects which reinforce antiferromagnetic spin canting, giving rise to a larger net magnetisation. While the sample annealed at 700 °C shows a similar M<sub>S</sub> than that of the sample annealed at 600 °C (Table 3.3), the saturation magnetisation of the sample annealed at 800 °C is considerably larger. The pronounced decomposition of BiFeO<sub>3</sub> upon annealing at 800 °C yields a highly nanostructured phase with strong size effects which might be responsible for the increase in M<sub>S</sub>. Taking into account the described structural changes with temperature, the increase in H<sub>C</sub> upon annealing at 700 °C and 800 °C might also be related to the formation of Bi<sub>2</sub>Fe<sub>4</sub>O<sub>9</sub> and the other paramagnetic phases, which probably tends to isolate the BiFeO<sub>3</sub> grains, thus decreasing intergranular dipolar and exchange interactions, both of which are known to be detrimental for coercivity [23].

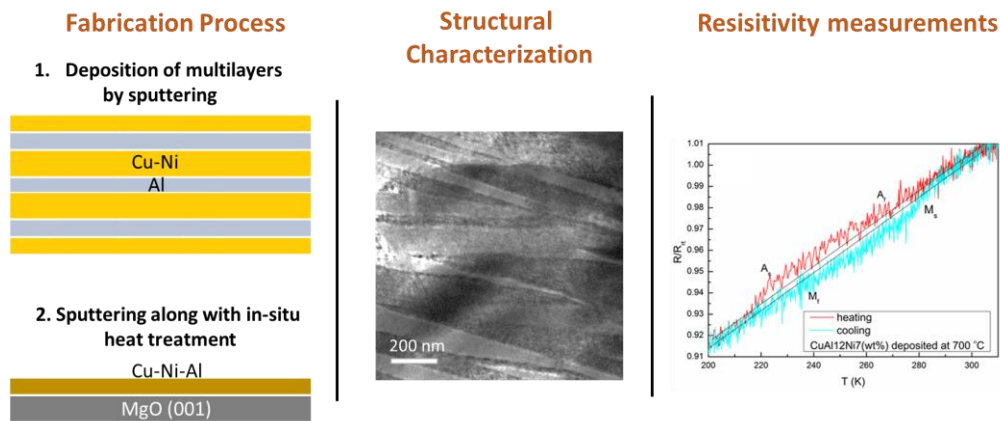
**Table 3.3 Saturation magnetization, M<sub>S</sub>, coercivity, H<sub>C</sub> and remanence-to-saturation magnetization ratio, M<sub>R</sub>/M<sub>S</sub>, of the hysteresis loops presented in Fig. 3.12, which correspond to the as-prepared sample and the samples annealed at 500, 600, 700 and 800 °C**

<b>Sample</b>	<b>M<sub>S</sub> (emu/cm<sup>3</sup>)</b>	<b>H<sub>C</sub> (Oe)</b>	<b>M<sub>R</sub>/M<sub>S</sub> (%)</b>
<b>As-prepared</b>	0.275	< 40	< 2.5
<b>500 °C</b>	0.390	< 40	< 2.5
<b>600 °C</b>	0.770	85	11.0
<b>700 °C</b>	0.745	822	38.3
<b>800 °C</b>	1.360	640	48.9



### 3.3 Sputter Deposited Cu–Al–Ni Shape Memory Thin Films

In this work two different approaches were followed to obtain Cu–Al–Ni thin films with shape memory potential. On the one hand, Cu–Ni/Al multilayers were grown by magnetron sputtering at room temperature. To promote diffusion and martensitic/austenitic phase transformation, the multilayers were subjected to subsequent heat treatment at 700 °C and quenched in iced-water. On the other hand, Cu, Al and Ni were co-sputtered onto heated MgO (001) substrates, held at 700 °C. In the following sections, the crystallographic differences among the films obtained by the two different approaches will be discussed in detail. Resistance versus temperature measurements will be carried out to investigate the shape memory behaviour of the austenitic Cu–12Al–7Ni (wt%) thin films.



**Scheme 3.3** Graphical abstract of the two approaches followed to fabricate the Cu–Al–Ni thin films along with a TEM image of the martensitic Cu–Al–Ni and a resistance vs. temperature curve

#### 3.3.1 X-ray Diffraction Analysis

The XRD patterns of the thin film synthesized either by multilayer deposition and post heat treatment or by simultaneous co-sputtering with in-situ heat treatment are shown in Figure 3.13. Among the free-standing thin films produced by multilayer deposition, Cu–14Al–4Ni (wt%) (Figure 3.13a) shows a mixture of  $\beta'$  martensite and pure Cu.  $\beta'$  martensite has a monoclinic structure (space group Cmcm) whereas Cu has a cubic Fm-3m lattice. As the content of Ni increases and the content of Al decreases (i.e. Cu–13Al–5Ni (wt%)) traces of  $\beta$  austenite (space group Fm-3m) and  $\text{Cu}_9\text{Al}_4$  (space group P-43m) along with  $\beta'$  martensite are detected (Figure 3.13b). However, only  $\beta$  austenite was detected in the XRD pattern of Cu–12Al–7Ni (wt%) free-standing thin film (Figure 3.13c). In turn, the XRD pattern of the thin film co-sputtered at high temperature consists of textured  $\beta$  austenite (Figure 3.13d). Previous studies on Cu–Al–Ni bulk shape memory alloys have reported that a slight change in the composition results in a shift in transformation temperatures [24–26]. Namely, in the studies carried out by Recarté et al. in a Cu–Al–Ni alloy, it was revealed that, for a fixed aluminium content of 13.2 wt%, a decrease in nickel from 5 wt% to 3.5 wt% raised the austenite finish temperature from 10 °C to 80 °C [24]. Agafonov et al. showed that Al content varying from 14.98 wt% to 13.03 wt% caused a change in the

room temperature phase from austenite to martensite for samples synthesized by casting and quenching into water [26]. Same trends were observed by Suresh and Ramamurty [25], where, at room temperature, Cu–13.4Al–4Ni wt.% alloy is in martensite state whereas Cu–14.1Al–4Ni alloy is in austenite state. While in our work we observed that a change in Ni content follows the same trend in the transformation temperatures as the results reported by Recarté et al. [24], the opposite tendency than that reported on [24,25] was observed when modifying the aluminium content. This may be explained because in our case we were modifying Ni and Al content at the same time; consequently, our transformation temperatures have the influence of both, Al and Ni.

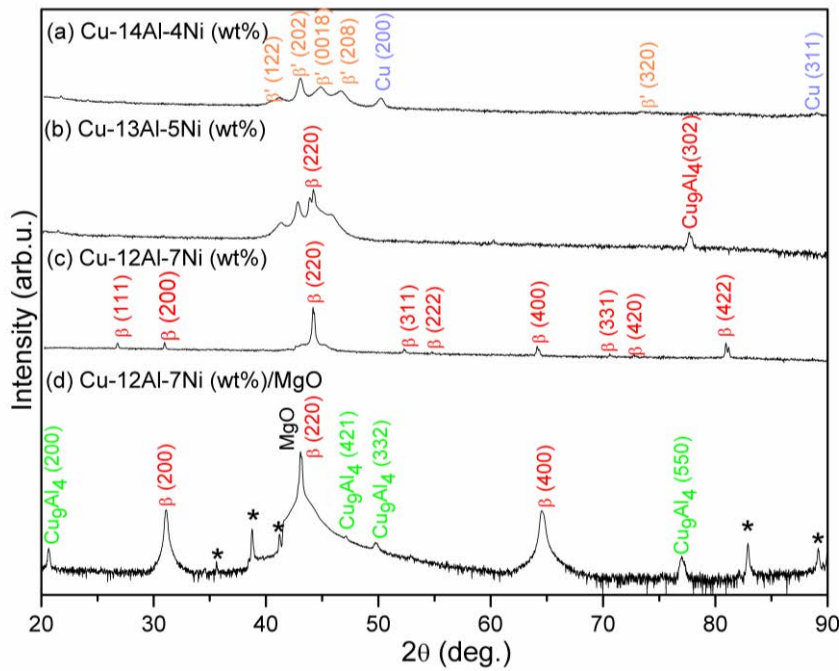


**Figure 3.13** XRD patterns of the sputtered Cu–Al–Ni thin films. (a) Cu–14Al–4Ni (wt%), (b) Cu–13Al–5Ni (wt%), (c) Cu–12Al–7Ni (wt%) films obtained by sputter deposition and subsequent heat treatment and (d) Cu–12Al–7Ni (wt%) film prepared on MgO substrate at 700 °C. (\*) peaks belong to  $K_{\beta}$

In the sample grown on MgO, a thin film with a Cu-12Al-7Ni (wt%) composition on MgO(001) substrate was implemented. Epitaxial relationship MgO(001)[100]/Cu–Al–Ni(001)[110] was induced. The film grows with 45° in plane rotation on the cubic cell of the substrate. Lattice mismatch ( $f$ ) between the cubic lattices is shown in Equation 3.1:

$$f = (\sqrt{2}a_{MgO} - a_{CuAlNi \beta}) / a_{CuAlNi \beta} \quad \text{Equation 3.1}$$

where  $a_{MgO} = 4.212 \text{ \AA}$ ,  $a_{Cu-Al-Ni \beta} = 5.836 \text{ \AA}$

The lattice mismatch between the film and the substrate is  $f = 2\%$ , which is small enough to favour epitaxy. The epitaxially grown sample at 700 °C exhibits preferential (100) orientation. This shows up as strong (200) and (400) peaks in the XRD pattern (Figure 3.13d). Peaks belonging to  $Cu_9Al_4$  phase (i.e. (200), (421), (332), (550) planes) are also present in the pattern. The phi scan carried out for the (220) peak of the film grown on MgO at 700 °C confirmed that the film rotated 45° relative to the substrate (Figure 3.14).



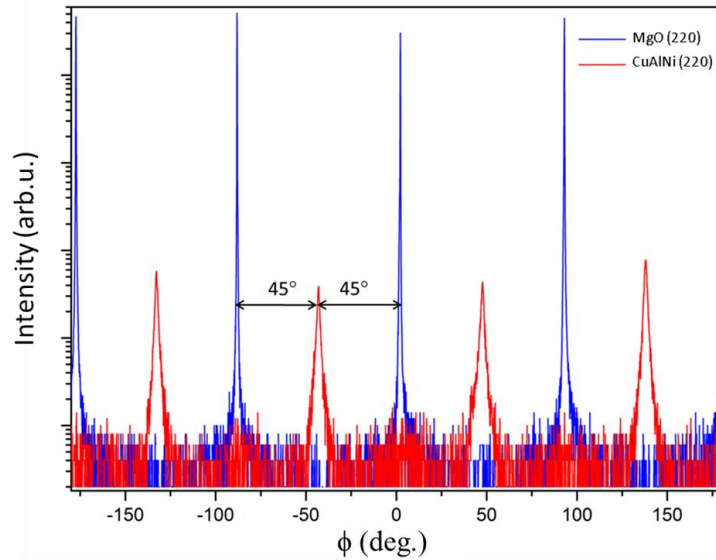


Figure 3.14 Phi scan for (220) peak of  $\beta$ -Cu-Al-Ni film deposited at 700 °C

### 3.3.2 Transmission Electron Microscopy Studies

For the free-standing thin films produced by multilayer deposition, further evidence that the compositional change, from Cu-14Al-4Ni (wt%) to Cu-12Al-7Ni (wt%), results in a shift from martensite to austenite was observed by TEM (Fig. 3.15).

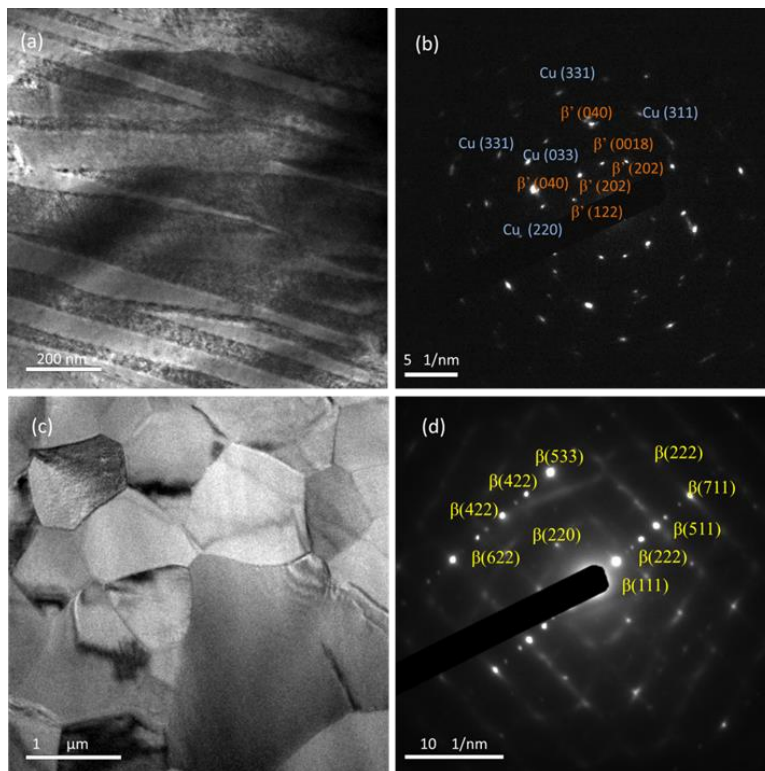


Figure 3.15 (a) TEM image of Cu-14Al-4Ni (wt%) thin film, (b) SAED pattern of (a), (c) TEM image of Cu-12Al-7Ni (wt%) thin film, (d) SAED pattern of (c)

Figure 3.15a and 3.15c belong to TEM images of Cu–14Al–4Ni (wt%) and Cu–12Al–7Ni (wt%) thin films, respectively. Typical martensitic plates are encountered in Cu–14Al–4Ni while a regular polycrystalline structure can be observed in the Cu–12Al–7Ni (wt.%) alloy. The SAED pattern from Cu–14Al–4Ni (wt.%) thin film consists of diffraction spots that belong to  $\beta'$  martensite corresponding to the (040), (202), (0018), (202) and (122) planes and to fcc Cu (i.e. (220), (311), (311), (033) planes). The SAED pattern of the Cu–12Al–7Ni (wt%) thin film consists of diffraction spots characteristics of the austenitic phase ( $\beta$ ) involving (111), (511), (711), (622), (422) and (533) planes. In Figure 3.16a, a high resolution TEM image of the Cu–12Al–7Ni (wt%) thin film grown in MgO is shown. From the FFT (Fast Fourier Transform) pattern of the selected zone in Figure 3.16a, an interplanar distance value of 2.07 Å, which belongs to  $\beta$  austenite (220) as well as a distance of 2.93 Å, which belongs to  $\beta$  austenite (200), can be observed (Figure 3.16b).

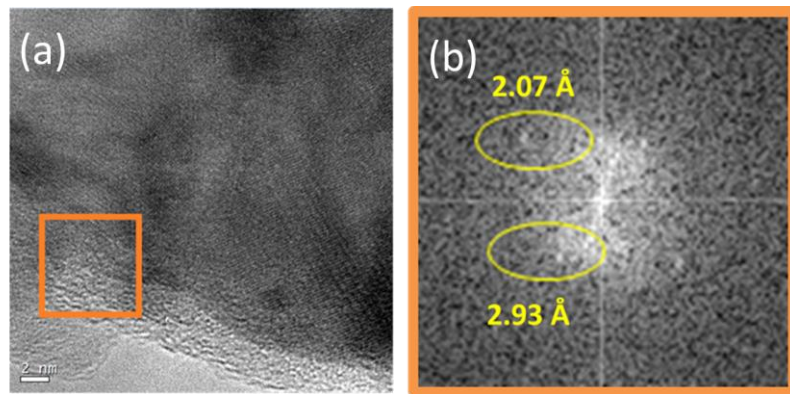
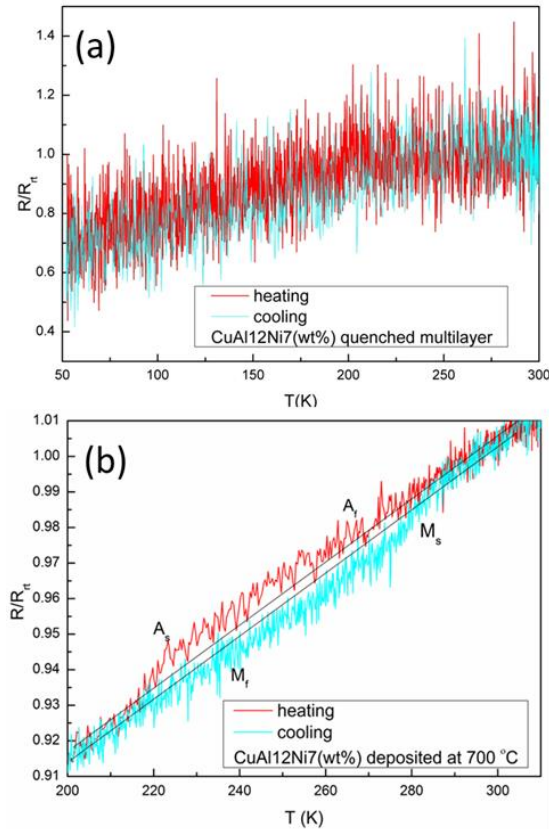


Figure 3.16 (a) HRTEM image of Cu–12Al–7Ni (wt%) thin film grown on MgO. (b) FFT of the selected zone (orange square) in (a)

### 3.3.3 Resistance vs Temperature Measurements

In order to identify the transformation temperatures, resistance measurements as a function of temperature were carried out for both the quenched multilayered sample with the composition Cu–12Al–7Ni (wt%) and the sample with the same composition grown on MgO substrate. Martensitic transformation was not observed in the quenched multilayered Cu–12Al–7Ni (wt%) (Figure 3.17a) whereas a trend that might be indicative of hysteresis formation was encountered for the epitaxially grown Cu–12Al–7Ni (wt%) sample (Figure 3.17b). The reason behind the fact that a transformation is observed in the epitaxially grown (200) textured austenite thin film whereas no change was seen in the randomly oriented polycrystalline one, might be attributed to size effects. Size effects such as the volume of the material or structural components including precipitate particles and grains in polycrystals have a huge influence on the martensitic phase transformation [27]. Decreasing grain size and decreasing twin separation cause an increase in strain energy and twin interfacial energy which, in turn, increases the energy barrier [28]. For instance, Shi et al. [29] showed that for submicrometric NiTi particles (below 100 nm), the martensitic transformation was fully suppressed. Similarly, in this work, in the randomly oriented polycrystalline austenitic Cu–12Al–7Ni (wt%) film, with a crystallite size of 95 nm according to Scherrer's formula, no transformation was observed. It has been indicated by Chen and Schuh

[30] that as  $d(\text{grain size})/D(\text{sample thickness})$  decreases, the energy barrier for transformation increases. The interfacial energies depend on grain boundary attained by martensite plates, the interfaces between austenite and martensite plates, and the twin interfaces within martensite plates [31].



**Figure 3.17 Resistance vs. temperature measurement of the Cu-12Al-7Ni (wt%) prepared by (a) heat treatment after sputtering and (b) in-situ heat treatment**

Additionally, previous studies demonstrate that decreasing film thickness is also a reason for suppression of martensitic phase transformation. Wan and Komvopoulos [32] showed that for sputtered NiTi films with a thickness less than 100 nm no martensitic transformation was observed. In the case of sputtered polycrystalline Cu–Al–Ni films, transformation temperatures for films with 2  $\mu\text{m}$  thickness were reported by Moran and his co-workers [31]. To the best of our knowledge, these are the sputtered Cu–Al–Ni films with the lowest thickness values reported in the literature. Torres et al. [33] also observed martensitic transformation for 5  $\mu\text{m}$  thick films. On the opposite, no transformation was observed in the polycrystalline 1.25  $\mu\text{m}$  Cu–12Al–7Ni (wt%) sample prepared in this work by post-treatment of the multilayers.

The absence of phase transformation at low deposition temperatures could be attributed to, on one side, to the small grain sizes causing higher number of grain boundary interfaces and associated excess free volume and, on the other side, to the thinner nature of the sample as pointed out by Wan and Komvopoulos [32].

## References

- [1] Sandnes, E., Williams, M. E., Bertocci, U., Vaudin, M. D., Stafford, G. R. Electrodeposition of Bismuth from Nitric Acid Electrolyte. *Electrochimica Acta*, 52 (2007), 6221–6228.
- [2] Frutos, A. A., Sala, L. F., Escandar, G. M., Devillers, M., Salas Peregrin, J. M., Gonzalez Sierra, M. Bismuth ( III ) Complexes of d–Gluconic Acid. *Studies in Aqueous Solution and in the Solid Phase. Polyhedron*, 18 (1999), 989–994.
- [3] Zhang, Z., Gibson, P., Clark, S. B., Tian, G., Zanonato, P. L., Rao, L. Lactonization and Protonation of Gluconic Acid: A Thermodynamic and Kinetic Study by Potentiometry, NMR and ESI-MS. *Journal of Solution Chemistry*, 36 (2007), 1187–1200.
- [4] Senthilkumar, M., Mathiyarasu, J., Joseph, J., Phani, K. L. N., Yegnaraman, V. Electrochemical Instability of Indium Tin Oxide (ITO) Glass in Acidic pH Range during Cathodic Polarization. *Materials Chemistry and Physics*, 108 (2008), 403–407.
- [5] Takeno, N. Atlas of Eh-pH Diagrams Intercomparison of Thermodynamic Databases. National Institute of Advanced Industrial Science and Technology. Tokyo. 2005.
- [6] Bretti, C., Cigala, R. M., De Stefano, C., Lando, G., Sammartano, S. Acid–Base and Thermodynamic Properties of d-Gluconic Acid and Its Interaction with Sn<sup>2+</sup> and Zn<sup>2+</sup>. *Journal of Chemical and Engineering Data*, 61 (2016), 2040–2051.
- [7] Das, A., Sangaranarayanan, M. V. Shape–Controlled Synthesis of Three–Dimensional Triangular Bismuth Microstructures and Sensing of H<sub>2</sub>O<sub>2</sub>. *CrystEngComm*, 18 (2016), 1147–1155.
- [8] Guo, L., Oskam, G., Radisic, A., Hoffmann, P. M., Searson, P. C. Island Growth in Electrodeposition. *Journal of Physics D: Applied Physics*, 44 (2011), 443001.
- [9] Cui, C. Q., Jiang, S. P., Tseung, A. C. C. Mechanism of the Electrodeposition of Cobalt (II) Chloride in N,N-Dimethylformamide (DMF) Solution. *Journal of the Electrochemical Society*, 138 (1991), 94–100.
- [10] Tripathi, M.K., Singh, D.K., Singh, V.B. Microstructure and Properties of Electrochemically Deposited Ni-Fe/Si<sub>3</sub>N<sub>4</sub> Nanocomposites from a DMF Bath. *Journal of the Electrochemical Society*, 162 (2015), D87–D95.
- [11] Quintana, A., Varea, A., Guerrero, M., Suriñach, S., Baró, M. D., Sort, J., Pellicer, E. Structurally and Mechanically Tunable Molybdenum Oxide Films and Patterned Submicrometer Structures by Electrodeposition. *Electrochimica Acta*, 173 (2015), 705–714.
- [12] Catalan, G., Scott, J. F. Physics and Applications of Bismuth Ferrite. *Advanced Materials*, 21 (2009), 2463–2485.
- [13] Cullity, B. D. Elements of X-ray Diffraction (Second Edition) Addison-Wesley Publishing. Massachusetts. 1956.
- [14] Sun, Z., Yuan, H., Liu, Z., Han, B., Zhang, X. A Highly Efficient Chemical Sensor Material for H<sub>2</sub>S:  $\alpha$ -Fe<sub>2</sub>O<sub>3</sub> Nanotubes Fabricated Using Carbon Nanotube Templates. *Advanced Materials*, 17 (2005), 2993–2997.
- [15] Sakurai, S., Namai, A., Hashimoto, K., Ohkoshi, S. First Observation of Phase Transformation of All Four Fe<sub>2</sub>O<sub>3</sub> phases ( $\gamma \rightarrow \epsilon \rightarrow \beta \rightarrow \alpha$ -phase). *Journal of the American Chemical Society*, 131 (2009), 18299–303.
- [16] Masrour, R., Hlil, E. K., Hamedoun, M., Benyoussef, A., Mounkachi, O., El Moussaoui, H. Electronic and Magnetic Structures of Ferrimagnetic Mn<sub>2</sub>Sb Compound. *Journal of Magnetism and Magnetic Materials*, 374 (2015), 116–119.

- [17] Ramazanoglu, M., Laver, M., Ratcliff, W., Watson, S. M., Chen, W. C., Jackson, A., Kothpalli, K., Lee, S., Cheong, S. W., Kiryukhin, V. Local Weak Ferromagnetism in Single-Crystalline Ferroelectric BiFeO<sub>3</sub>. *Physical Review Letters*, 107 (2011), 1–5.
- [18] Huang, F., Wang, Z., Lu, X., Zhang, J., Min, K., Lin, W., Ti, R., Xu, T., He, J., Chen, Y., Zhu, J. Peculiar Magnetism of BiFeO<sub>3</sub> Nanoparticles with Size Approaching the Period of the Spiral Spin Structure. *Scientific Reports*, 3 (2013), 1–7.
- [19] Bèa, H., Bibes, M., Petit, S., Kreisel, J., Barthèlèmy, A. Structural Distortion and Magnetism of BiFeO<sub>3</sub> Epitaxial Thin Films: A Raman Spectroscopy and Neutron Diffraction Study. *Philosophical Magazine Letters*, 87 (2007), 165–174.
- [20] Modarresi, H., Lazenka, V., Menéndez, E., Lorenz, M., Bisht, M., Volodin, A., Van Haesendonck, C., Grundmann, M., Van Bael, M. J., Ternst, K., Vantomme, A. Induced Ferromagnetism and Magnetoelectric Coupling in Ion-Beam Synthesized BiFeO<sub>3</sub>-CoFe<sub>2</sub>O<sub>4</sub> Nanocomposite Thin Films. *Journal of Physics D*, 49 (2006), 325302.
- [21] Zatsiupa, A. A., Bashkirov, L. A., Troyanchuk, I. O., Petrov, G. S., Galyas, A. I., Lobanovskii, L. S., Trukhanov, S. V., Sirota, I. M. Magnetization, Magnetic Susceptibility, and Effective Magnetic Moment of the Fe<sup>3+</sup> Ions in Bi<sub>2</sub>Fe<sub>4</sub>O<sub>9</sub>. *Inorganic Materials*, 49 (2013), 616–620.
- [22] Irshad, Z., Shah, S. H., Rafiq, M. A., Hasan, M. M. First Principles Study of Structural, Electronic and Magnetic Properties of Ferromagnetic Bi<sub>2</sub>Fe<sub>4</sub>O<sub>9</sub>. *Journal of Alloys and Compounds*, 624 (2015), 131–136.
- [23] Skomski, R., Coey J. M. D. *Permanent Magnetism*. Institute of Physics Publishing. Bristol and Philadelphia. 1999.
- [24] Recarte, V., Pérez-Sáez, R. B., San Juan, J., Bocanegra, E. H., Nó, M. L. Influence of Al and Ni Concentration on the Martensitic Transformation in Cu-Al-Ni Shape-Memory Alloys. *Metallurgical and Materials Transactions A*, 33 (2002), 2581–2591.
- [25] Suresh, N., Ramamurty, U. Aging Response and Its Effect on the Functional Properties of Cu-Al-Ni Shape Memory Alloys. *Journal of Alloys and Compounds*, 449 (2008), 113–118.
- [26] Agafonov, V., Naudot, P., Dubertret, B., Dubois, A., Influence of the Aluminium Content on the Appearance and Stability of Martensites in the Cu-Al-Ni System, *Scripta Metallurgica*, 22 (1988), 489–494.
- [27] Malygin, G. A. Nanoscopic Size Effects on Martensitic Transformations in Shape Memory Alloys. *Physics of the Solid State*, 50 (2008), 1538–1543.
- [28] Waitz, T., Karnthaler, H. P. Martensitic Transformation of NiTi Nanocrystals Embedded in an Amorphous Matrix. *Acta Materialia*, 52 (2004), 5461–5469.
- [29] Shi, X., Cui, L., Jiang, D., Yu, C., Guo, F., Yu, M., Liu, Y. Grain Size Effect on the R-phase Transformation of Nanocrystalline NiTi Shape Memory Alloys. *Journal of Materials Science*, 49 (2014), 4643–4647.
- [30] Chen, Y., Schuh, C. A. Size Effects in Shape Memory Alloy Microwires. *Acta Materialia*, 59 (2011), 537–553.
- [31] Morán, M. J., Condó, A. M., Soldera, F., Sirena, M., Haberkorn, N. Martensitic Transformation in Freestanding and Supported Cu-Al-Ni Thin Films Obtained at Low Deposition Temperatures. *Materials Letters*, 184 (2016), 177–180.
- [32] Wan, D., Komvopoulos, K. Thickness Effect on Thermally Induced Phase Transformations in Sputtered Titanium-Nickel Shape-Memory Films. *Journal of Materials Research*, 20 (2005), 1606–1612.
- [33] Torres, C. E., Condó, A. M., Haberkorn, N., Zelaya, E., Schryvers, D., Guimpel, J., Lovey, F. C. Structures in Textured Cu-Al-Ni Shape Memory Thin Films Grown by Sputtering. *Materials Characterization*, 96 (2014), 256–262.

## 4. General Conclusions

1. Finely-distributed micrometer- and submicrometer-sized Bi particles were obtained by electrodeposition from an aqueous solution containing nitric acid and sodium gluconate. A narrow window of deposition potentials and relatively short deposition time (250 s) to prevent the material from detachment was examined.
2. The substrate type (metallic vs. oxide) greatly impacted both the shape and the size of the particles obtained at each applied potential. Differences in substrate conductivity likely play a key role in Bi particles' shape. A transition from polyhedral-shaped particles, including hexagons towards dendrites, was most clearly observed on glass/ITO.
3. Rhombohedral Bi with (003) predominant orientation and crystallite size below 50 nm was obtained at  $-0.28$  V vs. Ag|AgCl on all electrodes.
4. The (003) orientation further increased when completed and truncated hexagons formed on the substrate, as was the case for the glass/ITO electrode.
5. The synthesis of bismuth ferrite ( $\text{BiFeO}_3$ ) has been successfully carried out by potentiostatic electrodeposition from a nitrate-based DMF bath followed by heat treatment in air.
6. Since the electrodeposition results in amorphous-like films, thermal treatments are needed to induce crystallisation. Annealing procedures in air at 500, 600, 700 and 800 °C for 2 hours were carried out. The heat treatment at 600°C results in nearly pure nanostructured  $\text{BiFeO}_3$  with soft ferromagnetic-like properties. A detailed structural, morphological and magnetic characterisation as a function of annealing temperature evidences that  $\text{BiFeO}_3$  forms in a narrow temperature window.
7. The observed ferromagnetism in the obtained films is mainly ascribed to nanostructuring and is also sensitive to the presence of secondary phases, such as Bi–Fe–O ternary phases or iron oxides.
8. Cu–Al–Ni films with shape memory potential were synthesized by both sputter deposition followed by heat treatment and sputter deposition along with in-situ heat treatment.
9. A transition from martensite to austenite was observed in samples prepared by sputtering followed by heat treatment as the Ni content of the composition increased and the Al content decreased.

10. Preferential growth along (100) direction of film on MgO was observed in Cu–12Al–7Ni (wt%) due to epitaxial relationship MgO(001)[100]/Cu–Al–Ni(001)[110] at synthesis of the film at 700 °C.
  
11. Resistance change with respect to temperature was observed in the highly preferentially oriented grown austenitic Cu–12Al–7Ni (wt%) film whereas martensitic transformation was completely suppressed in the polycrystalline austenitic sample with the same composition.

## **5. Future Perspectives**

Within the scope of this Thesis, electrodeposition and sputter deposition were used in the fabrication of sustainable materials. The electrochemical behaviour of the eco-friendly semi-metal bismuth was investigated and as a bismuth based compound, electrodeposition of bismuth ferrite was carried out. As a substitute candidate for Ni–Ti shape memory alloys with 55% Ni, Cu–Al–Ni shape memory system, which has 4-7 wt% Ni, was studied as a more sustainable alternative with low nickel content. Morphological, structural, magnetic and electrical properties of the deposited films were investigated by using necessary characterization techniques. The synthesized films have the potential to be adapted in MEMS platforms. The approaches that can be followed in the next steps are mentioned below:

For surface sensitive applications such as heterogeneous catalysis, gas storage and sensing, the submicron and nanosized particles of electrodeposited bismuth could be used as they possess a larger surface-to-volume ratio compared to compact films. On the other hand, in order to move towards obtaining full coverage of bismuth films on the substrate, variations in the electrolyte composition and deposition conditions could be applied.

By focusing on making variations in the bath composition and heat treatment parameters such as time, temperature and vacuum conditions, obtaining bismuth ferrite films with higher purity could be expected. It is envisaged that the electrodeposition of  $\text{BiFeO}_3$  in the form of films with increased surface area would emerge as a subject of interest that would pave the way for both new fundamental physics and spintronic device applications.

In order to investigate the size effects in Cu–Al–Ni shape memory thin films further, sputter deposition of Cu–Al–Ni austenite films on MgO substrates at high temperature with different micrometer-level thicknesses and nanopillars followed by electrical resistance measurements to characterize shape memory behaviour would enhance the present work carried out. Also, mechanical characterization would also provide further insight on the size effects for this alloy system. These steps would prepare the background to design the potential for the use of Cu–Al–Ni shape memory thin films in microactuator applications.

Keeping sustainability on board while pursuing miniaturization in device materials is the concept that will shape the future in the MEMS world. That's why; starting from precursor selection, in all steps of material production, environmental, social and economic aspects of the process should be taken into consideration.





## Scientific CV



**Address** : Campus Universitat Autònoma de Barcelona, Vila Universitaria, Block R, R009, 08193, Bellaterra, Barcelona, Spain.

**e-mail** : doga.bilican@uab.cat, bilican.doga@gmail.com

**Name** : Doğa Bilican **Birth Date** : 26.06.1990

**Marital Status** : Single **Birth Place** : Istanbul, Turkey

**Nationality** : Turkish Republic

### Present Professional Activities

**Ph.D. Student**  
**2015-2018 (expected)**

**Autonomous University of Barcelona, Barcelona, Spain**  
**Materials Science Department**

Supervisors: Prof. Jordi Sort, Dr. Eva Pellicer, Dr. Jordina Fornell  
The Ph.D. is carried out within the framework of a Marie Skłodowska Curie Action named SELECTA-ITN (Smart Electrodeposited Alloys Innovative Training Network). The project (H2020-MSCA-ITN-2014 no. 642642) deals with the development of environmentally sustainable materials to be utilized in magnetic and mechanical applications by electrodeposition of bismuth, electrodeposition of bismuth ferrite, synthesis of Cu-Al-Ni shape memory alloys, effects of post- and in-situ heat treatment methods in obtaining shape memory properties.

### Academic Background

**M.Sc. Degree**  
**2013-2015**

**Istanbul Technical University, Istanbul, Turkey**

Production Metallurgy and Technologies Engineering Programme

Supervisor: Assoc. Prof. Dr. Bora Derin

Synthesis of Zr- based bulk metallic glasses. Using the Edmund Bühler Arc Melting and Suction Casting equipment, the effects of hafnium substitution and yttrium addition for the microstructure of

Zr<sub>52.5</sub>Cu<sub>17.9</sub>Ni<sub>14.6</sub>Ti<sub>5</sub>Al<sub>10</sub> are investigated by XRD and EDX/SEM methods.

**B.Sc. Degree**  
**2009-2013**

**Istanbul Technical University, Istanbul, Turkey**

Metallurgical and Materials Engineering

**High School  
2004-2009**

**Kadıköy Anatolian High School  
Science**

**Experimental Skills**

Electrodeposition  
Sputtering  
X-ray Diffraction  
Vibrating Sample Magnetometry  
Confocal Microscopy  
Scanning Electron Microscopy with Energy Dispersive X-ray Analysis

**Foreign Languages**

English (Advanced)  
French (Elementary)  
Spanish (Elementary)

**Academic Stay Abroad**

17 May 2017 – 9 August 2017

University of Cambridge, Department of Materials Science and Metallurgy,  
Device Materials Group, Group of Prof. Zoe Barber

"Epitaxial growth of CuAlNi shape memory alloys by sputtering along with in-situ heat treatment" was studied in collaboration with the Ph.D. candidate Samer Kurdi.

**Trainings**

1<sup>st</sup> SELECTA Workshop: "Fundamentals of electrodeposition of metallic alloys: State of the art at European and international levels". Kragujevac, Serbia. 3-7 November 2015.

2<sup>nd</sup> SELECTA Workshop: "Training on research methodologies, characterization techniques and reporting scientific results". Dresden, Germany. 6-10 March 2016.

3<sup>rd</sup> SELECTA Workshop: "Micro- and nano- electrodeposition for MEMs/NEMs and micro/nanorobotic platforms. Overview of lithography methods. Impact to society". Wiener Neustadt, Austria. 29-31 August 2016.

UAB X-ray Diffraction Unit, X-Pert HighScore Plus Data Analysis Software Training, 20-21 October 2016.

4<sup>th</sup> SELECTA Workshop: "Bridging innovation and entrepreneurship with sustainable materials development " . Gothenburg, Sweden, 5-9 December 2016

*I performed oral presentations about the current state of my Ph.D. project during the first four SELECTA workshops.*

2nd COST Action e-Minds Workshop on Electrodeposition and Structural Characterization. Schwabisch Gmünd, Germany, 2-6 April 2017.

-Member of the team that won the Best Presentation Prize

5<sup>th</sup> SELECTA Workshop: "Materials modeling for target applications: Fundamentals of electrodeposition of metallic alloys: state-of-the-art at European and International levels", Ionnina, Greece, 3-7 September 2017.

*I performed a poster presentation about the current state of my project in the 5<sup>th</sup> SELECTA workshop.*

6<sup>th</sup> SELECTA Workshop: "Introducing materials to market. Practical aspects", Cambridge, United Kingdom

*I prepared a showcase video about the content of my Thesis in the 6<sup>th</sup> SELECTA workshop. The video can be accessed from <http://www.selecta-etn.eu/dissemination>.*

## Articles

D. Bilican, J. Fornell, J. Sort, E. Pellicer, "Electrochemical synthesis of bismuth particles: tuning particle shape through substrate type within a narrow potential window" , Materials (MDPI) 2017, 10, 43.

D. Bilican, E. Menéndez, J. Zhang, P. Solsona, J. Fornell, E. Pellicer, J. Sort, "Ferromagnetic-like behaviour in bismuth ferrite films prepared by electrodeposition and subsequent heat treatment", RSC Advances, 2017, 7, 32133.

## Conferences

Institute of Physics Conference "Plasmas, Surfaces and Thin Films: Early Career Researchers Meeting", Leicestershire, England, 22 June 2017. Poster entitled as follows was presented:

-Synthesis of BiFeO<sub>3</sub> films with Ferromagnetic-like Behaviour by Electrodeposition followed by Heat Treatment

Royal Society of Chemistry Conference "Materials Chemistry Conference", Liverpool , England, 10-13 July 2017. Posters entitled as follows were presented:

-Electrochemical Synthesis of Micron and Submicron-sized Bismuth Particles with Tunable Morphology onto Various Substrates

-Synthesis of Bismuth Ferrite by Electrodeposition Followed by Heat Treatment

3<sup>rd</sup> "Barcelona Nanocluster Meeting", ICMAB, Barcelona. Poster entitled as follows was presented:

-Effects of Post- and In situ Heat Treatment on Sputtered CuAlNi Shape Memory Alloys

## Dissemination Activity

Marie Skłodowska Curie Action "Meet the Fellows 2016", Madrid, Spain. 22 April 2016

-Selected as the "Fellow of the week" on 22 July 2016 on Marie Skłodowska Curie Actions Official Facebook page due to making a presentation about the concept of the SELECTA Project.